Volume 65C
Number 4
Oct.–Dec. 1961

Engineering and Instrumentation

U.S. DEPARTMENT OF COMMERCE

SECTION C

JOURNAL OF RESEARCH

NATIONAL BUREAU OF STANDARDS

Journal of Research
of the
National Bureau of Standards

C. Engineering and Instrumentation

OCT.–DEC. • 1961

VOLUME • 65C

NUMBER • 4

Editor: W. A. Wildhack

Associate Editors: G. F. Montgomery, R. B. Jacobs

Publication dates:
Feb. 15, May 15, Aug. 15, Nov. 15, 1961

JOURNAL OF RESEARCH

The National Bureau of Standards Journal of Research reports research and development in the fields of activity shown at right. Also included from time to time are survey articles on topics closely related to the Bureau's scientific and technical program.

The Journal is published in four separate sections as follows:

A. Physics and Chemistry

Contains papers of interest primarily to scientists working in these fields. Issued six times a year. Annual subscription: domestic, $4.00; foreign, $4.75.

B. Mathematics and Mathematical Physics

Presents studies and compilations designed mainly for the mathematician and the theoretical physicist. Issued quarterly. Annual subscription: domestic, $2.25; foreign, $2.75.

C. Engineering and Instrumentation

Reports research and development results of interest chiefly to the engineer and the applied scientist. Issued quarterly. Annual subscription: domestic, $2.25; foreign, $2.75.

D. Radio Propagation

Reports work in radio propagation physics and upper atmospheric research. Issued six times a year. Annual subscription: domestic, $4.00; foreign, $4.75.

U.S. DEPARTMENT OF COMMERCE
Luther H. Hodges, Secretary

NATIONAL BUREAU OF STANDARDS
A. V. Astin, Director

Functions and Activities

The functions of the National Bureau of Standards are set forth in the Act of Congress, March 3, 1901, as amended. These include the development and maintenance of the national standards of measurement and the provision of means and methods for making measurements consistent with these standards; the determination of physical constants and properties of materials; the development of methods and instruments for testing materials, devices, and structures; advisory services to government agencies on scientific and technical problems; invention and development of devices to serve special needs of the Government; and the development of standard practices, codes, and specifications. The work includes basic and applied research, development, engineering, instrumentation, testing, evaluation, calibration services, and various consultation and information services. The Bureau also serves as the Federal technical research center in a number of specialized fields. The scope of activities of the National Bureau of Standards is suggested in the following listing of the divisions and sections engaged in technical work.

Washington, D.C.

Electricity. Resistance and Reactance, Electrochemistry. Electrical Instruments. Magnetic Measurements. Dielectrics.
Metrology. Photometry and Colorimetry. Refractometry. Photographic Research. Length. Engineering Metrology. Mass and Scale. Volumetry and Densimetry.
Heat. Temperature Physics. Heat Measurements. Cryogenic Physics. Equation of State. Statistical Physics.
Radiation Physics. X-Ray. Radioactivity. Radiation Theory. High Energy Radiation. Radiological Equipment. Nucleonic Instrumentation. Neutron Physics.
Analytical and Inorganic Chemistry. Pure Substances. Spectrochemistry. Solution Chemistry. Standard. Reference Materials. Applied Analytical Research.
Mechanics. Sound. Pressure and Vacuum. Fluid Mechanics. Engineering Mechanics. Rheology. Combustion Controls.
Organic and Fibrous Materials. Rubber. Textiles. Paper. Leather. Testing and Specifications. Polymer Structure. Plastics. Dental Research.
Metallurgy. Thermal Metallurgy. Chemical Metallurgy. Mechanical Metallurgy. Corrosion. Metal Physics. Electrodeposition.
Mineral Products. Engineering Ceramics. Glass. Refractories. Enameled Metals. Crystal Growth. Physical Properties. Constitution and Microstructure.
Building Research. Structural Engineering. Fire Research. Mechanical Systems. Organic Building Materials. Codes and Safety Standards. Heat Transfer. Inorganic Building Materials.
Applied Mathematics. Numerical Analysis. Computation. Statistical Engineering. Mathematical Physics.
Data Processing Systems. Components and Techniques. Digital Circuitry. Digital Systems. Analog Systems. Applications Engineering.
Atomic Physics. Spectroscopy. Infrared Spectroscopy. Solid State Physics. Electron Physics. Atomic Physics.
Instrumentation. Engineering Electronics. Electron Devices. Electronic Instrumentation. Mechanical Instruments. Basic Instrumentation.
Physical Chemistry. Thermochemistry. Surface Chemistry. Organic Chemistry. Molecular Spectroscopy. Molecular Kinetics. Mass Spectrometry.

• Office of Weights and Measures.

Boulder, Colo.

Cryogenic Engineering. Cryogenic Equipment. Cryogenic Processes. Properties of Materials. Gas Liquefaction.
Ionosphere Research and Propagation. Low Frequency and Very Low Frequency Research. Ionosphere Research. Prediction Services. Sun-Earth Relationships. Field Engineering. Radio Warning Service.
Radio Propagation Engineering. Data Reduction Instrumentation. Radio Noise. Tropospheric Measurements. Tropospheric Analysis. Propagation-Terrain Effects. Radio-Meteorology. Lower Atmosphere Physics.
Radio Standards. High Frequency Electrical Standards. Radio Broadcast Service. Radio and Microwave Materials. Atomic Frequency and Time Interval Standards. Electronic Calibration Center. Millimeter-Wave Research. Microwave Circuit Standards.
Radio Systems. High Frequency and Very High Frequency Research. Modulation Research. Antenna Research. Navigation Systems. Space Telecommunications.
Upper Atmosphere and Space Physics. Upper Atmosphere and Plasma Physics. Ionosphere and Exosphere Scatter. Airglow and Aurora. Ionospheric Radio Astronomy.

Order all publications from the Superintendent of Documents
U.S. Government Printing Office, Washington 25, D.C.

Use of funds for printing this publication approved by the Director of the Bureau of the Budget (June 19, 1961).

JOURNAL OF RESEARCH of the National Bureau of Standards—C. Engineering and Instrumentation
Vol. 65C, No. 4, October–December 1961

A New Airglow Photometer*

C. M. Purdy, L. R. Megill, and F. E. Roach

(May 10, 1961)

The study of night airglow phenomena requires the use of various types of instruments, the type depending upon the experimental environment and the results desired for final analysis. It has recently become apparent to the authors that there is a need for a very simple, yet rugged and reliable, photometer. The instrument which is described herein is intended to fill these needs.

1. Introduction

The photometer, which is shown in figure 1, is designed to monitor airglow intensities in one direction only. The more likely choices for this direction are either toward the zenith or the pole. The present instrument is mounted on a base which gives zenith observations most readily, but for other directions a small modification in the base will give the desired angle.

The photometer is designed to observe four colors in sequence. One and one-quarter minutes are required for each color observation. Of this time, 25 sec are used in each of three operations as follows: (1) the instrument has an external shutter over the objective lens which gives a zero reading, (2) a standard light is moved in front of the objective lens giving a relative calibration of the instrument, (3) the objective lens is open to the sky giving a reading of the airglow intensity. A time sequence is shown in figure 2. The photomultiplier detector, the turret, the turret drive mechanism and the optics are contained in one unit—21 in. high, 12 in. square. Several views of the unit are shown in figure 3.

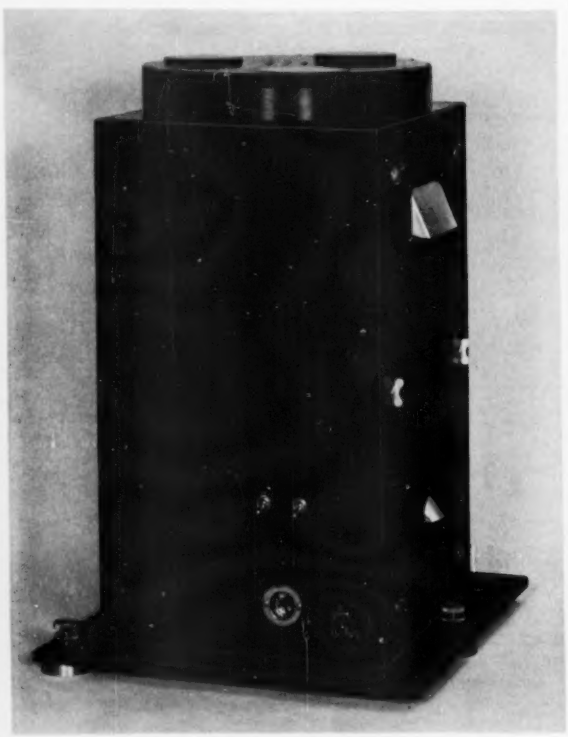

FIGURE 1. *Photometer telescope.*

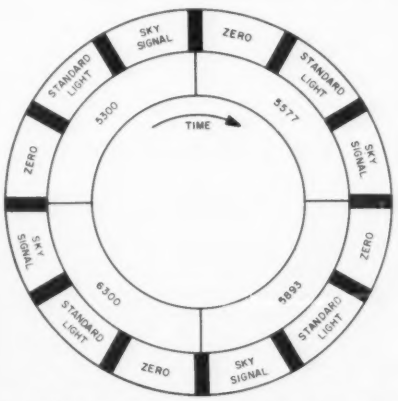

FIGURE 2. *Time sequence of operation of upper and lower telescope turrets.*

2. Optics

The optics used in this telescope consist of an objective and field lens as shown in figure 4.

The optical design is the same as that used in an earlier model [St. Amand, 1953].[1] The field lens images the objective on the surface of the photocathode of the detector, which makes the instrument less sensitive to the position in the field of view of a point source such as a star. This is necessary because of the extremely nonuniform photocathode on the 1P21 photomultiplier used as a detector.[2]

3. Electronics

The photocathode of the 1P21 has an S-4 spectral response, giving it some sensitivity as far as 6300 A. This enables one to observe all the prominent visible

[1] Figures in brackets indicate the literature references at the end of this paper.
[2] The unit is readily adaptable to photomultiplier tubes with an end-on photocathode.

*Contribution from the Central Radio Propagation Laboratory, National Bureau of Standards, Boulder, Colo.

FIGURE 3.—*Telescope drawing.*

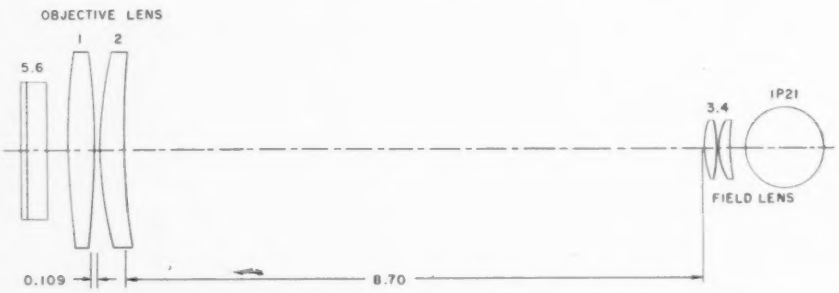

Element Number	Diam. In.	Radi		Center Thickness	Index of Refr. N_D	Eff. Focal L. In.	Material
		Front	Rear				
1	2.85	10.96	-73.43	0.35	1.523	9.23	Water white
2	2.85	5.77	14.43	0.41	1.523	0.73	Plate glass
3	0.90	1.26	- 2.85	0.18	1.611		Dense barium
4	0.90	0.64	2.22	0.18	1.611		Crown, 3
5	2x2	Colored glass transmission filter					
6	2x2	Interference filter					

All dimensions in inches

FIGURE 4. *Telescope optics.*

airglow lines with only one detector. Voltage for the tube is supplied by a commercial plug-in high voltage supply, manufactured by the C. J. Applegate Company. The addition of a 20K series resistance and a 10 mf 2,000 v d-c paper condenser in the output of the high volt power supply reduces the ripple at the output of the supply. The tube is operated at 1,000 v.

The amplifying system consists of an Electro Instruments model A–12 d-c or A–14 d-c amplifier. This unit is an all-transistor amplifier that is chopper stabilized. Since, in general, the airglow intensities are independent of one another, four sensitivities will be needed for standard operation. The amplifier has a fixed gain and the individual gain adjustment for each of the four airglow intensities is accomplished by varying the size of resistor R_s. See figure 5. The system is programed to change sensitivity each time a filter is moved into position in front of the telescope.

The dark current of the photomultiplier presents a problem as it does in any d-c amplifier system. In order to eliminate its effect, a simple circuit is set up at the input of the amplifier which may be adjusted to feed the amplifier an equal and opposite current as shown in figure 5. Since the dark current is a strong function of the temperature, this adjustment is made readily accessible and can be adjusted periodically by the observer. Each of the four sensitivity adjustments available for each filter has its own dark current adjustment. This allows the operator to set the dark current adjustment for each sensitivity. The voltage supply for dark current balance, shown in figure 5, uses a battery. Current drain is so extremely small that the shelf life of the battery is not shortened significantly. A galvanometric strip chart recorder is used to record the data. In order to match the characteristic impedance of the recorder and accomplish optimum time response, a driver stage was necessary as shown in figure 5. This stage is not necessary for servo-type recorders.

4. Mechanical Drive

The movements of both turrets are controlled by purely mechanical means. An exploded view of the gear system is shown in figure 6. The rotating turret "b" which holds the filters and turret "a" which holds the standard light, the sky opening, and a blank position for a zero, are driven by two concentric shafts. Each has its own gear system, but both are driven by the same motor. The motor runs continuously and a periodic motion of the turrets is obtained by a Geneva drive system. Descriptions of this type of operation are available in the literature [Jones, 1930]. This type of motion combines high reliability with accurate positioning.

5. Filter System

The filters are mounted, as previously mentioned, in a disk which is periodically rotated into place. The particular line desired for study is selected by using an interference filter with a band pass of about 50 A at half transmission. Colored glass filters may be used to eliminate side bands. Any wavelengths within the sensitivity range of the detector may, of course, be observed by changing filters. The present instrument is equipped with filters centered at 5300, 5577, 5893, and 6300 A. The last three are centered on airglow lines. The first is in a region where there is relatively little airglow and is used to help subtract out the integrated starlight and light from other extraterrestrial sources.

6. Calibration and Standard Light

The problem of calibration is one of the more difficult in the airglow field [Roach, 1958]. There is a well-calibrated photometer at the NBS Fritz Peak airglow station. The absolute calibration is obtained by comparison with this instrument.

In order to maintain the calibration we are using, as previously mentioned, a standard light. This is a phosphorescent source using a radioactive decay product as the activator.

There are many phosphors on the market using radioactive decay products for activation. An inexpensive source may be made from a radium activated phosphor which is applied as paint. These sources do exhibit some decay resulting from damage of the phosphor by the heavy ionization due

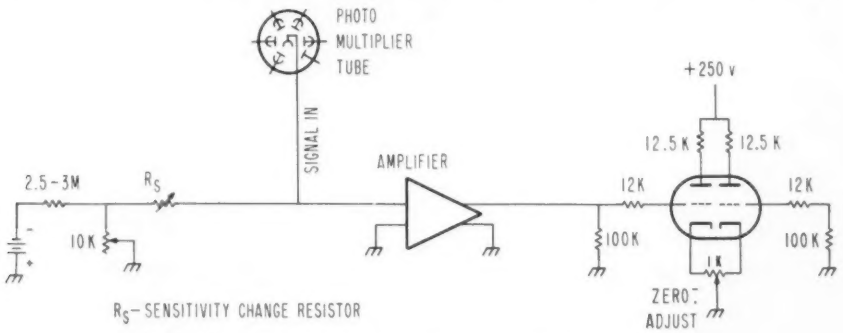

FIGURE 5. *Simplified schematic of amplification system.*

The signal output from the driver tube is taken directly from the plates of the tube.

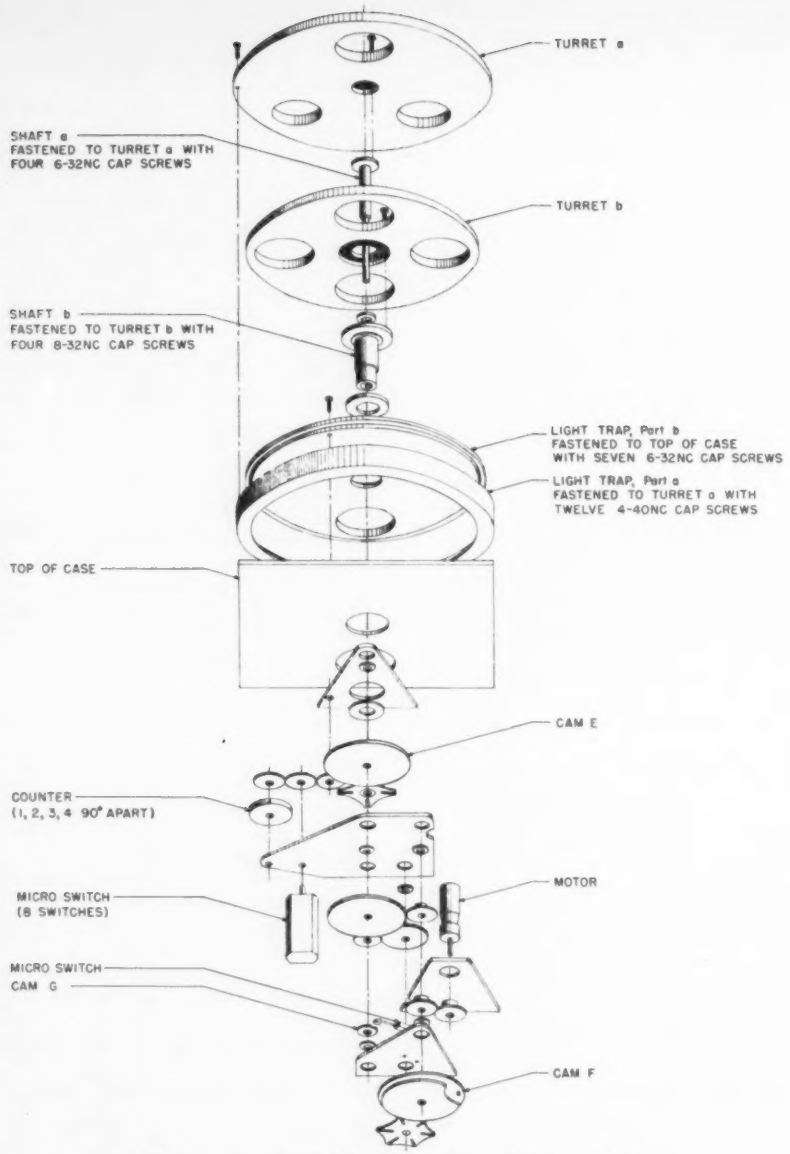

FIGURE 6. *Turret drive mechanism exploded assembly.*

to the alpha particles from the radium. They are, however, quite good for considerable periods and easily obtained. Most phosphors available have peak response in the green and little emission in the red. This is also true of some tritium activated phosphors which have been used.

A phosphor which has been found to have good red emissions as well as the shorter wavelengths in the visible region is the U.S. Radium Corp. Isolite Standard Source. This contains a U.S. Radium Corp. red phosphor with carbon 14 as the activator. This phosphor is available with several types of radioactive activators.

The authors recognize the contributions of Ralph C. Darr of the NBS Instrument Shop for excellent workmanship, particularly in the design of the details of the Geneva motion.

7. References

[1] Jones, F. D., Editor, Ingenious Mechanisms for Designers and Inventors (The Industrial Press, 1930).
[2] Roach, F. E., The intercalibration of airglow photometers, unpublished (1958).
[3] St Amand, Pierre, A possible relation between the night airglow and the ionosphere, Thesis (California Institute of Technology, 1953).

(Paper 65C4–73)

JOURNAL OF RESEARCH of the National Bureau of Standards—C. Engineering and Instrumentation
Vol. 65C, No. 4, October–December 1961

A Guide to the Use of the Modified Reflectometer Technique of VSWR Measurement *

Wilbur J. Anson

(February 10, 1961)

The theory of the modified reflectometer technique of measuring VSWR at microwave frequencies is discussed briefly, the operational procedure is outlined, and selected results are given of an unpublished error analysis. Much of the theory and procedure has been published in isolated papers. This paper unifies those details essential to the use of this technique and includes procedural suggestions that have grown out of extensive experience with the technique. The error analysis provides the means to evaluate the accuracy of any particular measurement made with this system.

1. Introduction

The modified reflectometer technique [Beatty and Kerns, 1958; Beatty, 1959; Engen and Beatty, 1959] recently developed at the Boulder Laboratory of the National Bureau of Standards is a method of making accurate VSWR measurements in rectangular waveguide. This technique is capable of measuring low VSWR's (VSWR<2) to accuracies of 1 percent quite easily. Accuracies of 0.1 percent in VSWR are obtainable with extra care in the adjustments of the modified reflectometer.

The purpose of this paper is to provide operating knowledge of the modified reflectometer technique. Much of the material presented herein has been published elsewhere but this paper gathers in one place those details essential to the use of this technique. The paper also offers suggestions on procedure which have grown out of extensive experience with this technique. Also it provides selected results of an error analysis which are important in evaluating the accuracy of any particular measurement made with this system.

2. An Outline of the Theory

The modified reflectometer measures the magnitude of the reflection coefficient of a waveguide termination at microwave frequencies. This method utilizes a directional coupler oriented to couple to the reflected wave with appropriately placed tuners adjusted so that the amplitude of the voltage wave from the side arm is directly proportional to the magnitude of the reflection coefficient.

According to references 1 and 2, the scattering equations for a three arm junction representing the combination of a directional coupler and two tuners (fig. 1) are

$$\begin{aligned} b_1&=S_{11}a_1+S_{12}a_2+S_{13}a_3\\ b_2&=S_{21}a_1+S_{22}a_2+S_{23}a_3\\ b_3&=S_{31}a_1+S_{32}a_2+S_{33}a_3, \end{aligned} \tag{1}$$

where $a_1=b_g+b_1\Gamma_G$, $a_2=b_2\Gamma_L$, and $a_3=b_3\,\Gamma_D$. These may be solved for the response in the form

$$b_3=b_g k\,\frac{(1+K\Gamma_L)}{(1-\Gamma_{2i}\Gamma_L)}, \tag{2}$$

$$k=\frac{S_{31}}{\begin{vmatrix}(1-S_{11}\Gamma_G) & S_{13}\Gamma_D\\ S_{31}\Gamma_G & (1-S_{33}\Gamma_D)\end{vmatrix}}, \tag{3}$$

$$K=\frac{\begin{vmatrix}S_{21} & S_{22}\\ S_{31} & S_{32}\end{vmatrix}}{S_{31}}, \tag{4}$$

and

$$\Gamma_{2i}=\frac{\begin{vmatrix}-(1-S_{11}\Gamma_G) & S_{12} & S_{13}\Gamma_D\\ S_{21}\Gamma_G & S_{22} & S_{23}\Gamma_D\\ S_{31}\Gamma_G & S_{32} & -(1-S_{33}\Gamma_D)\end{vmatrix}}{\begin{vmatrix}(1-S_{11}\Gamma_G) & S_{13}\Gamma_D\\ S_{31}\Gamma_G & (1-S_{33}\Gamma_D)\end{vmatrix}}. \tag{5}$$

Rearranged slightly, the equation becomes

$$b_3=\frac{b_g}{\begin{vmatrix}(1-S_{11}\Gamma_G) & S_{13}\Gamma_D\\ S_{31}\Gamma_G & (1-S_{33}\Gamma_D)\end{vmatrix}}\;\frac{S_{31}+\begin{vmatrix}S_{21} & S_{22}\\ S_{31} & S_{32}\end{vmatrix}\Gamma_L}{1-\Gamma_{2i}\Gamma_L}. \tag{6}$$

Now let $S_{31}=0$ and $\Gamma_{2i}=0$, then

$$b_3=\frac{b_g S_{21}S_{32}\Gamma_L}{(1-S_{11}\Gamma_G)(1-S_{33}\Gamma_D)}. \tag{7}$$

If b_g, Γ_G, and Γ_D are constant, then

$$b_3=C_{(\text{constant})}\Gamma_L. \tag{8}$$

For a detector not phase sensitive

$$|b_3|=|C\Gamma_L|. \tag{9}$$

Note that this last relationship is the desired response mentioned just before (1), i.e., the amplitude of the voltage wave from the sidearm is directly proportional to the magnitude of the reflection coefficient.

*Contribution from the Radio Standards Laboratory, National Bureau of Standards, Boulder, Colo.

Therefore, let $\Gamma_L=\Gamma_u$ (the unknown) so that $|b_3|_u=|C\Gamma_u|$. Then let $\Gamma_L=\Gamma_s$ (a known quantity) so that $|b_3|_s=|C\Gamma_s|$. Now form the ratio

$$\frac{|b_3|_u}{|b_3|_s}=\frac{|\Gamma_u|}{|\Gamma_s|}. \tag{10}$$

Thus, given the value of $|\Gamma_s|$, and measuring the ratio of the sidearm outputs $\frac{|b_3|_u}{|b_3|_s}$, the value of $|\Gamma_u|$ may be calculated.

3. Procedure

Any practical use of the modified reflectometer technique depends upon an understanding of the physical conditions imposed by the theory.

For $|b_3|$ to conform to (8) certain quantities as represented in (7) must remain constant. It requires a stable source (constant b_g) well isolated from load changes. It also requires apparent generator and detector impedances that are unchanging (constant Γ_G and Γ_D)—requirements which can be essentially fulfilled by isolators placed at terminal planes T_1 and T_3 in figures 1 and 2.

The remaining quantities of (8), namely S_{21}, S_{32}, S_{11}, and S_{33}, are constants of the 3-arm junction and therefore remain unchanging after adjustments are made for $S_{31}=0$ and $\Gamma_{2f}=0$.

3.1. Adjustment of $S_{31}=0$ and $\Gamma_{2f}=0$

For a directional coupler with the arms labeled as in figure 2 the statement that $S_{31}=0$ is equivalent to saying that the coupler has infinite directivity since, in terms of scattering coefficients, directivity $\equiv 20\log_{10}\left|\frac{S_{32}}{S_{31}}\right|$.

Infinite directivity can be approached by adjusting tuner A for no variation in the output $|b_3|$ when sliding a load of small reflection ($|\Gamma_L|<0.005$) in the uniform waveguide.

After making this adjustment, the condition $\Gamma_{2f}=0$ can be approached by adjusting tuner B for no variation in the output $|b_3|$ when sliding a load of large reflection (usually a shorting plunger) in the uniform waveguide.

This adjustment sequence may need to be repeated several times since the two adjustments are not completely independent. However, if the reflection from the sliding load used in the directivity adjustment is small enough, then the two adjustments are more nearly independent and one adjustment sequence will usually be enough.

NOTE: It is seldom necessary for the variation to be completely zero. The variation allowable while the loads are slid in each adjustment depends upon the desired accuracy of the measurement to be made. This allowable variation is discussed in the error analysis and is displayed in figures 5, 6, 7, and 8.

3.2. An Alternate Adjustment Procedure for $S_{31}=0$ and $\Gamma_{2f}=0$

Consider the definition for directivity in conjunction with (6) and observe that $|b_3|=0$ when $\Gamma_L=0$ if the directivity is infinite. Therefore the adjustment could be made by attaching a flat load ($\Gamma_L=0$) and adjusting tuner A for $|b_3|=0$. But there is no commercial termination flat enough for the accuracy of adjustment often needed and therefore an adjustable sliding termination such as the one described by R. W. Beatty [1957] must be adjusted for $\Gamma_L=0$.

The two adjustments for $S_{31}=0$ and $\Gamma_L=0$, using an adjustable sliding termination, are carried out alternately. The adjustable termination is slid and adjusted so that the variations in $|b_3|$ are reduced and then tuner A is adjusted so that the average level of the variation is lowered. When no variation in $|b_3|$ occurs as the adjustable termination is slid, *and* when $|b_3|$ is zero, then $S_{31}=0$ and $\Gamma_L=0$. Note that after adjustment of tuner A the variations will be greater than before. The greater variation results from increased sensitivity as infinite directivity is approached with the adjustments of tuner A.

Adjustments for $\Gamma_{2f}=0$ can be made after making the previous adjustment for infinite directivity. The symbol Γ_{2f} in (2), besides representing a group of symbols as noted in (5), actually represents the reflection coefficient "looking in" arm 2 of the junction as indicated in figure 2. Therefore the condition $\Gamma_{2f}=0$ is equivalent to saying that, at the terminal plane T_2, this input reflection coefficient is zero.

In figure 3 a scheme is illustrated for recognizing this matched condition. Power is coupled out of the main line to supply an auxiliary directional coupler

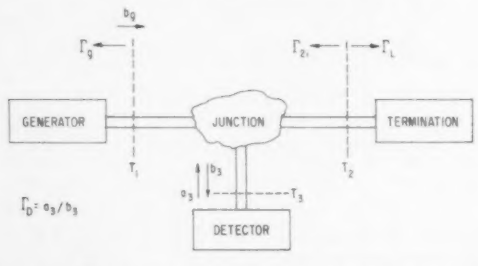

FIGURE 1. *Three arm junction representing the modified reflectometer.*

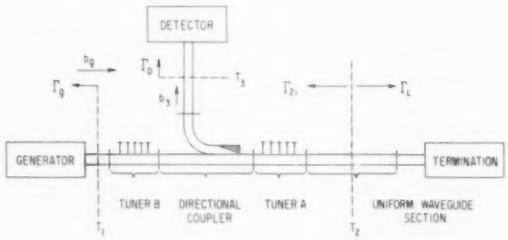

FIGURE 2. *Diagram of modified reflectometer.*

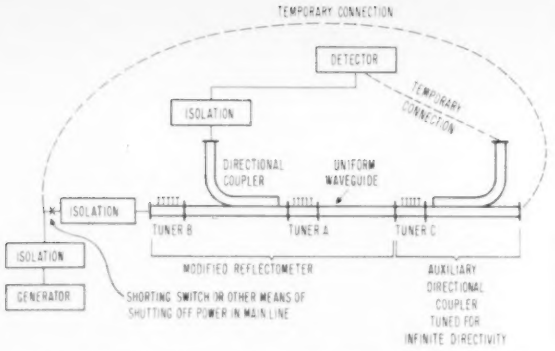

FIGURE 3. *Equipment arrangement for adjusting* $\Gamma_{2i}=0$.

tuned for infinite directivity. This coupler is temporarily attached to the uniform waveguide with power shut off in the main line supplying the modified reflectometer. Tuner B is then adjusted for no output from the sidearm of the auxiliary coupler. The condition $\Gamma_{2i}=0$ is thereby fulfilled.

There must, of course, be enough isolation on the generator side of the modified reflectometer to maintain essentially the same value of Γ_{2i} during both this matching procedure and the normal operation of the reflectometer. Also, there must be enough isolation between the generator and whatever means is used for shutting off the main line power to insure no possibility of frequency pulling.

The auxiliary directional coupler can be tuned for infinite directivity by utilizing the flat load previously discussed. This flat load is attached temporarily to the auxiliary coupler and tuner C adjusted for no output from the sidearm of the auxiliary coupler.

This adjustment sequence may also need to be repeated several times since the two adjustments are not completely independent. However, if the adjustment for infinite directivity is carefully made, one adjustment sequence will be enough.

Although this alternate procedure is sometimes easier to use, it does not provide sufficient information to evaluate the maximum errors due to imperfect adjustments of the tuners. Therefore, the adequacy of the adjustments must be checked by sliding the small and large reflection loads in the uniform waveguide and by observing whether the variations in $|b_3|$ are within the allowable limits for the measurement accuracy needed.

If the variations are not within the allowable limits it is important that the final adjustments be made with the small and large reflection sliding loads *in the uniform waveguide*. Otherwise, reflections from the waveguide joints will detune the infinite directivity adjustment.

3.3. Another Alternate Adjustment Procedure for $S_{31}=0$

By adding an auxiliary channel as illustrated in figure 4, the adjustment for infinite directivity ($S_{31}=0$) is made considerably easier and faster [Beatty, Engen, and Anson, 1960]. This auxiliary

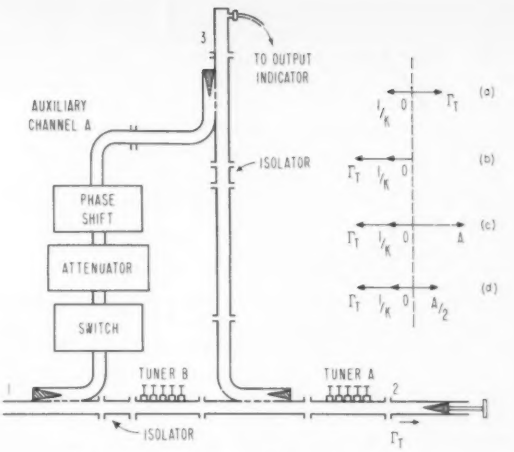

FIGURE 4. *Auxiliary channel technique.*

channel permits introduction of a signal of the proper phase and magnitude to null the signal component indicative of finite directivity.

From (2) the response from the sidearm is

$$|b_3|=|b_g K|\left|\frac{1+K\Gamma_L}{1-\Gamma_{2i}\Gamma_L}\right|.$$

If $|\Gamma_{2i}|$ is small, i.e., $|\Gamma_{2i}|<0.01$, then a very good approximation is

$$|b_3|=|b_g k K|\cdot\left|\frac{1}{K}+\Gamma_L\right|. \tag{11}$$

The following description of the procedure is best understood by referring to (11) and the vector diagrams in figure 4.

1. With the shorting switch in the auxiliary arm closed, arbitrarily position the small reflection load in the uniform waveguide and adjust tuner A for $b_3=0$. This corresponds to step (a) in figure 4 wherein $1/K$ is oppositely directed and equal in magnitude to $|\Gamma_L|$.

2. Slide the load for maximum $|b_3|$. This corresponds to step (b) in figure 4 wherein Γ_L and $1/K$ are in phase.

3. Open the waveguide switch in auxiliary channel A and adjust the phase shifter and attenuator in that channel for $|b_3|=0$ again. This corresponds to step (c) in figure 4 which illustrates a signal A having been introduced to null $\left|\frac{1}{K}\right|+|\Gamma_L|$.

4. Introduce 6.02 db of attenuation into the auxiliary arm to reduce the amplitude of signal A by one-half as illustrated in step (d) in figure 4. This A/2 cancels the $1/K$ term in (11) and results in infinite directivity. Recall that $|\Gamma_{2i}|$ is assumed small so that (11) is a good approximation.

The directivity obtained by this procedure can be checked by sliding the low reflection load and observing the variations in $|b_3|$ as noted in section 3.1. If the directivity obtained thusly is not high enough, then trial and error adjustments using the phase

shifter and the attenuator in the auxiliary arm or tuner A will allow closer adjustment. However, adjustments using the components of the auxiliary arm are in general easier because these components usually present better resolution than tuner A.

To avoid possible interaction between the two channels, two isolators should be included as shown in figure 4. Other tuning [Engen, 1960] could be employed to reduce interaction but these two isolators should suffice.

3.4. Measurement of $|\Gamma_u|$

Certain details vary from system to system and from operator to operator depending upon personal preferences, equipment available and the accuracies needed. Therefore, no attempt has been made to write this guide for a specific arrangement of equipment.

However, regardless of the arrangement of the apparatus in the system, the ratio $\left|\frac{\Gamma_u}{\Gamma_s}\right|$ can be conveniently measured by some adaptation of the following sequence:

A. Adjust $S_{31}=0$ and $\Gamma_{2f}=0$ by some combination of methods as previously outlined.

B. Check the adequacy of the adjustments to insure the achievement of the measurement accuracy required.

C. Attach the microwave termination of unknown reflection coefficient Γ_u to the uniform waveguide.

D. Set $|b_3|$ at some convenient reference level on some suitable detector and note the setting of a calibrated attenuator. This attenuator, of course, must be properly matched [Beatty, 1954; Schafer and Rumfelt, 1959] to measure accurately the voltage ratios at the detector.

E. Replace the unknown with some standard termination whose reflection coefficient is accurately known.

F. Return $|b_3|$ to the reference level by adjustment of the calibrated attenuator mentioned in step (D).

G. Record the difference in settings of the calibrated attenuator between step (D) and step (F). Calculate the value of $|\Gamma_u|$ from this difference, i.e., $R=20\log_{10}\left|\frac{\Gamma_s}{\Gamma_u}\right|$ where R is the difference in decibels. This calculation can be aided by reference to a table [Beatty and Anson, 1960] of reflection coefficient versus return loss.

4. The Error in the Measurement of $|\Gamma_u|$ and VSWR Due to $S_{31}\neq 0$ and $\Gamma_{2f}\neq 0$

As noted previously, the variation in $|b_3|$ allowable while the loads are slid in each adjustment depends upon the desired accuracy of the measurement made. This allowable variation can be computed from the following equations or taken from the graphs included for certain measurement situations. It is recommended that the adjustments be checked by this method both *before* and *after* measurements are made as an indication of changes created by accidental bumps or frequency drift.

4.1. The Error Due to $S_{31}\neq 0$

It can be shown that the maximum fractional error (assuming the worst phase combination) in the measurement of $|\Gamma_u|$, where $S_{31}\neq 0$ but all other conditions are met, is given by the expression

$$\frac{d|\Gamma_u|}{|\Gamma_u|}\leq\frac{1}{|K|}\left(\frac{|\Gamma_s|+|\Gamma_u|}{|\Gamma_u|-\left|\frac{\Gamma_u}{K}\right|}\right) \tag{12}$$

where $\Gamma_s\equiv$reflection coefficient of the standard termination,

$\Gamma_u\equiv$reflection coefficient of the unknown termination,

and $$|K|=\frac{10^{R_1/20}+1}{(10^{R_1/20}-1)|\Gamma_L|},$$

in which R_1 is the db variation in $|b_3|$ as the small reflection load Γ_L is slid in the uniform waveguide.

The corresponding maximum error in the measurement of VSWR, when $S_{31}\neq 0$, is obtained from (12) applying the following relation:

$$\frac{d\sigma_u}{\sigma_u}=\frac{2|\Gamma_u|}{1-|\Gamma_u|^2}\frac{d|\Gamma_u|}{|\Gamma_u|}\quad\text{where }\sigma_u\equiv\text{VSWR}. \tag{13}$$

4.2. The Error Due to $\Gamma_{2f}\neq 0$

The maximum fractional error in the measurement of $|\Gamma_u|$, when $\Gamma_{2f}=0$ but all other conditions are met, is given by the expression

$$\frac{d|\Gamma_u|}{|\Gamma_u|}\leq\frac{(|\Gamma_u|+|\Gamma_s|)|\Gamma_{2f}|}{1-\Gamma_{2f}\Gamma_u} \tag{14}$$

where

$\Gamma_s\equiv$reflection coefficient of the standard termination,

$\Gamma_u\equiv$reflection coefficient of the unknown termination,

and $|\Gamma_{2f}|$ is obtained from

$$R_2=20\log_{10}\frac{1+|\Gamma_{2f}\Gamma_L|}{1-|\Gamma_{2f}\Gamma_L|}$$

in which R_2 is the db variation in $|b_3|$ observed as a large reflection load (usually a shorting plunger whose $|\Gamma_L|\cong 1$).

The corresponding maximum error in the measurement of VSWR, when $\Gamma_{2f}\neq 0$, is obtained from (14) by applying (13).

4.3. The Error Due to Both $S_{31}\neq 0$ and $\Gamma_{2f}\neq 0$

Seldom, if ever, will S_{31} or Γ_{2f} be adjusted perfectly. However, it can be shown that the maximum error due to both $S_{31}\neq 0$ and $\Gamma_{2f}\neq 0$ simultaneously is the sum of the individual maximum errors. Therefore, these individual errors may be obtained from (12) through (14), or from figures 5 through 8, and added to form the maximum error of the measurement due to $S_{31}\neq 0$ and $\Gamma_{2f}\neq 0$.

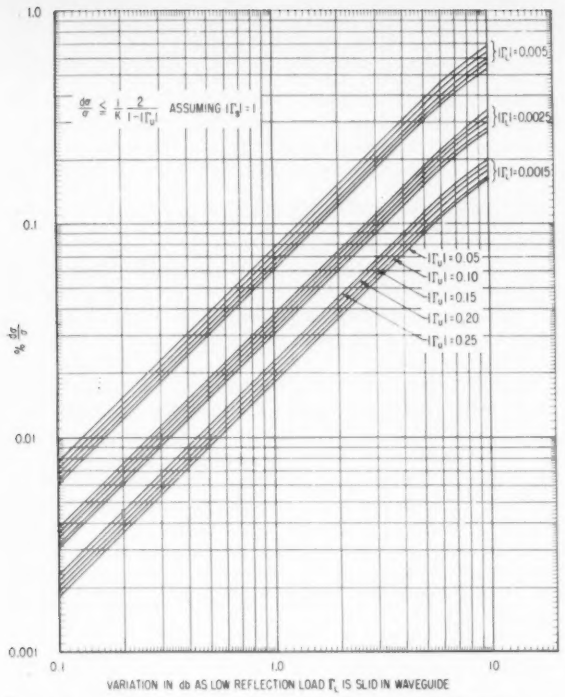

FIGURE 5. *The maximum error in measuring VSWR by the modified reflectometer technique due to* $S_{31} \neq 0$ *and assuming* $\Gamma_{2i}=0$.

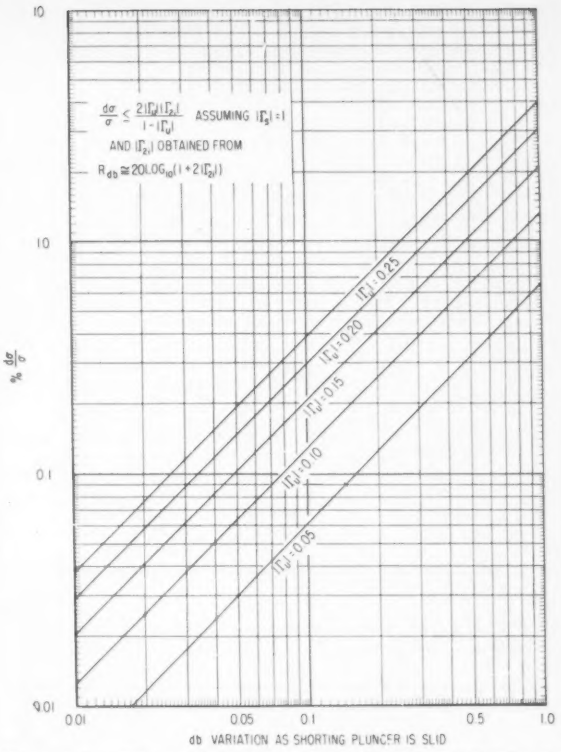

FIGURE 6. *The maximum error in measuring VSWR by the modified reflectometer technique due to* $\Gamma_{2i} \neq 0$ *and assuming* $S_{31}=0$.

Example: Suppose there is 0.5 db variation in $|b_3|$ as a small reflection load $|\Gamma_L|<0.005$ is slid in the uniform waveguide and there is a 0.02 db variation as a short ($|\Gamma_s| \approx 1$) is slid. What is the total limit of error in the measurement of the VSWR of a termination whose reflection coefficient is $|\Gamma_u| \approx 0.2$? From figure 5 the maximum error in measuring VSWR due to $S_{31} \neq 0$ is 0.036 percent; from figure 6 the maximum error due to $\Gamma_{2i} \neq 0$ is 0.058 percent. So the maximum error (due to both $S_{31} \neq 0$ and $\Gamma_{2i} \neq 0$) in measuring the VSWR of the termination is 0.094 percent.

5. Procedural Suggestions

1. Adjustment of the tuners for no variation in the sidearm response $|b_3|$ is easier if some systematic approach is used. One such approach is the following:

A. Slide the load for either a maximum or minimum response. In this example assume that it was slid for maximum.

B. Adjust a stub of the tuner in the direction which lowers the detector response. (Although this example uses a multiple-stub tuner the same procedure is usually adaptable to other types of tuners.)

C. Slide the load for a minimum.

D. Adjust the *same* stub in the same direction as before. If the response increases, i.e., moves toward the average of the variation, then further adjustment of that tuning stub using steps (A) through (D) repeatedly will systematically reduce the variation. If the response decreases, i.e., moves away from the average of the variation, adjustment of that stub will probably be useless and another stub should be tried.

The adjustments for no variation as the load is slid are usually quicker if several effective stubs are located by this procedure and then alternately adjusted.

If no effective stubs can be located, make some random adjustment of the tuner to raise or lower the detector response and repeat the previous procedure. This is a trial and error process. Experience with your own equipment will provide "feel" for the detector response level resulting when the sliding load variations have been reduced.

2. An approximation to the detector response level resulting when the variation in the sidearm output has been reduced for the infinite directivity can be obtained as follows:

A. Slide the low reflection termination for a minimum.

B. Adjust tuner A for a null.

C. Slide the low reflection termination for a maximum. About 6 db down from the maximum is the detector response level resulting when infinite directivity is achieved. This level can serve as a guide when making the adjustments for no variation as the load is slid.

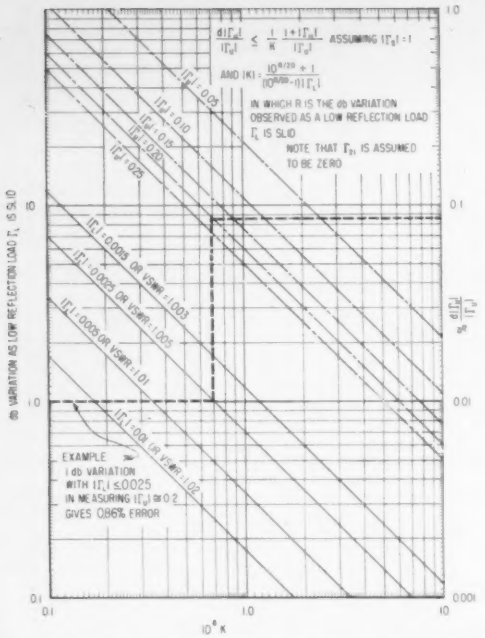

FIGURE 7. *The maximum error in measuring* $|\Gamma_u|$ *by the modified reflectometer technique due to* $S_{31} \neq 0$ *and assuming* $\Gamma_{2i}=0$.

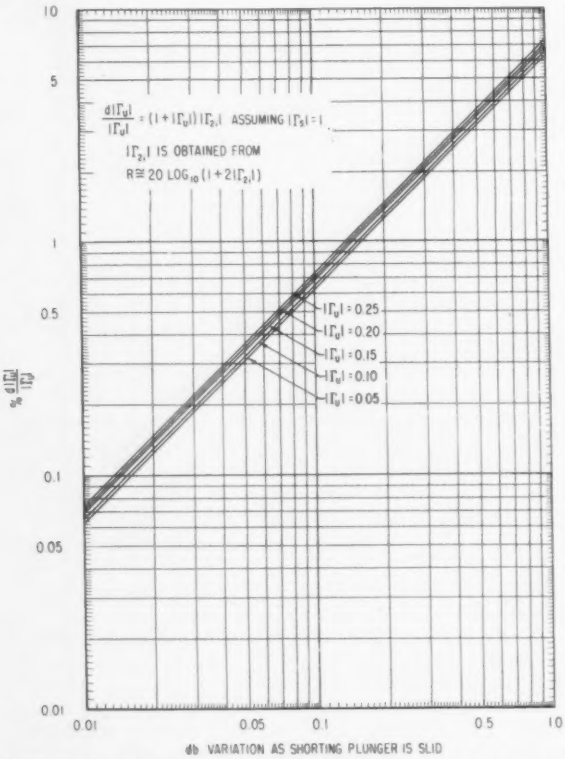

FIGURE 8. *The maximum error in measuring* $|\Gamma_u|$ *by the modified reflectometer technique due to* $\Gamma_{2i} \neq 0$ *and assuming* $S_{31}=0$.

This procedure avoids the one possible false adjustment which could result in an approximately constant output with $\left|\frac{1}{K}\right| \gg |\Gamma_T|$. This misleading adjustment is seldom encountered except when adjusting the equipment the first time. It sometimes occurs at that time because the system lacks sufficient power sensitivity for detection of the approximately constant output signifying $\left|\frac{1}{K}\right| << |\Gamma_T|$ which occurs at a low power level.

3. It is recommended that the adjustments for S_{31} and Γ_{2i} be checked both *before* and *after* a VSWR or reflection coefficient measurement is made to detect possible changes created by accidental bumps or frequency drift.

4. The reflection coefficient magnitude $|\Gamma_L|$ of the small reflection load need not be determined to any great accuracy. Computation of the maximum error requires only that the actual value of $|\Gamma_L|$ is less than the value used in the computation.

This reflection coefficient magnitude can be determined accurately enough as follows:

A. Make the normal adjustments of the system, repeating the adjustment sequence until adjustment for $\Gamma_{2i}=0$ does not require further adjustment of $S_{31}=0$.

B. Slide the small reflection load and observe the maximum and minimum $|b_3|$. There should be little, if any, detectable difference between the minimum and the maximum. Therefore, it is usually sufficient to position the sliding load for the average response and measure $|\Gamma_L|$ for this position using the magnified reflectometer technique. For a truly conservative figure, however, measure the reflection coefficient magnitude of the load in the position of minimum $|b_3|$.

If the standard termination being used is a "short" ($|\Gamma_s|=1$) the ratio $R=20 \log_{10} \frac{|\Gamma_s|}{|\Gamma_u|}$ may be too large for the calibrated attenuator of the system. Then it may be necessary to use a standard of smaller reflection coefficient in order to measure $|\Gamma_u|$.

5. The adjustment of the tuners as outlined in 5.1 is an efficient technique if effective stubs can be found. The following technique aids in finding effective stubs for the infinite directivity adjustment.

A. Adjust tuner A and the sliding load for $|b_3|=0$.

B. Slide the load for maximum $|b_3|$.

C. Now at least one of the stubs is an "effective" stub. Continue the adjustment as outlined in 5.1.

6. When using the small reflection load ($|\Gamma_L| < 0.005$) the signal level may disappear into the noise as the adjustments for infinite directivity are attempted. This difficulty indicates that the detection system does not have sufficient power sensitivity. Rather than invest in more sensitive equipment, a load with greater reflection (perhaps $|\Gamma_L| \sim 0.025$) can be used for the infinite directivity adjustment provided the adjustment sequence outlined in section 3.1 is repeated as indicated. However, this alternate procedure is considerably more time consuming.

The author is indebted to Edward Niesen for his invaluable assistance in the operation and maintenance of the equipment, to R. W. Beatty for his encouragement and helpful suggestions during the writing of this guide, and to David Wait and Michael Brady for their work on the error analysis.

6. References

Beatty, R. W., Mismatch errors in the measurement of ultra high frequency and microwave variable attenuators, J. Research NBS **52,** 7 (Jan. 1954).

Beatty, R. W., An adjustable sliding termination for rectangular waveguide, IRE Trans. on Microwave Theory and Tech. **5,** No. 3 (July 1957).

Beatty, R. W., Magnified and squared VSWR responses, IRE Trans. on Microwave Theory and Tech. **7,** No. 3 (July 1959).

Beatty, R. W., and W. J. Anson, Table of magnitude of reflection coefficient versus return loss $\left(L_R = 20 \log_{10} \frac{1}{K}\right)$, NBS Tech. Note 72 (Sept. 1960).

Beatty, R. W., G. F. Engen, and W. J. Anson, Measurement of reflections and losses of waveguide joints and connectors using microwave reflectometer techniques, IRE Trans. on Instrumentation **I-9,** No. 2, 219–226 (Sept. 1960).

Beatty, R. W., and D. M. Kerns, Recently developed microwave impedance standards and methods of measurement, IRE Trans. on Instrumentation, p. 319 (Dec. 1958).

Engen, G. F., A method of improving isolation in multichannel waveguide systems, IRE Trans. on Microwave Theory and Tech. **8,** p. 460 (July 1960).

Engen, Glenn F., and R. W. Beatty, Microwave reflectometer techniques, IRE Trans. on Microwave Theory and Tech. 351–355 (July 1959).

Schafer, G. E., and A. Y. Rumfelt, Mismatch errors in cascade connected variable attenuators, IRE Trans. on Microwave Theory and Tech. **7,** p. 447 (Oct. 1959).

(Paper 65C4—74)

JOURNAL OF RESEARCH of the National Bureau of Standards—C. Engineering and Instrumentation
Vol. 65C, No. 4, October–December 1961

An X-Ray Diffractometer Cryostat Providing Temperature Control in the Range 4 to 300 °K*

Floyd A. Mauer and Leonard H. Bolz

(July 5, 1961)

The diffractometer cryostat described earlier has been modified to provide a means for controlling temperature and for confining the vapor in equilibrium with volatile samples. Materials with vapor pressures as great as 1 atmosphere (atm) can be handled without loss of insulating vacuum, and temperatures can be controlled with an accuracy of ±0.1 °K in the range 4 to 20 °K decreasing to ±1.0 °K at 300 °K. Data on the lattice constant and thermal expansion of neon are given to demonstrate the suitability of the apparatus for maintaining a desired temperature while working with a volatile material.

1. Introduction

In 1958 the authors collaborated with others in designing a cryostat for obtaining X-ray diffraction patterns of polycrystalline solids formed by deposition on a surface cooled by liquid helium [1].[1] It was used with some success in studying low-temperature solids condensed from the gaseous phase, but the design imposed serious limitations on the choice of experimental conditions. The copper block on which samples were deposited was soldered directly to the bottom of the helium reservoir, and gaseous samples were introduced into the insulating vacuum space through a tube directed at this block. Most of the material froze where it first impinged on the helium-cooled surface, and could be examined by X-ray diffraction methods through thin beryllium windows in the outer wall. Deposition and examination at the boiling temperatures of conventional cryogenic liquids could be accomplished readily, but, at intermediate temperatures, observations could be made only while the block was warming after depletion of the refrigerant. The normal rate of warming (1° per min) was too high to permit adequate X-ray data to be obtained. It was not feasible to maintain a desired temperature by heating the block electrically while it was in contact with liquid helium, and when crude techniques for isolating and heating it were tried, the increase in vapor pressure of the sample usually interfered. When the vapor pressure exceeded 10^{-5} mm of Hg, diffusion of the sample into the insulating vacuum spaces resulted in excessive heat transfer, while condensation on surfaces colder than the block eventually led to disappearance of the sample from the surface in the X-ray beam.

These difficulties have been overcome in recent modifications which permit the copper block to be isolated from the helium reservoir. It can be heated electrically or cooled at any time to the temperature of the refrigerant. An electronic controller maintains the desired temperature, and a Mylar window separates the specimen chamber from the insulating vacuum spaces so that sample vapor pressures as high as 1 atm can be tolerated. Moreover, heat leaks have been reduced so that 2 liters of liquid helium last for as long as 6 hr.

The method of isolating the copper block from the helium reservoir is an adaptation of that used by Henshaw [2] in his neutron diffractometer cryostat. In most other designs, a low-conductivity link is introduced between the sample and the liquid helium reservoir before an experiment is begun. Thereafter, the sample cannot be cooled to the temperature of the refrigerant and may require hours to reach its equilibrium temperature. Henshaw overcame these difficulties by placing his specimen block at the lower end of a thin-walled stainless steel tube joined to the bottom of the helium reservoir. Initially, liquid helium fills this tube and is in direct contact with the specimen block. When the block is to be heated, a plug is inserted in the top of the tube to exclude the liquid. Because of the low conductivity of the stainless steel used for the tube, the block can be heated to 40 or 50 °K before the increase in the evaporation rate of the liquid helium becomes excessive. Figure 1 shows how this design has been adapted to the diffractometer cryostat.

2. Modification of the Cryostat

By comparing figure 1 with the corresponding figure in the earlier paper [1] it can be seen that many features of the cryostat remain unchanged. It is a conventional double Dewar vessel consisting of a liquid helium vessel (21) surrounded by a liquid nitrogen container (22) and radiation shields (19, 3) which screen the helium vessel from thermal radiation.

In modifying the cryostat the original copper block was detached from the helium reservoir at the soft solder joint (7). The inner vacuum wall (10), which had separated the vacuum around the helium

*This work was performed under the National Bureau of Standards Free Radicals Research Program supported by the Department of Defense.
[1] Figures in brackets indicate the literature references at the end of this paper.

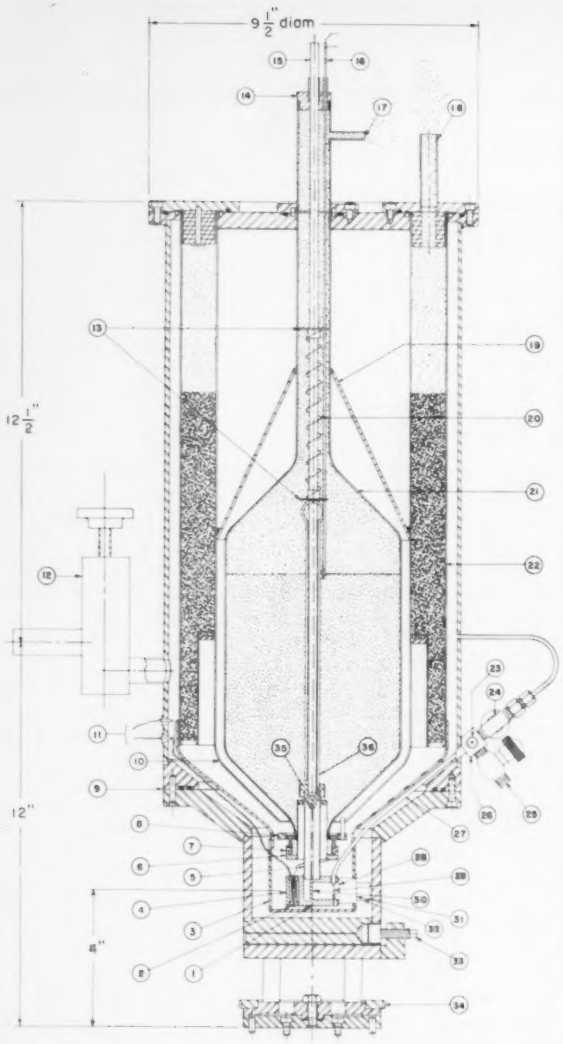

FIGURE 1. *Vertical section through the X-ray diffractometer cryostat.*

(1) Thermocouple, (2) heater bobbin, (3) radiation shield, (4) copper block, (5) thin-walled support tube (stainless steel), (6) copper ring, (7) soft-solder joint, (8) ring with centering pins, (9) flange with "o"-ring seal, (10) inner vacuum wall, (11) heater leads, (12) vacuum valve, (13) radiation baffle) (14) helium-vessel neck stopper, (15) block vent tube, (16) liquid-helium depth probe, (17) helium vent, (18) nitrogen fill-tube and vent, (19) radiation shield, (20) spacing spring, (21) helium vessel, (22) nitrogen vessel, (23) inlet-tube-heater terminal, (24) bypass valve, (25) sample-inlet valve, (26) manifold block, (27) sample-inlet tube (stainless steel), (28) Mylar plastic window, (29) sample-inlet-tube heater, (30) sample-deposition surface, (31) aluminum foil window (0.00035-in. thick), (32) opening for 0.025-in. thick beryllium X-ray window, (33) translation-adjustment screw, (34) rotational-alinement gear sector, (35) plug, (36) internal siphon.

vessel from that in the specimen chamber, was then cut away from the helium vessel at the lower end to reduce heat conduction to the liquid helium. A ring (8) with three centering pins was fitted to the lower end of the inner vessel. The pins contact the remaining portion of the inner wall and prevent lateral motion. They do, however, allow for a vertical component of relative motion so that the two vessels may contract independently when filled with cold liquids.

Replacing the original copper block is an assembly which makes it possible to introduce the thin-walled tube (5) between the bottom of the helium reservoir and the copper block (4) without changing the location of the deposition surface (30) relative to the windows and X-ray beam. The copper ring (6) is fitted with a ⅞-in. o.d. tube that extends for 1¾-in. up inside the helium reservoir. At the top of this tube is a second ring which becomes, in effect, the new bottom of the liquid helium vessel. The ⅝-in. o.d. tubing (5) of 304 stainless steel that supports the copper block is 2½-in. long. The wall thickness, originally 0.035 in., has been reduced to 0.010 in. over a length of 2 in. to reduce the cross sectional area of the heat path. Because of the low thermal conductivity of 304 stainless steel ($\sim 2 \times 10^{-3}$ watt cm^{-1} $°K^{-1}$), the heat flow along this path corresponding to a block temperature of 40 °K is only about 0.025 watt.

The plug (35) which is inserted through the neck of the cryostat is used to exclude liquid helium from the region of the block when it is to be heated. A diagonal passage through this plug connects the internal siphon (36) with the tube extending to the bottom of the space below and permits liquid trapped in this region to return to the helium reservoir. Another passage connects this region with the vent tube (15). These passages may not be visible when the figure is reproduced.

A new sample deposition block (4) was cut from a cylinder (1½-in. diam by ⅞-in. high) of electrolytic tough pitch copper, selected for its high conductivity at low temperatures. A ½-in. wide cut was made halfway through the cylinder, leaving a plane surface (30) on which samples are deposited. The block was gold-plated to provide a chemically inert surface that gives an X-ray pattern suitable for use as an internal standard.

The uncut portions of the cylinder above and below the deposition surface provide circular flanges around which the Mylar window (28) is cemented using an epoxy resin [3]. The window is 0.0007 in. thick and attenuates the copper K_α radiation ordinarily used by only 8.5 percent. It is vacuum-tight and readily supports a pressure differential of 1 atm. The one failure of this window occurred at a pressure difference of about 3 atm.

A 23-ohm Manganin resistor wound on a copper bobbin (2) is provided for heating the block. The carbon resistor, (100 ohm, ⅛ watt) used as the sensing element for the temperature controller, is mounted in a 1/16-in. hole drilled along the axis of the bobbin. The whole assembly is pressed into a ¼-in. hole in the copper block.

An inlet tube (27) connects the region enclosed by the Mylar window with the manifold (26) on the outside of the cryostat. Stainless steel tubing ⅛ in. in diameter with a 0.005-in. wall thickness is used.

To keep samples from freezing in this tube, it is lined with Teflon tubing through which is passed an elongated helix of #30 Nichrome wire (29). The inner end is grounded to the copper block and the outer is connected to a terminal (23) in the manifold so that a current may be passed through the wire if blockage occurs.

The bypass valve (24) may be opened while pumping to equalize pressures on the two sides of the Mylar window, and closed before the inlet valve (25) is opened to admit the sample gas. Since the cryostat turns through 90° while the X-ray pattern is scanned, flexible ⅛-in. annealed copper tubing is used to connect this valve to the stationary specimen preparation train, flow gages, manometer, and auxilliary vacuum pump.

Other features that have not been described in the text are identified in the legend of figure 1.

3. Temperature Controller

Numerous controllers have been described in the literature [4], but the one used to control the temperature of the specimen block differs from all of these and will be described briefly. It uses the 100-ohm carbon resistor in the heater bobbin as the temperature sensing element (fig. 2). The resistor forms one arm of a Wheatstone bridge which is set to balance at a resistance corresponding to the desired temperature. The servo amplifier from a recording potentiometer amplifies the output of the bridge and drives a two-phase reversible motor to set a variable autotransformer. In this way, heater power input is automatically increased or decreased until the desired temperature is reached. To improve the stability of the system, a rate signal is obtained from a small d-c generator on the shaft of the balancing motor. While the system is approaching the control point, this generator produces a voltage proportional to the velocity. A portion of this voltage is fed back to the amplifier input, phased so that, when amplified, it tends to drive the motor in the reverse direction. Thus, a braking torque is provided that is very effective in reducing the amount of overshooting at the control point.

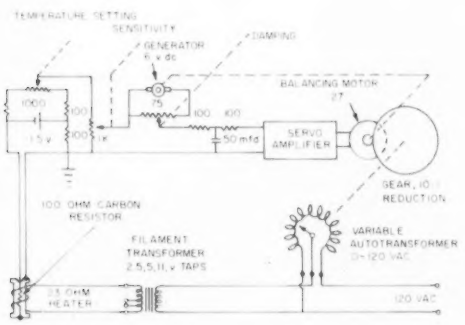

FIGURE 2. *Temperature controller circuit.*

In order to reduce the time required for the resistor to sense a change of power input, the compact ⅛₀-watt size is used. It is cemented into a ⅛₆-in. hole in the heater bobbin. One lead is soldered directly to the block, and the other is cut very short to decrease its heat capacity.

A separate resistor (56 ohm, 1 watt) is mounted in the block and used for measuring temperatures in the range below 30 °K. In addition, a thermocouple (Au +2.11 atomic % Co versus Cu) is used throughout the range 4.2 to 300 °K.

The use of carbon resistors in low temperature thermometry has been described by Clement and Quinell [5]. Two characteristics of these thermometers are their extreme sensitivity at low temperatures and the rapid decrease of sensitivity with increasing temperature. Thus, by measuring resistance to 1 part in 5,000, it is possible to detect temperature changes of 0.0001° at 2 °K, 0.01 °K at 20 °K, or 1.0 °K at 300 °K. In the present application, the inherent sensitivity cannot be fully utilized, and below 20 °K the precision of control is limited to ±0.1 °K. Above 20 °K the precision gradually decreases to about ±1°K at room temperature.

4. Operation

In order to fill the cryostat with liquid helium, the neck-stopper (14, fig. 1.) and the entire plug assembly are removed so that the transfer siphon can be inserted. When the inner vessel has been filled to approximately the level shown, the siphon is removed and the neck-stopper is replaced after drawing the plug (35) all the way up so that it remains in the neck tube to be cooled by the escaping vapor. The sample is usually introduced at this time by opening the inlet valve (25) and allowing the gas to flow in at a rate of 20 to 30 cm³/min (STP) until the thickness of the deposit is sufficient to reduce the intensity of the X-ray pattern from the gold substrate by a predetermined amount. When the block is to be heated, the plug is lowered and seated in the top of the tube (5) to exclude liquid helium. That trapped below the plug is returned to the reservoir through the internal siphon (36) by closing the vent (15) so that pressure develops in the well.

With helium out of the well, the block may be heated electrically, using the controller to maintain a desired temperature. The setting of the bridge is determined by referring to curves based on the semi-empirical equation of Clement and Quinell for the calibration of carbon resistance thermometers. Experience soon indicates the best settings for the sensitivity and damping controls.

The relationship between power input and block temperature for three refrigerants is shown in figure 3. Some heat reaches the block by conduction along the electrical leads and sample inlet tube even when the electrical power input is reduced to zero. As a result, the temperature of the block rises 10 to 20° above the temperature of the refrigerant. The internal siphon (36, fig. 1.), which was not a part of the system described by Henshaw, was introduced

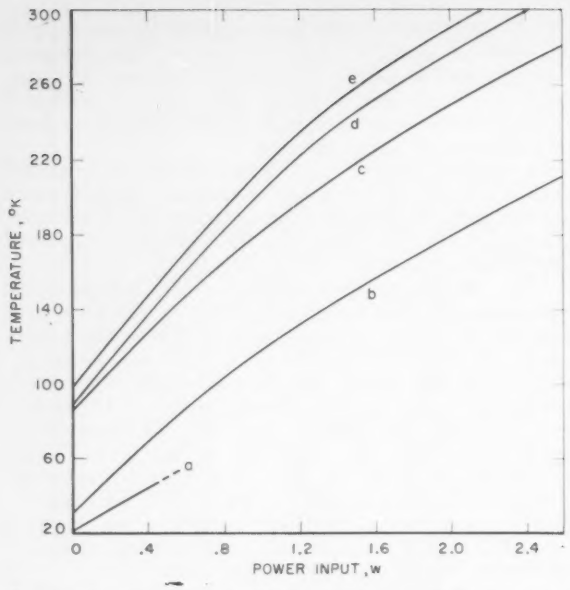

FIGURE 3. *Variation of block temperature with heater power input for (a) liquid helium, (b) liquid hydrogen, and (c) liquid nitrogen.*

For the last refrigerant, the effect of residual gas in the region below the plug is seen by comparing curve (c), obtained with nitrogen gas at 1 atm in the well, with curve (d), obtained by filling the region with styrofoam, and curve (e), obtained by evacuating the region to eliminate both conduction and convection.

in an attempt to control temperatures in the interval between the boiling point of the refrigerant and the zero-power intercept. By pumping on the block vent (15) through a needle valve, helium (for example) can be drawn in at a controlled rate. If desired, the automatic temperature controller may be used simultaneously. This method is effective down to 10 to 12°K. At lower temperatures two-phase flow evidently commences and results in discontinuous cooling.

The arrangement that has given the best results in the range 4.2 to 15 °K is a sliding-piston plug which is substituted for the plug shown (35, fig. 1.). It was hoped that any desired temperature could be reached by sliding the plug up or down to vary the effective length of the heat path along the thin-walled tube (5). However, with the block vent (15) closed to create a positive pressure, keeping helium from leaking around the piston, the lowest temperature reached with the plug all the way down is 12 °K. To reach lower temperatures it is necessary to provide an escape to the atmosphere for helium gas. The rate of leakage around the plug is determined by the rate at which gas is allowed to escape and this is easily controlled by a needle valve (not shown). Each full turn changes the block temperature by very roughly 0.5 °K. The temperature remains constant (± 0.1 °K) for periods of 10 min or more, and automatic control is available if desired. The valve is simply opened enough to give the lowest temperature required and, thereafter, the controller is used to adjust the heater input.

5. Application

Temperature was controlled in this way to obtain data on the lattice constant of neon at various temperatures in the range 4.2 to 22 °K (fig. 4) [6]. Values of the lattice constant were determined by the X-ray method except for that at the triple point, which was calculated from the density data of Clusius [7]. Both carbon resistors and the thermocouple were calibrated in place at the boiling point of helium, the triple point of hydrogen and the boiling point of hydrogen. In addition, readings from both resistors and the thermocouple were compared with the vapor pressure of hydrogen throughout the temperature range 10 to 20 °K. Temperature measurements are believed to be accurate to ± 0.1 °K and lattice constants to ± 0.001 A. The neon data demonstrate the importance of accurate control at temperatures below 20 °K. There are, of course, many other problems requiring temperature control that can be studied with this apparatus. For example, solid oxygen is known to exist in three forms, but, as far as we know, the structures of two of these and the effects of disorders that commonly occur, are still subjects for further study. It is hoped that this cryostat will contribute to the solution of these and other problems in the structure of low temperature solids.

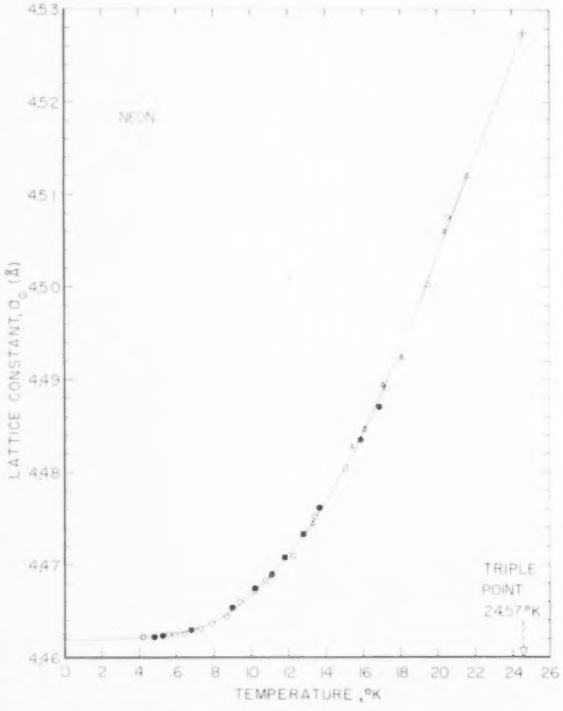

FIGURE 4. *The lattice constant of neon as a function of temperature, showing the reproducibility between three experiments.*

The value at 4.2 °K is the average of four measurements. That at the triple point is calculated from the density reported by Clusius.

6. References

[1] I. A. Black, L. H. Bolz, F. P. Brooks, F. A. Mauer, and H. S. Peiser, A liquid-helium cold cell for use with an X-ray diffractometer, J. Research NBS **61,** 367 (1958) RP2907.

[2] D. G. Henshaw, Atomic distribution in liquid and solid neon and solid argon by neutron diffraction, Phys. Rev. **111,** 1471 (1958).

[3] R. S. Hickman, R. W. Kenny, R. C. Mathewson, and R. A. Perkins, Liquid hydrogen targets of adhesive-bonded Mylar plastic, Rev. Sci. Instr. **30,** 983 (1959).

[4] R. D. Goodwin and J. R. Purcell, Direct-coupled power amplifier for cryostat heating control, Rev. Sci. Instr. **28,** 581 (1957). (Twenty-six references are cited.)

[5] J. R. Clement and E. H. Quinell, The low temperature characteristics of carbon-composition thermometers, Rev. Sci. Instr. **23,** 213 (1952).

[6] L. H. Bolz and F A. Mauer, Lattice constants and thermal expansion of solid Ne, A, Kr, and Xe, to be submitted to J. Research NBS.

[7] K. Clusius, Atomwärmen und schmelzwärmen von Neon, Argon, und Krypton, Z. phys. Chem. **B31,** 459(1936).

(Paper 65C4—75)

JOURNAL OF RESEARCH of the National Bureau of Research—Engineering and Instrumentation
Vol. 65C, No. 4, October–December 1961

Apparatus for Determination of Pressure-Density-Temperature Relations and Specific Heats of Hydrogen to 350 Atmospheres at Temperatures Above 14 °K*

Robert D. Goodwin

(June 20, 1961)

Method and apparatus are designed for more rapid determination of accurate, closely-spaced, PVT and specific heat data than realized by previous procedures. A sequence of pressure-temperature observations at nearly constant density is made by a modified Reichsanstalt method. Temperatures of the essentially adiabatic piezometer are regulated by electric heating under control of the measuring thermometer. Instruments for measurement and control are integrated with a high-pressure calorimeter for compressed liquid and fluid. Calorimetric experimentation is accelerated by use of an electronic battery for the calorimetric heat supply and of a d-c power regulator developed for automatic shield control. Details are given of the PVT calibrations, adjustment computations, and comparisons with independent data.

1. Introduction

The high-density physical properties of hydrogen are needed for technological applications [5, 10]. Thermodynamic functions may be computed from certain thermal data combined with a wide range of precise mechanical properties (PVT) and vapor-pressure data [1, 2, 3, 9]. The purpose of this paper is to describe the essential features of apparatus used to obtain PVT data for parahydrogen from 16 to 100 °K and from 2 to 350 atm, and to obtain specific heats of compressed liquid and fluid in the same range. Advent of high-speed digital computers renders practical the handling of a large quantity of data, produced by closely-spaced observations with accelerated methods to be described.

2. Experimental PVT Method

The PVT method and its numerous calibrations are emphasized in preference to the better-known calorimetric techniques, outlined below. The popular Burnett method for PVT determinations [17] is not suitable for compressed liquids [9]. That of Holborn and coworkers [20, 21, 22], termed the Reichsanstalt method [2], involves essentially direct measurement of each variable. As employed by Michels and coworkers, a sample of fluid of known PVT behavior at normal temperature is confined in the piezometer and pressure gage system at that temperature. Pressure of the sample then decreases rapidly with temperature of the piezometer [25]. In the Ohio State University modification for gaseous states, adjustments for obnoxious volumes of capillary and gage were eliminated by placing a valve in the cryostat. This necessitated an independent determination of the amount of sample following every P–T determination [24]. For liquid states they employed a boiling hydrogen thermostat. Successive small portions of the sample were released from the piezometer or "pipet" to obtain a series of isothermal P–v determinations from a given filling, each P–v point again requiring an independent volumetric determination [23].

Average time per determination is greatly reduced in the present method. Temperature of the nearly adiabatic pipet is varied to obtain a series of P–T determinations at nearly constant density. Temperatures are automatically controlled at exact, integral values, to permit handling the data as isotherms. Only one determination of the amount of sample is required following each experimental "pseudo-isochore". The portion of the total sample which was in the pipet during each P–T determination is calculated by subtracting the computed amounts residing simultaneously in capillary and diaphragm cell under those conditions. For this small adjustment, the known and estimated PVT behavior of normal hydrogen is employed.

With reference to figure 1, a sample of the experimental fluid is confined by valve C–4 to the following system: the heavy-walled copper pipet, the stainless "transition" capillary tube in the cryostat, the capillary tubes and valves at room temperature, and the pressure-sensitive diaphragm cell (N. P. D.). Volumes of these elements are calibrated independently. The latter transmits pressure of the fluid to the oil of a piston-type, deadweight gage. With reference to figure 2, liquid hydrogen refrigerant resides in the tank. The pipet is cooled strongly as required by liquid hydrogen reflux action from hydrogen gas introduced to the thin-walled, stainless steel "reflux" tube supporting the pipet. For automatic temperature regulation by electric heating, under control of

*Contribution from the Cryogenics Engineering Laboratory, National Bureau of Standards, Boulder, Colo.

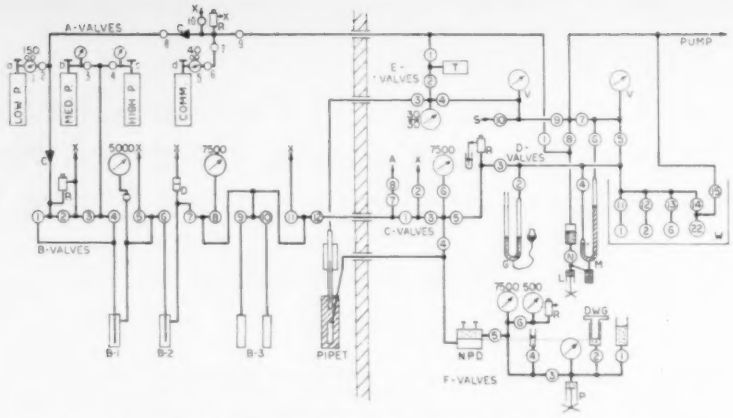

FIGURE 1. *Pneumatic apparatus for PVT determinations.*

A, Connection to thermal conductivity analyzer.
B-1, Absorbent bomb at 76 °K.
B-2, Iron-oxide, ortho-para catalyst bomb at 19.6 °K.
B-3, Thermal pump bombs.
C, Check valves
COMM., Commercial hydrogen.
D, Bursting disk.
DWG, Dead weight gage.
G, Gas buret.
L, Mercury leveling screw.
M, Precision manometer.
NPD, Null pressure detector.
P, Oil press.
R, Relief valves.
S, Sampling connection.
T, Reflux gas dose tank.
V, Philips vacuum gauges.
W, Water-bath thermostat.
X, Exterior vent lines.

the platinum resistance measuring thermometer, gas pressure in the reflux tube is reduced to provide controlled cooling by gas convection, aided by a copper rod suspended in this tube.

An experimental run consists of measurement of a sequence of pressure versus temperature points, beginning at the lowest temperature. The total quantity of confined fluid then is determined by releasing it as gas into volumetric system *D* of figure 1 and measuring P, V, and T at about normal conditions, accounting also for the gas remaining in all obnoxious volumes and in the pipet at this pressure. Experimental time required for filling and emptying the pipet is greatly reduced through capability of the commercial, null-pressure diaphragm instrument to withstand high-pressure imbalance without damage. About 30 points on a pseudo-isochore are determined routinely in 8 hr by 2 or 3 men.

3. Sample Preparation, Handling, and Analysis

By mass-spectral analysis, electrolytic hydrogen in clean steel cylinders at 2,000 psig contains less than 5 ppm helium and 100 ppm air, respectively. The preparation system on the left of figure 1 has three functions. Impurities are absorbed at 76 °K in B–1 on 20 ml of 1.6 mm diam extrusions of "molecular sieve" silica [71]. The paramodification of hydrogen is produced catalytically in B–2 at 19.6 °K on 10 ml of "30–100 mesh" particles of an iron oxide, batch 48–C, used in activity studies [72]. Small disks of sintered stainless steel retain the fine solids in their containers. Two stainless steel bombs, B–3, each of about 20 ml capacity, may be immersed in liquid nitrogen to provide a two-stage, thermal pump for boosting the parahydrogen pressure. Solidification of hydrogen at the catalyst is avoided by placing the catalyst ahead of these pumps in the train. The hydrogen cylinders, preparation system, liquid hydrogen transport Dewar, cryostats and vacuum pumps are separated from the instrument room by an explosion-proof wall. Valve manifold C in the instrument room uses a bourdon gage as a doser for filling the pipet to selected densities and for controlling release of the pipet sample to the gasometer system *D*.

Systems B and C of figure 1 are assembled with 1/16-in. o. d. stainless steel tubing and high-pressure midget valves with solid stems and polytetrafluoroethylene O-ring packings. Shop-fabricated gage connectors force a small, drilled, metal cone against a conical recess on the gage stem. This special fitting is necessary to avoid contamination of the gas. Bourdon gages for hydrogen must be phosphor-bronze, beryllium-copper, or type 316 stainless steel [75].

Analysis for parahydrogen is performed on gas bled from valve C–8 at 100 ml NTP/min through a thermal conductivity instrument [58]. Calibration depends upon parahydrogen produced independently. In preliminary studies the rate of conversion of para- to orthohydrogen in the pipet at pressures up to 4,500 psi was in the order of one percent per day at 76 °K and 25 to 30 percent per day at 275 to 300 °K. The vapor pressure of parahydrogen was measured at the beginning of a number of PVT runs [66]. Following one of the routine, 8-hr PVT determinations, the presence of parahydrogen again was confirmed by a vapor pressure measurement.

4. Cryostat and Piezometer

Descriptions and summaries of low temperature techniques are available [11, 12, 13, 14, 38, 46].

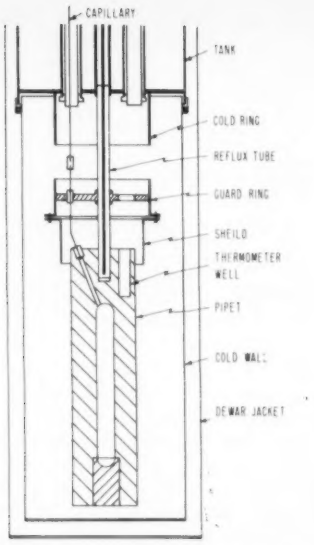

FIGURE 2. *Piezometer region of PVT cryostat.*
(Shield is misspelled in the above figure.)

Figure 2 shows a cross section of the lower portion of the cryostat. A 25-ml pipet sample cavity, 5/8-in. diam, is bored into a two-in. diam, solid copper cylinder 8.5-in. long. To avoid oxidation, the plug is brazed with helium in the cavity. Metal stress is about one half the internal pressure. Helical grooves on the cylinder carry a 32-gage, 500 Ω constantan wire heater. The platinum thermometer is tinned and cast into the pipet with Rose's alloy. Above the pipet on the supporting, thin-walled, stainless steel tube, a guard ring thermally tempers electric wires leading to and wound on the pipet; the ring is automatically controlled at pipet temperature by a gold-cobalt versus copper thermocouple [40, 44] and a 36-gage, 100 Ω constantan wire heater. A cold ring, integral with the refrigerant tank, tempers electric wires entering from room temperature. Before it was mounted and wound in the cryostat, the bundle of 36-gage, low-level wires was constructed as a unit with all wires lightly varnished together parallel in a plane to insure good thermal contact on the rings. The levels of cooling through the reflux tube which do not disturb the temperature-versus-pressure relationships are determined experimentally. About 10 milliwatts cooling normally is used.

An evacuable copper can, soldered to the tank with Rose's alloy, encloses the pipet. A Dewar vacuum jacket immersed in an open Dewar of liquid nitrogen protects the can and the tank. A permanent liquid hydrogen transfer line with built-in valves enters the cryostat refrigerant tank through an O-ring seal, with the amount of refrigerant in the tank shown by an electronic level-indicator instrument. Suitable valves and safety devices on the vent from the tank permit the use of a rotary oil pump to attain the triple-point temperature of the refrigerant.

5. Measurement of Sample Volume

5.1. Normal Pipet Volume

This volume is required for computation of density. By ignoring the adjustments contained in eqs (10.1–1) and (10.3–1) there is obtained the rough approximation for sample density,

$$\sigma \approx (P_m/RT_b)(V_g/V_o), \qquad (5.1\text{–}1)$$

where P_m, T_b and V_g refer to the gasometry system and V_o is pipet volume. Whereas the ratio V_g/V_o dominates the computation of eq (10.3–1), it is a practical convenience to perform absolute calibrations.

The pressure and temperature-dependent volume of the pipet is required. Connection to the pipet cavity is made with a 3-in. length of 0.35 mm stainless capillary brazed to the pipet drill hole, figure 2. The pipet was briefly tested to 8,000 psi. A midget valve was attached to the capillary, the pipet evacuated, and freshly boiled water admitted to the pipet. The three determinations yielded an adjusted volume of 25.83 ± 0.016 cm^3 at 25 °C. Volume at room temperature after mounting in the cryostat was determined by expanding hydrogen from the pipet at about 1,000 psi into the gasometer system of section 6. Seven determinations yielded adjusted volume 25.854 ± 0.037 cm^3 at 25 °C. Following two series of high-density experiments for PVT data to 5,400 psi, low-density experimental results violated general, low-density, limiting gas behavior. Six redeterminations of pipet volume by gas expansion yielded normal volume 25.913 ± 0.009 cm^3 relative to the gasometer volumes, in agreement with deductions from low-density behavior. The first series of PVT experiments is rejected, and the increase of molal volume by factor 1.00263 is applied to all other data. The annealed pipet is thus assumed to have deformed in use. With this correction, the estimate of error in normal pipet volume is 0.5 parts per thousand.

5.2. Elastic Stretching of Pipet

Circumferential and longitudinal stresses in a closed-end cylinder are, respectively,

$$S_c = kP/(R-1) \text{ and } S_l = P/(R^2-1), \qquad (5.2\text{–}1)$$

where P is excess internal pressure, R is the ratio of external to internal diameters, and k incorporates both end-effects and relative behavior of thick walls. With modulus of elasticity E, relative diameters, lengths, and volumes are, respectively,

$$D/D_o = 1 + kP/E(R-1) \qquad (5.2\text{–}2)$$

$$L/L_o = 1 + P/E(R^2-1) \qquad (5.2\text{–}3)$$

$$V/V_o - 1 = (P/E)[(R^2-1)^{-1} + 2k(R-1)^{-1}]. \qquad (5.2\text{–}4)$$

The temperature-dependence of E from [73] in T °K is

$$E=1.15\cdot 10^{6}[1-4.35\cdot 10^{-4}T],\ \text{atm}, \quad (5.2\text{–}5)$$

and the behavior of k by comparison with [70, 74, 79] is

$$k=a(R-1)[(R^2+1)/(R^2-1)+m]=1.11 \quad (5.2\text{–}6)$$

by introducing $R=3.2$, $a=1/3$ for end-effect and $m=0.3$ for Poisson's ratio. Within the accuracy of above estimates, therefore,

$$\lambda\equiv V/V_o=1+1\cdot 10^{-6}[1+4.35\cdot 10^{-4}T]\cdot P_{\text{atm}}. \quad (5.2\text{–}7)$$

5.3. Thermal Contraction of Pipet

Thermal expansivity of copper [78] in the form $a\equiv(L_o-L)/L_o$ as a function of temperature is used to compute a table of V/V_o versus temperature. For use with computing machines, this is fitted by a quadratic polynomial on the Kelvin temperature scale,

$$V/V_o=a+bT+cT^2,$$

$$V_o=25.913\ \text{cm}^3;\ a=0.990069;\ b=1.667\cdot 10^{-6};$$

$$c=1.317\cdot 10^{-7}. \quad (5.3\text{–}1)$$

6. Measurement of Amount of Sample

6.1. The Gasometer

The fluid contained in the pipet, the capillary, and the diaphragm cell is released into the gasometer system D (fig. 1). This is a set of spherical glass standard volumes in a precision water-bath thermostat, and a valve manifold with precision mercury manometer [48] in a circulating-air cabinet. Elevation of each arm of the leveled manometer is read to ±0.05 mm by a highly reproducible lightbeam and photocell arrangement. A standard volume is selected such that the pressure is in the upper range of the manometer; i.e., 500 mm or greater. The instrument room temperature is controlled to about ±0.5 °C. To compromise between low obnoxious volumes and adequate pumping speeds, the manifolds are ¼-in. copper tubing of 0.19-in. diam bore. For leak-free behavior, bellows-sealed valve seats and gaskets are a plasticized vinyl chloride polymer. Bellows volume increase per single turn is 0.15 cm³. This adds to standard volumes of 10 liters or more used for most determinations. Ionization gages serve for vacuum leak testing.

6.2. Gasometer Calibration

Volumes of the 1- and 2-liter spherical glass flasks are determined by weighing them with water on a 3-kg analytical balance against class Q weights. The 6-liter flask is weighed on a 20-kg single-beam platform balance against calibrated weight slugs. Adjustment is made for air buoyancy, water density, and thermal expansion of the borosilicate glass [76]. Volumes at 300 °K are given by the second column of table 1.

TABLE 1. *Calibration of gasometer flask volumes*

Nominal volume	Water weighing	Gas expansion	Assigned
	ml	*ml*	*ml*
1 L	994.48	(994.48)	994.11
2 L	2,036.35	2,037.5±0.7	2,036.7
6 L	6,429.1	6,427±3.0	6,427
22 L	.....	21,226±3.0	21,226
Ratio, 2 L/1L	2.0477	2.0488	.....

After determination of all manifold volumes including the manometer, the 2-liter flask is calibrated by gas expansion relative to the 1-liter flask; each successive flask then is calibrated relative to the sum of all smaller flasks. With all adjustments the results shown in the third column are obtained. Absolute volume standard is selected as the sum of volumes of the 1- and 2-liter flasks by water weighing, and the ratio of these two volumes by gas expansion is selected for assigning the values shown in the last column. Pressure-dependence of the flask volumes was computed from physical dimensions and mass of the individual flasks and the modulus of elasticity [76]. The nearly uniform results were confirmed experimentally upon a flask filled with water extending into a capillary neck,

$$(1/V)(dV/dP)=1\cdot 10^{-4}\ \text{atm}^{-1}. \quad (6.2\text{–}1)$$

6.3. Adjustment for Capillary and Cell

The amount of sample in the pipet is the total amount behind valve 4 of figure 1, determined by gasometry, less amounts in capillaries and in the diaphragm cell under conditions of measurement for each P–T point. The rapid experimental method is justified provided these latter amounts can be estimated with sufficient accuracy. This is attained with a diaphragm cell volume which is small relative to the pipet, and by utilizing known and estimated gas-imperfection behavior of normal hydrogen.

A volume of 0.655 cm³ for capillary tubing and diaphragm-cell exterior to the top of the cryostat and up to the pipet valve C–4 is obtained by weighing mercury out of the tubing and by finding differences with suitable gas-expansion methods. The quantity of hydrogen in these obnoxious volumes is computed from their temperatures, the pressure, and the compressibility factor for normal hydrogen [65].

The volume of the 71-cm-long, transition capillary from the top of the cryostat to the guard ring is $V_c=0.0672$ cm³, or 0.26 percent of pipet volume. The amount of fluid in the capillary is computed by calculating the temperature T_x, corresponding to any position at a fraction x of capillary length from the ring at pipet temperature T_o to the top of the cryostat at room temperature T_1, from thermal conductivity K of stainless steel [77] by the relation,

$$x=\left[\int_o^{T_x} K dT-\int_o^{T_o} K dT\right]\cdot\left[\int_o^{T_1} K dT-\int_o^{T_o} K dT\right]^{-1} \tag{6.3-1}$$

The number of gram moles of fluid in the capillary is

$$N_c=(PV_c/RT_o)\theta \tag{6.3-2}$$

where

$$\theta\equiv T_o\int_o^1 dx/T_xZ_x. \tag{6.3-3}$$

Indices o refer to the ring or pipet, x to relative position along the capillary, and $Z\equiv Pv/RT$ where v=molal volume. By known [23, 64, 68, 69] and extrapolated [3] data for Z, the capillary factor θ for hydrogen is determined at a sufficient number of sensitive points for smoothing, taking note of liquid-vapor discontinuities; results are summarized by figure 3. The ratio of amount of fluid in the transition capillary to amount in the pipet is necessary for an estimate of required accuracy. This ratio is $(V_c/V_o)\cdot\phi$, where $\phi\equiv Z_o\theta$ is summarized by figure 4. Due to the small value of V_c/V_o, a ten percent error in ϕ would correspond to a relative error well under 0.03 percent in density of the pipet sample at temperatures ≤ 100 °K.

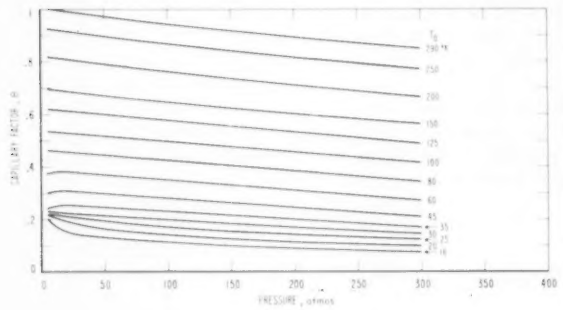

FIGURE 3. *Capillary factor, θ.*

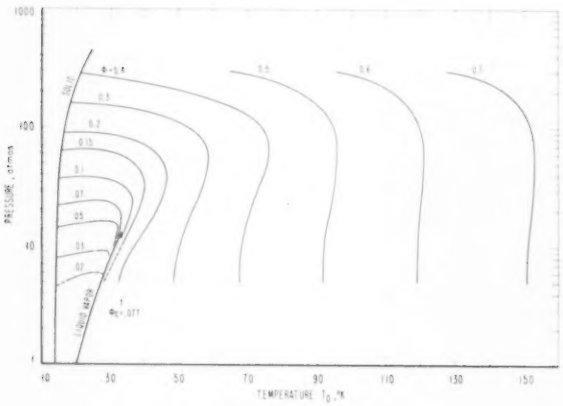

FIGURE 4. *Capillary relative content, φ.*

7. Measurement of Pressure

7.1. Piston Gage and Diaphragm Cell

The commercial, dual-range, precision, dead-weight gage and null-detector operate in the oil-filled F-manifold, figure 1 [52, 53, 57, 59]. The diaphragm, with adjustable electric contacts to indicate null position, is centered by use of an open-tube manometer. The oil pressure is adjusted to the experimental gas pressure with the screw-type oil press P. Prior to placing weights on the piston gage, the approximate pressure is read from bourdon gages.

Piston diameters of about 0.182 and 0.407 in. are measured with a light-wave micrometer to ± 5 millionths of an inch. Tolerance on the weights, determined by comparison with class S standards [54], decreases from 0.05 percent on the 1 psi weight to 0.002 percent on the 1000 psi weights. Adjustments to gage readings are made for temperature, pressure, acceleration of gravity, and barometric pressure. Observed sensitivity of pressure measurement with the small piston varies from under ± 0.05 psi below 500 psi to under ± 0.5 psi at 5000 psi.

As compared with known diaphragm-detectors [49, 61], the commercial instrument used here withstands extreme pressure imbalance without damage, but exhibits temporary hysteresis effects up to about ± 0.05 psi. A measured shift of null-point with absolute pressure is applied by the relation

$$P_{\text{gas}}=P_{\text{barom}}+(1.00002)P_{\text{oil}}. \tag{7.1-1}$$

Table 2 summarizes estimates of accumulated errors at different pressures.

TABLE 2. *Estimates of accumulated pressure errors*

Gage pressure, atm	2	20	200
	Error, atm×10⁴		
Barometer	0.50	0.50	0.50
Diaphragm cell	4.00	4.00	4.00
Piston-cylinder diameter	0.06	0.60	6.00
Calibration of weights	.67	1.52	4.07
	5.23	6.62	14.57
Relative error $(\delta P/P)\cdot 10^3$	2.6	0.33	0.073

Thermal equilibrium of the fluid sample, following a step-increase of temperature, is found by pressure observations to be established nearly as rapidly as the heating rate of the massive pipet. Occasional pressure balances are taken an hour apart to confirm this inference from the steady behavior of single observations.

7.2. Adjustment for Capillary Column

The column of cold fluid standing in the transition capillary tube produces an additional pressure P_c at the pipet,

$$P_c/P=JML_c\theta/RT_0$$

using symbols of section 6.3, pressure conversion factor J, molecular weight M, and capillary length L_c=71 cm. Since $JML_c/R=1.68 \cdot 10^{-3}$ °K for hydrogen, the adjustment for capillary column pressure is negligible.

8. Measurement of Temperature

8.1. Method and Instruments

The potentiometric method of figure 5 is employed with a 25-ohm platinum resistance thermometer calibrated by the NBS Temperature Physics section and a six-dial microvolt potentiometer [41, 42, 46]. The low-impedance, unsaturated standard cells are protected from occasional extreme temperatures of the laboratory by two concentric boxes of 1/2-in. aluminum in a plywood case [43]. The upper potentiometer current supply is stabilized by placing a lead-acid battery across an isolated, rectified, and filtered a-c source [60]. A 25-v, 200 amp-hr, thermally insulated and shielded battery, of a similar, low internal-discharging type, supplies the stable thermometer currents which flow in the calibrated precision standard resistors. The microvolt switch is wired so that the thermometer potential connections to the potentiometer can be reversed when the thermometer current is reversed. Microvolt galvanometer amplifiers with floating input circuits are coupled to 50-μa panel galvanometers in suitable damping and range-changing circuits. To minimize spurious effects in the thermometer and thermocouple potential circuits, the continuous copper wires from the pipet in the cryostat are joined by a special solder [45] to untinned, copper cable wires near the cryostat on copper lugs in an iron-shielded, heavy aluminum box. The cryostat wires and shielded cables run in iron conduits. The cryostat and all electrical instruments are interconnected and grounded to the earth with heavy copper conductors.

8.2. Procedure and Calibration

When the instrument room air conditioner is started, spurious potentials up to $\pm$0.1 microvolt arise in the galvanometer circuit. These potentials are observed by use of an internally-shorted emf position on the potentiometer and are bucked out at the galvanometer amplifier. When the cryostat is cooled with liquid hydrogen, a 0.35-μv spurious potential, which is nearly independent of pipet temperatures up to 40 °K and increases with higher temperatures, appears across the thermometer potential leads in the absence of thermometer current. Potential measurements with reversed thermometer currents show the effect to be independent of current.

Thermometer currents are adjusted to exact integral milliampere values. To a corresponding, tabulated, thermometer potential is added the spurious thermometer potential to obtain a potentiometer dial setting yielding an automatically-controlled, integral-valued temperature. A thermometer current of 5 ma is used at temperatures below 35 °K; 2 ma, from 35 to 75 °K; and 1 ma, at 75° and above. Thermometer heating by the 5 ma current produces an error of 0.0007 °K at 40 °K. All measurements occur in the low range of the potentiometer.

The specified error limit of the potentiometer low range is 0.01 percent of reading plus 0.02-μv. The calibrated value of the 1-ohm standard resistor is 0.99999$\pm$0.00001 ohms. Apparently satisfactory agreement was found between the platinum thermometer calibration tables and measurements with above procedures for the ice-point and for vapor pressures of high-purity nitrogen and of parahydrogen, as described in section 11.

The accuracy of temperature measurements is summarized by table 3. It is based on the thermometer characteristic and currents, the potentiometer specifications, and a latitude of 0.05 μv for bucking out spurious potentials. Thermometer calibration uncertainties are not included.

TABLE 3. *Estimates of accumulated temperature errors*

T, °K	Thermometer			Potentiometer error, μv	Errors, δT, °K · 10^3		δT/T, $\times 10^6$
	i, ma	R, Ω	dR/dT		Potentiometer	External $\pm$0.05 μv	
15	5	0.049	0.0074	0.045	1.22	1.35	170
20	5	.112	.017	.076	0.89	0.58	74
40	2	1.07	.075	.234	.62	.13	19
76	1	4.65	.109	.485	.89	.09	13
100	1	7.25	.109	.745	1.37	.09	15

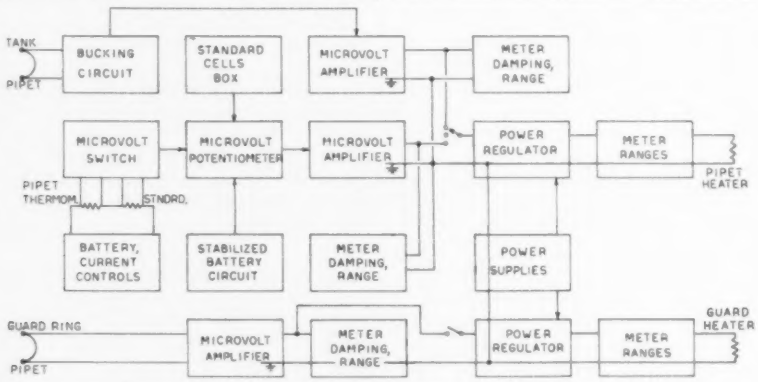

FIGURE 5. *Temperature measurement and control methods.*

9. Regulation of Temperature

Precisely controlled electric heating compensates for crudely adjusted, spontaneous cooling (section 4). The pipet temperature can be controlled [29] from a thermocouple, relative to the temperature of the refrigerant tank (upper left of figure 6), by a wide range microvolt bucking circuit, a microvolt amplifier [56] and a d-c power-regulator [50]. For all PVT measurements the pipet temperature is controlled from the platinum resistance thermometer and potentiometer. There is no perceptible noise at 0.0002 °K sensitivity. The accuracy of controlled temperature is equivalent to the described accuracy of measurement. To maintain a steady temperature during other operations with the potentiometer, the power regulator input signal switch is opened and the steady-state heating carefully adjusted by the power regulator control before undertaking such operations. If required, the above thermocouple control can be used. The guard ring temperature is controlled with similar instruments.

10. Computation of PVT Observations

10.1. Gasometry

The number, N, of gram moles of hydrogen contained behind pipet valve C–4 is calculated by the relation,

$$RN/P_m=[(EV_g+V_w)/T_w+V_a/T_a + V_b/T_b]/Z_{w,m}+V_o/T_oZ_{om}, \quad (10.1\text{–}1)$$

where P_m is mercury manometer pressure in atmospheres,

R=82.057 cm³ atm/g mol deg K,

$$P_m=KgDL_m, \quad (10.1\text{–}2)$$

K=0.986923.10⁻⁶ atm cm²/dyne [4],

g=979.615 dyne/gram in this laboratory room,

$$D=13.5948-0.00245 \cdot t_m,\ g/\text{cm}^3 \text{ [4]}, \quad (10.1\text{–}3)$$

t_m=manometer mercury temperature, °C,

L_m=manometer mercury height, cm (brass scale),

$$E=\text{glass volume/pressure coefficient} = 1+10^{-4}(P_m-0.825), \quad (10.1\text{–}4)$$

T_a=air-bath manifold temp, °K,

T_b=NPD temp, °K,

T_o=pipet temp, °K,

T_w=water-bath temp, °K,

V_a=vol of air-bathed manifold and manometer, 59.66 cm³,

V_b=vol of lines, gasometer to C-valves, including gage, 22.37 cm³,

V_g=vol of glass bulbs used, cm³,

V_w=vol of water-bath manifold, 13.00 cm³,

V_o=vol of pipet, cm³,

$$V_o/T_o=25.913[0.990069/T_o+1.667.10^{-6} +1.317.10^{-7} \cdot T_o], \quad (10.1\text{–}5)$$

$$Z_{w,m} \text{ (at } T_w \text{ and } P_m)=1.000044+0.000555P_m, \quad (10.1\text{–}6)$$

$$Z_{o,m} \text{ (at } T_o \text{ and } P_m)=1.0007 -1055/T_o^3 \text{ for } T_o \geq 40 \text{ °K}. \quad (10.1\text{–}7)$$

10.2. Pressure

The pipet fluid pressure P in international atmospheres is

$$P=0.0680457P_g+P_b \quad (10.2\text{–}1)$$

where

P_g=deadweight oil gage pressure in psig,
P_b=barometric pressure in atm,

$$P_g=k(g/g_s)[1-2.4 \cdot 10^{-5}(t_g-20 \text{ °C})]\,[1+ 4.2 \cdot 10^{-8}P_g] \cdot [\text{Nominal wt psi}]. \quad (10.2\text{–}2)$$

k=1.00002, eq (7.1–1),
(g/g_s)=979.615/980.665,
t_g=deadweight gage temperature, °C,

$$P_b=KgD \cdot L_b \text{ as in eq (10.1–2)}, \quad (10.2\text{–}3)$$

L_b=barometer height, cm,
t_b=barometer temp, °C.

10.3. Density

Density, σ, g moles cm³, is calculated by

$$\sigma V_o=N-(P/R)[V_c\theta/T_o+V_d/Z_dT_d] \quad (10.3\text{–}1)$$

where

T_d=temperature NPD, °K,
T_o=pipet temperature, °K,

$$V_o=25.913\ \lambda[0.990069+1.667 \cdot 10^{-6}T_o+ 1.317 \cdot 10^{-7}T_o^2], \quad (10.3\text{–}2)$$

V_c=0.0672 cm³,
V_d, volume of NPD and warm capillary=0.655 cm³,
Z_d, for gas at P and room temperature in V_d is

$$Z_d=0.99990+0.000623447\ P, \quad (10.3\text{–}3)$$

λ, eq (5.2–7),
θ, eq (6.3–3) and figure 3.

11. Checks on PVT Calibrations

11.1. Thermometry Fixed Points

Vapor pressures of a commercial, high-purity nitrogen and of parahydrogen were measured prior to the PVT experiments. Examination of experimental technique later revealed failure to compensate some of the spurious potentials. Determination of these potentials provided adjustments, estimated accurate within 0.005 °C, which have been applied in preparing table 4.

TABLE 4. *Thermometry fixed point observations**

P, mm [a]	T_{obs}	T_{lit}	ΔT
Vapor pressure of nitrogen [b]			
625.05	75.732	75.730	−0.002
625.42	75.741	75.735	−0.006
626.03	75.744	75.743	+0.001
631.75	75.825	75.816	+0.009
631.68	75.826	75.815	+0.011
Vapor pressure of parahydrogen [c]			
626.33	19.639	19.632	+0.007
626.72	19.645	19.634	+0.011
626.90	19.650	19.635	+0.015
628.18	19.656	19.642	+0.014
629.12	19.656	19.646	+0.010

*All temperatures in deg K on NBS 1955 scale.
[a] Mercury column height reduced to 0 °C at standard gravity.
[b] G. T. Armstrong, 1954.
[c] Hoge and Arnold, 1951.

11.2. Elevated Vapor Pressures

Initial PVT points of several runs were taken at saturation conditions to check instrumentation. If the substance is nearly pure parahydrogen, the observed pressure-temperature relations should agree with those of Hoge and Arnold. Table 5 presents

TABLE 5. *Elevated vapor-pressures observations*

P_{obs}, atm			Data from Hoge and Arnold [a]	
T °K	II	III	P, atm	dP/dT
22	.....	1.612	1.614	0.417
23	.....	2.069	2.071	.498
24	.....	.....	2.614	.587
25	.....	3.246	3.249	.685
26	3.978	3.983	3.985	.790
27	4.832	4.829	4.832	.904
28	5.785	5.792	5.795	1.026
29	.....	6.886	6.889	1.162
30	.....	.....	8.121	1.304
31	9.499	9.502	9.500	1.459
32	11.051	.....	11.047	1.643
32	11.051	.....	11.047	1.643
32	11.052	.....	11.047	1.643

[a] Data of Hoge and Arnold interpolated to NBS 1955 temperature scale.

observed vapor pressures of parahydrogen from the series II compressed liquid runs and from the series III low-density runs in the vapor and gaseous region. Data of Hoge and Arnold are interpolated to the NBS 1955 temperature scale of the present work. Temperature deviations corresponding to pressure deviations in series II range from 0.0098 deg at 28 °K to 0.0030 deg at 32 °K. The series III range is from 0.005 deg at 22 °K to 0.003 deg at 32 °K.

11.3. PVT Data for Normal Hydrogen

The first PVT run was made with normal hydrogen for comparison with known data, table 6. The

TABLE 6. *PVT observations on normal hydrogen*

T, °K	P, atm	v, cm³/mol	Z_{exp}	$1.0026 \cdot Z_{exp}$	Z_{lit}
28	30.869	30.443	0.4090	0.4101	0.4093[a]
30	45.357	30.460	.5612	.5627	.5616[a]
32	59.738	30.476	.6933	.6952	.6945[a]
36	88.443	30.508	.9134	.9160	.914*[b]
40	116.969	30.538	1.0883	1.0911	1.0902[b]
45	151.884	30.574	1.2576	1.2609	1.259*[b]
50	186.213	30.607	1.3892	1.3928	1.3928[b]

[a] Friedman and Hilsenrath, private communication.
[b] Johnston and White, Trans. ASME **72,** 785 (1950).
*Nonlinear interpolation.

known data have been interpolated linearly except where indicated. Present results for Z in column 4 are multiplied by 1.0026 in column 5 as an adjustment for the pipet deformation which occurred at an unknown time during the experiments. Deviations of the former results are within 0.07 to 2.6 parts per thousand; of the latter within 0.00 to 2.2 parts per thousand.

11.4. Virial Coefficients

Corresponding to the virial equation,

$$Z \equiv Pv/RT = 1 + B/v + C/v^2 + \cdots, \quad (11.4\text{–}1)$$

the data function,

$$\phi \equiv RT(Z-1)v = RTB + RTC/v + \cdots, \quad (11.4\text{–}2)$$

exhibits satisfactory linear dependence on density at each temperature when the recalibrated pipet volume, $V_0 = 25.913$ cm³ is used for computation of experimental densities below critical. Unsmoothed values of RTB and RTC, determined by least squares, are given by table 7. These new data are equivalent to an equation of state for parahydrogen at densities up to 9 g mol/liter. For comparison are given values for normal hydrogen calculated from the smoothed table 19 of H. W. Woolley et al. [69], and values for RTB only, smoothed by us from the "smoothed" table CIV of A. S. Friedman [19]. Negative third virial coefficients in the latter table below 50 °K suggest that corresponding second virial coefficients are too small in absolute value. Our closely-spaced data suggest a so-called lambda-point maximum in the third virial coefficient at the critical temperature. The criteria of its validity have not been investigated. Concerning comparison of results, it recently has been shown that second virial coefficients for parahydrogen may be about 1 percent smaller in absolute value than for normal hydrogen at liquid hydrogen temperatures, in

agreement with these results [63]. Quantitative study of the ϕ-density behavior before and after correction of the pipet volume suggests accuracy of volumetric calibrations within one part per thousand.

TABLE 7. *Virial coefficients, parahydrogen*

Units of cm³, g mol, atm, deg K

	$-RTB\cdot10^{-5}$			$RTC\cdot10^{-6}$	
T, °K	*Exp*	(a)	(b)	*Exp*	(a)
24	2.229*	2.247	2.20	3.053*	.....
25	2.185*	.....	.....	3.432*	.....
26	2.139‡	2.159	2.11	3.273‡	.....
27	2.098	.....	.....	3.519	.....
28	2.059	2.075	2.02	3.647	.....
29	2.023	.....	.....	3.826	.....
30	1.987	1.996	1.95	3.938	.....
31	1.952	.....	.....	4.021	.....
32	1.917	1.921	1.88	4.096	.....
33	1.883	.....	.....	4.124	.....
34	1.848	1.849	1.81	4.110	4.171
35	1.814	.....	.....	4.103	.....
36	1.780	1.781	1.75	4.073	4.089
37	1.747	.....	.....	4.043	.....
38	1.714	1.715	1.70	4.020	4.020
39	1.683	.....	.....	3.998	.....
40	1.651	1.653	1.64	3.986	3.962
42	1.591	1.591	1.59	3.934	3.914
44	1.533	.....	.....	3.920	.....
46	1.478	1.473	1.49	3.922	3.846
48	1.423	.....	.....	3.929	.....
50	1.369	1.360	1.40	3.926	3.811
55	1.239	1.224	1.28	3.971	3.804
60	1.116	.....	1.16	4.074	.....
65	0.992	.....	.....	4.143	.....
70	.873	.....	0.94	4.232	.....
75	.762	.....	.....	4.414	.....
80	.647	.....	.65	4.514	.....
85	.531	.....	.....	4.587	.....
90	.417	.....	.40	4.688	.....
95	.310	.....	.....	4.849	.....
100	.205	.....	.14	5.007	.....

[a] H. W. Woolley et al., J. Research NBS **41**, 379 (1948) RP1932, normal H_2.
[b] A. S. Friedman, Ohio State dissertation (1950), normal H_2.
*Based on only two data points.
‡Based on only three data points.

12. Comments on Overall PVT Accuracy

Requests for a statement of overall accuracy of data in the form $Z \equiv Pv/RT$ are commonplace. This accuracy depends not only on calibrations, but also on all the adjustment computations and the particular conditions defining the state of the fluid. The relative error in Z is the sum of relative errors in experimental variables,

$$\frac{\delta Z}{Z} = \frac{\delta P}{P} + \frac{\delta v}{v} - \frac{\delta T}{T}.$$

Estimation of pressure errors is indicated by section 7.1. and table 2. The complexity of error estimates for molal volume, v, is appreciated by reference to eq (10.3–1). In view of sections 5 and 6, table 1, and the unpublished details of calibration and adjustment of obnoxious volumes, we venture the experimentalist's opinion that error in v generally is under two parts per thousand. Temperature errors, in view of tables 3, 4, and 5, are within 0.02 °C except near 14 °K, comparable to uncertainty in the low temperature scale [38]. Value of the gas constant used for present computations is $R = 82.057$ cm³ atm/g mol deg. It may be noted that at high densities, any isotherms of pressure as a function of density are highly sensitive to errors in density, due to the relatively incompressible state of the fluid, a situation giving spurious indications of low precision in the measurement of pressure.

13. Calorimetric Apparatus

13.1. Introduction

Measurements of the volume, mass, and temperature of a fluid sample are necessary to define the state corresponding to each specific heat determination. For high pressures the PVT pipet must be massive so that its volume will be calculable. The PVT data are obtained first because they are used for calibration of the volume of the thin-walled calorimeter as a function of temperature and pressure. Calorimetric methods have been reviewed [29] and the calorimetry of some compressed fluids described [28, 30, 33, 34, 35, 36]. The purpose of this section is to provide a brief description of some improved instrumentation and of the integration of calorimetric with PVT apparatus. Calorimetric calibrations will accompany the publication of results.

13.2. Cryostat and Calorimeter

The calorimeter resides in an additional cryostat of basic construction identical with that for the PVT pipet, with the high-pressure hydrogen capillary, vacuum, and liquid-transfer plumbing in parallel through suitable valves. Alternation of experiments requires no dismantling. Figure 6 is the calorimeter region of the cryostat, and figure 7 is the calorimeter section. All parts are copper except for

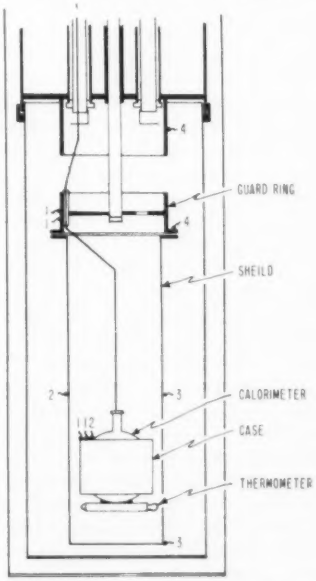

FIGURE 6. *Calorimeter region of calorimeter cryostat.*
(Shield is misspelled in the above figure.)

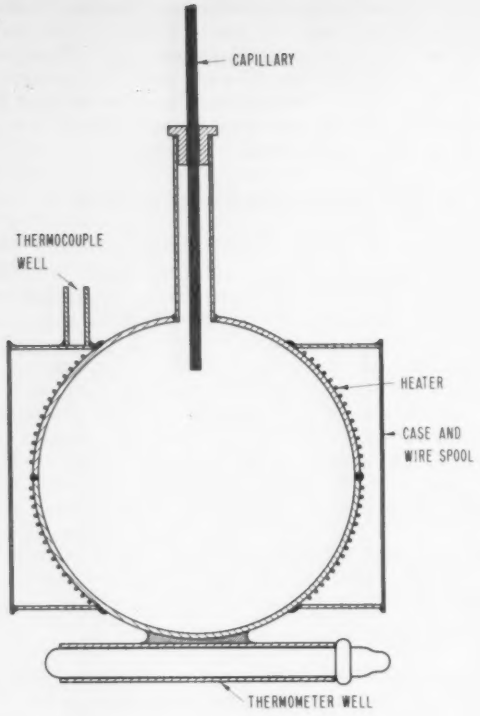

FIGURE 7. *Calorimeter section.*

sphere, capillary tube, and the guard-ring support tube. The 2-in. diam, type 316 stainless steel, spherical calorimeter has a nominal wall thickness of 0.06 in. It is fabricated from spun hemispheres, welded together, with addition of a 1-in.-long neck of ¼-in. tubing. The spherical shape is improved by expansion with water pressure. Yielding to a permanent volume increase of 10 percent was observed with a pycnometer surrounding the calorimeter. It occurred at pressures from 5,000 to 6,400 psi, corresponding to metal stress roughly 8.3 times these values. Elastic behavior following this deformation was $\Delta V/V\Delta P = 1.59 \cdot 10^{-5}$ atm^{-1}, corresponding roughly to a circumferential modulus $(3d/4t)$ $V\Delta P/\Delta V = 23 \cdot 10^6$ psi, where d is diameter and t is wall-thickness. After electroplating copper inside and outside to about 0.2 mm thickness, avoiding sulfate electrolytes, the normal volume is 72.35 cm^3, determined by gas expansion from the calorimeter in the cryostat. The 100-ohm, constantan wire heater is varnished directly onto the sphere, and shielded by the lightweight calorimeter case, which serves also as the wire spool for thermally anchoring thermocouple and thermometer leadwires. The 1/16-in. o.d. stainless steel capillary has a bore diameter of 0.0345 cm. This relatively large bore is essential for rapid filling and emptying of the calorimeter. Volume of this capillary, including a valve at the head of the cryostat, is 0.080 cm^3.

Adiabatic shielding is in two parts: the guard ring, and attached, lightweight shield can. The ring tempers all electric wires, pressed into individual, longitudinally machined grooves. These wires lead from similar grooves in the cold ring and lead to the calorimeter case. Separate heaters are wound on the guard ring, the cylindrical surface of the shield and as a plane spiral on the bottom of the shield can. The two shield heaters operate in a divider circuit from a single regulator. These heaters are automatically controlled from thermopile *1* and thermocouple *2* respectively of figure 6. Thermocouple *3* serves for manual adjustment of the side-to-bottom heat divider. Thermocouple *4* serves for automatic temperature control of shields and calorimeter, during gas-expansion calibrations of the calorimeter volume, with reference to the refrigerant tank temperature.

To facilitate control of the calorimeter temperature during some calibrations, a small heat leak is introduced to the present apparatus. Thermal contact between electric wires and tempering ring is reduced to obtain the calorimeter cooling drift described in section 13.4 The calorimetric method therefore may be described as quasi-isothermal.

13.3. Control and Measurement of Heat

The control circuits for calorimetric heating are indicated by figure 8. Although they are conventional in principle, a useful simplification is application of an electronic battery: a 0.5 amp, transistorized, d-c power supply, continuously adjustable to 0.02 v from 0 to 32 v, with regulation and stability better than 0.002 v. The rms ripple is 0.001 v. The battery source impedance, R_b of the figure, is readily adjusted equal to the calorimeter heater resistance when the battery potential indicated by P–1 is twice the heater potential indicated by P–2 [31]. To provide time for potentiometric measurements of the heater power, and for shield temperature adjustments, a temperature rise of about 2° in a fixed interval of 10 min at all temperatures is realized by adjusting the battery potential. This adjustment does not affect R_b, in contrast to behavior with conventional batteries and rheostats. Relay coils are operated with direct current to reduce induction of spurious a-c effects in the low-level circuits.

Potentials are measured with the 6-dial microvolt potentiometer and with a type K–3 universal potentiometer, each indicating through an electronic galvanometer [56], as in figure 5. Potentials to be measured are connected to each potentiometer by high-quality, commercial, microvolt selector switches. Four measurements of heater potential and current are made in 10 min. Heater power is constant to better than 1 part in 10,000. The standard electric, clutch-type, synchronous stopclock utilizes local, 60 c/s, powerline frequency for the time standard. The NBS Time Standards Section finds that this frequency usually is accurate and constant to well within 0.03 percent.

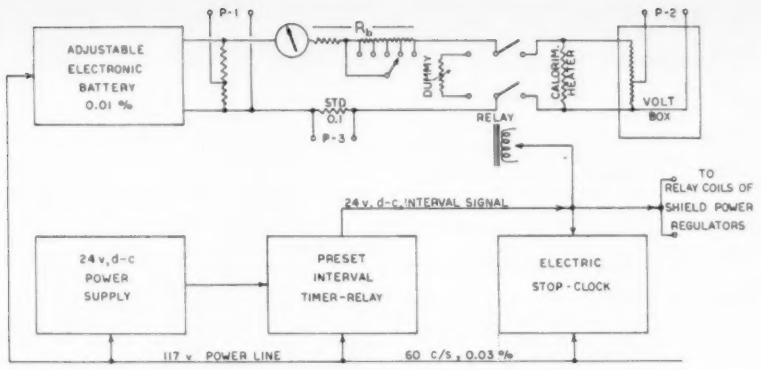

FIGURE 8. *Calorimetric heat control methods.*

13.4. Measurement of Temperatures

The calorimeter platinum resistance thermometer is calibrated and the thermometric technique checked as described for PVT determinations. Imperfections of adiabatic shielding yield empty calorimeter drift rates from −0.0009°/min at 20 °K to −0.0019°/min at 100 °K. These are linear in time.

Five temperature observations in 5 min precede a heating interval. Nonlinear equilibration following the interval requires a few minutes, and is observed with a recorder. Five similar temperature measurements follow. Temperature-time behaviors are extrapolated to mean time of the heating interval, by a least-squares computer program, at which time is taken the calorimetric temperature increment.

13.5. Control of Shield Temperatures

The different methods, isothermal and adiabatic shielding, are useful for different purposes [37]. The adiabatic method is selected here for rapid adjustments in the range 20 to 100 °K where thermal transport is almost entirely conductive. Gold-cobalt versus copper thermocouples indicate temperature differences between the calorimeter and the guard ring and shield respectively. An individual regulating system is employed for each of the latter. An improvement of present instrumentation, indicated by the bottom row of figure 5, is its simplicity relative to current practices [27]. Control instruments are the microvolt amplifier [56] and the power regulator [50]. Two factors contribute to satisfactory operation. (1) Thermocouples are so placed on shields as to give rapid but average response. The heater windings and powers are designed to match the areas and masses of metal to be controlled. (2) The power regulator contains a solenoid relay, operated by the heating interval signal, figure 8, which automatically boosts the shield heating to a manually pre-set level. This eliminates the delay otherwise required for development of the temperature difference normally utilized for automatic control. The booster circuit does not affect the low output impedance of this regulator, thereby avoiding the loss of power-gain and temperature-regulation otherwise suffered when resistances or other impedances are inserted in the heater circuit for boosting control. Because automatic resetting instruments are not necessary for the present work, the normal steady-state heating also is manually adjusted at the power regulator. For calibration work, the shield versus calorimeter temperature differences may be recorded from the microvolt amplifier output signals by means of simplified strip-chart instruments. A typical chart shows that, with routine error in adjustment of the boost heat level, the guard ring-versus-calorimeter temperature difference peaks at 0.001 °C at the start of an interval and decays to within 0.0001° in 20 sec. The same behavior with opposite sign follows the ending of an interval. Relative change in the steady heat-leak over the copper wire bundle between guard ring and calorimeter is negligible during a heating interval.

The numerous machined parts for the cryostats were made in the NBS, Boulder shop under S. Landis. The skillful assembly and silver-soldering of these parts as well as the construction of the liquid transfer and hard vacuum systems by Cryogenic Division instrumentalist W. R. Bjorklund greatly advanced the project. D. E. Diller placed all of the small electric wiring in the cryostats, intercalibrated the gasometer glass volumes, performed the gas-expansion calibrations of the pipet, checked fixed-points of the platinum thermometer, and measured null-point shift of the diaphragm cell in addition to other important contributions. L. A. Weber assisted with the many details of placing the PVT apparatus in final operating condition. B. A. Younglove determined mechanical properties of the calorimeter and with D. E. Diller placed the calorimetry in successful operation. Hans M. Roder, in programing the computer work, devised subsidiary equations presented in sections 5.3 and 10. Continuing encouragement from Robert J. Corruccini and Russell B. Scott have been essential in bringing this long task to completion.

14. References

14.1. General

[1] Stanley H. Bransom, Applied thermodynamics (D. van Nostrand Co., Ltd., London, 1961).

[2] F. Din, editor, Thermodynamic functions of gases, 1 (Butterworths Scientific Publications, London, 1956).

[3] B. F. Dodge, Chemical engineering thermodynamics (McGraw-Hill Book Co., Inc., New York, N.Y., 1944).

[4] W. E. Forsythe, Smithsonian physical tables, Ninth revised ed. (Smithsonian Institution, Washington, D.C., 1956).

[5] Lawrence Lessing, The master fuel of a new age, Fortune **63** (5), 152 (1961).

[6] A. Michels, High pressure research, Research **9,** 99 (1956).

[7] A. Michels, J. C. Abels, C. A. Ten Seldam, and W. deGraff, Polynomial representation of experimental data; application to virial coefficients of gases, Physica **26,** 381 (1960).

[8] J. B. Opfell and B. H. Sage, Application of least-squares methods, Ind. Eng. Chem. **50,** 803 (1958).

[9] J. S. Rowlinson, The properties of real gases, Handbuch der Physik, vol. **XII,** S. Fluegge, ed. (Springer-Verlag, Berlin 1958).

[10] R. B. Scott, Liquid hydrogen for chemical and nuclear rockets, Discovery **21** (2), 74 (1960).

14.2. Cryogenic Technique

[11] J. G. Aston and H. L. Fink, Application of low temperatures to chemical research, Chem. Revs. **39,** 357 (1946).

[12] F. Din and A. H. Cockett, Low temperature techniques (Geo. Newness, Ltd., London, 1960).

[13] R. B. Scott, Cryogenic engineering, D. van Nostrand, Co., Ltd., London (1959).

[14] G. K. White, Experimental techniques in low-temperature physics (Clarendon Press, 1959).

14.3. PVT Methods

[15] E. P. Bartlett, H. C. Hetherington, H. M. Kvalnes, and T. H. Tremearne, The compressibility isotherms of hydrogen, nitrogen and a 3:1 mixture of these gases at temperatures of −70, −50, −25 and 20° at pressures up to 1000 atmospheres, J. Am. Chem. Soc. **52,** 1363 (1930).

[16] J. A. Beattie, The apparatus and method used for the measurement of the compressibility of several gases in the range 0° to 325°C. Proc. Am. Acad. Arts. Sci. **69,** 389 (1934).

[17] E. S. Burnett, Compressibility determinations without volume measurements, J. Appl Mechanics **3,** 136 (1936).

[18] D. Cook, The second virial coefficient of carbon dioxide at low temperatures, Can. J. Chem. **35,** 268 (1957).

[19] A. S. Friedman, Pressure-volume-temperature relationships of gaseous hydrogen, nitrogen and a hydrogen-nitrogen mixture, Thesis, The Ohio State University, (1950).

[20] L. Holborn and H. Schultze, On the pressure balance and the isotherms of air, argon and helium between 0 and 200°, Ann. der Physik **47,** 1089 (1915).

[21] L. Holborn and J. Otto, On the isotherms of helium, nitrogen and argon below 0°, Z. Physik **30,** 320 (1926).

[22] L. Holborn and J. Otto, The isotherms of helium, hydrogen and neon below −200°, Z. Physik **38,** 359 (1926).

[23] H. L. Johnston, W. F. Keller, and A. S. Friedman, The compressibility of liquid normal hydrogen from the boiling point to the critical point at pressures up to 100 atm., J. Am. Chem. Soc. **76,** 1482 (1954).

[24] H. L. Johnston and D. White, Pressure-volume-temperature relationships of gaseous normal hydrogen from its boiling point to room temperature and from 0–200 atmospheres, Trans. ASME **72** (6), 785 (1950).

[25] A. Michels, T. Wassenaar, and Th. N. Zwietering, The experimental determination of the equation of state of gases at temperatures between 0° and −180° C, Physica **18,** 67 (1952).

14.4. Calorimetric Methods

[26] J. G. Aston and M. L. Eidinoff, The low temperature precision adiabatic calorimeter adapted to condensed gases from 10 °K. to room temperature, J. Am. Chem. Soc. **61,** 1533 (1939).

[27] W. J. Cooper, R. H. Forsythe, J. F. Masi, and R. E. Pabst, Low temperature adiabatic calorimeter with automatic shield control, Rev. Sci. Instr. **30,** 557 (1959).

[28] A. Eucken, On the thermal behavior of some compressed and condensed gases at low temperatures, Verh. deut. Phys. Ges. **18,** 4 (1916).

[29] R. W. Hill, Low-temperature calorimetry, Progress in Cryogenics, vol. **1,** K. Mendelssohn, ed. (Heywood and Co., Ltd., London, 1959).

[30] H. J. Hoge, Heat capacity of a two-phase system, with applications to vapor corrections in calorimetry, J. Research NBS **36,** 111 (1946) RP1693.

[31] H. J. Hoge, Circuits for minimizing transient effects on energy measurements in calorimetry, Rev. Sci. Instr. **20,** 59 (1949).

[32] Hugh M. Huffman, Low-temperature calorimetry, Chem. Revs. **40,** 1 (1947).

[33] O. V. Lounasmaa, Specific heats at low temperatures, Thesis, University of Oxford, Brasenose College, 1958. (Helium C_v and PVT.)

[34] A. Michels and J. C. Strijland, The specific heat at constant volume of compressed carbon dioxide, Physica **18,** 613 (1952).

[35] E. B. Rifkin, E. C. Kerr, and H. L. Johnston, Condensed gas calorimetry. IV. The heat capacity and vapor pressure of saturated liquid diborane above the boiling point, J. Am. Chem. Soc. **75,** 785 (1953).

[36] P. A. Walker, The equation of state and the specific heat of liquid argon, Thesis, Queen Mary College, Univ. of London (1956).

[37] D. M. Yost, C. S. Garner, D. W. Osborne, T. R. Rubin, and H. Russell, Jr., A low temperature adiabatic calorimeter. The calibration of platinum resistance thermometers, J. Am. Chem. Soc. **63,** 3488 (1941).

14.5. Thermometry

[38] Anonymous, Symposium on Temperature, Its Measurement and Control in Science and Industry (Columbus, Ohio, March 27, 1961), Abstracts, 116 pp., $5.00, American Institute of Physics, 335 E. 45th St., New York, N.Y.

[39] T. M. Dauphinee and H. Preston-Thomas, A copper resistance temperature scale, Rev. Sci. Instr. **25,** 884 (1954).

[40] N. Fuschillo, A low-temperature scale from 4 to 300 °K in terms of a gold-cobalt vs. copper thermocouple, J. Phys. Chem. **61,** 664 (1957).

[41] F. K. Harris, Electrical Measurements (John Wiley & Sons, Inc., New York, N.Y., 1952).

[42] H. J. Hoge and F. G. Brickwedde, Establishment of a temperature scale for the calibration of thermometers between 14° and 83 °K, J. Research NBS **22,** 351 (1939) RP1188.

[43] E. F. Mueller and H. F. Stimson, A temperature-control box for saturated standard cells, J. Research NBS **13,** 699 (1934) RP739.

[44] R. L. Powell, M. D. Bunch, and R. J. Corruccini, Low-temperature thermocouples—I. Gold-cobalt or constantan versus copper or "normal" silver, Cryogenics **1** (3), 139 (1961).

[45] Bruce K. Smith, Low thermal soldering procedures for copper junctions, Electronic Design **7** (25), 52 (1959).

[46] H. F. Stimson, Precision resistance thermometry and fixed points, Temperature, vol. **2,** H. C. Wolfe, editor (Reinhold Publ. Corp., New York, N.Y., 1955).

[47] H. F. Stimson, Heat units and temperature scales for calorimetry, Am. J. Phys. **23,** 614 (1955).

14.6. Instruments

[48] W. G. Brombacher, D. P. Johnson, and J. L. Cross, Mercury barometers and manometers, NBS Mono. 8 (1960).

[49] D. O. Coffin, High-pressure gas-to-liquid transducer, Rev. Sci. Instr. **29,** 896 (1958).
[50] R. D. Goodwin, An improved d.c. power regulator, Advances in cryogenic engineering, vol. **5,** K. D. Timmerhaus, ed. (Plenum Press, New York, N.Y., 1960).
[51] P. C. Hoell, Low-level d.c. amplifier with whole-loop feedback, Rev. Sci. Instr. **29,** 1120 (1958).
[52] D. P. Johnson and D. H. Newhall, The piston gauge as a precise pressure-measuring instrument, Trans. ASME **75,** 301 (April 1953).
[53] F. G. Keyes, High-pressure technic, Ind. Eng. Chem. **23,** 1375 (1931).
[54] T. W. Lashof and L. B. Macurdy, Precision laboratory standards of mass and laboratory weights, NBS Circ. 547 (1954).
[55] L. LeBlan, The precise measurement of pressures, Chimie et ind. **61,** 235; 349 (1949).
[56] M. D. Liston, C. E. Quinn, W. E. Sargeant, and G. G. Scott, A contact-modulated amplifier to replace sensitive suspension galvanometers, Rev. Sci. Instr. **17,** 194 (1946).
[57] A. Michels, Calibration of pressure-balance in absolute units, Proc. Kon. Ak. Amsterdam **35,** 994 (1932).
[58] J. R. Purcell and R. N. Keeler, Sensitive thermal conductivity gas analyzer, Rev. Sci. Instr. **31,** 304 (1960).
[59] H. H. Reamer and B. H. Sage, Experience with piston-cylinder balance for pressure measurements, Rev. Sci. Instr. **26,** 592 (1955).
[60] E. E. Watson, Constant current supply for the potentiometer, Am. J. Phys. **27,** 404 (1959).
[61] D. White and J. Hilsenrath, A pressure-sensitive diaphragm-type null detector, Rev. Sci. Instr. **29,** 648 (1958).

14.7. Fluids Properties

[62] G. T. Armstrong, Vapor pressure of nitrogen, J. Research NBS **53,** 263 (1954) RP2543.
[63] J. J. M. Beenakker, F. H. Varekamp, and H. F. P. Knapp, The second virial coefficient of ortho and para hydrogen at liquid hydrogen temperatures, Physica **26,** 43 (1960).
[64] A. S. Friedman and J. Hilsenrath, The thermodynamic and transport properties of liquid hydrogen and its isotopes (private communication).
[65] Joseph Hilsenrath et al., Tables of thermal properties of gases, NBS Circ. 564 (1955).
[66] H. J. Hoge and R. D. Arnold, Vapor pressures of hydrogen, deuterium, and hydrogen deuteride and dew-point pressures of their mixtures, J. Research NBS **47,** 63 (1951) RP2228.
[67] V. J. Johnson, editor, A compendium of the properties of materials at low temperature. Part I, Properties of fluids. Part II, Properties of solids, WADD Technical Report 60–56, Office of Technical Services, U.S. Dept. Commerce, Washington 25, D.C.
[68] R. B. Stewart and V. J. Johnson, A compilation and correlation of the P-V-T data of normal hydrogen from saturated liquid to 80 °K, Advances in Cryogenic Engineering, vol. **5,** K. D. Timmerhaus, ed. (Plenum Press, New York, N.Y., 1960).
[69] H. W. Woolley, R. B. Scott, and F. G. Brickwedde, Compilation of thermal properties of hydrogen in its various isotopic and ortho-para modifications, J. Research NBS **41,** 379 (1948) RP1932.

14.8. Solids Properties

[70] J. H. Faupel and A. R. Furbeck, Influence of residual stress on behavior of thick-walled closed-end cylinders, Trans. ASME **75,** 345 (April 1953).
[71] M. J. Hiza, Cryogenic impurity adsorption from hydrogen, Chem. Eng. Progr. **56** (10), 68 (1960).
[72] R. N. Keeler and K. D. Timmerhaus, Poisoning and reactivation of ortho-parahydrogen conversion catalyst, Advances in Cryogenic Engineering, vol. **4,** K. D. Timmerhaus, ed. (Plenum Press, New York, N.Y., 1960).
[73] R. M. McClintock, D. A. vanGundy, and R. H. Kropschot, Low-temperature tensile properties of copper and four bronzes, ASTM Bull. No. 240, p. 47 (TP 177) (Sept. 1959).
[74] A. Michels, The behavior of thick-walled cylinders under high pressures, Proc. Kon. Ak. Amsterdam **31,** 552 (1928).
[75] R. L. Mills and F. J. Edeskuty, Hydrogen embrittlement of cold-worked metals, Chem. Eng. Prog. **52** (11), 477 (1956).
[76] G. W. Morey, The properties of glass (Reinhold Publ. Corp., New York, N.Y., 1954).
[77] R. L. Powell and W. A. Blanpied, Thermal conductivity of metals and alloys at low temperatures, NBS Circ. 556 (Sept. 1, 1954).
[78] T. Rubin, H. W. Altman and H. L. Johnston, Coefficients of thermal expansion of solids at low temperatures, J. Am. Chem. Soc. **76,** 5289 (1954).
[79] S. Timoshenko, Strength of materials II, 2d ed., eq. (208) (D. van Nostrand Co., Inc., New York, N.Y., 1941).

(Paper 65C4–76)

JOURNAL OF RESEARCH of the National Bureau of Standards—C. Engineering and Instrumentation
Vol. 65C, No. 4, October–December 1961

The Use of a Thermistor for Detecting Eluent Fronts in Liquid-Solid Chromatography

Gaylon S. Ross

(July 24, 1961)

The adsorption-desorption phenomenon which occurs when a multicomponent liquid is forced through a column of solid adsorbent is accompanied by an evolution of heat. The resulting temperature change occurring within the column may be monitored and correlated with the compositional changes occurring in the liquid phase. The construction and use of thermistor sensing cells is described. These cells are an integral part of the column, and they are maintained at appropriate temperatures by either constant temperature, liquid-circulating baths or by transistorized temperature controllers. Both methods of temperature control are described, and various applications of the cells are discussed.

1. Introduction

As part of a study of liquid-solid chromatography, it was desirable to develop means which would allow the process to be observed at various positions down the column length. The adsorption of a liquid upon the solid adsorbent causes an evolution of heat, and the displacement of this adsorbed liquid by a more tenaciously adsorbed liquid produces a further evolution of heat. The heats of preferential sorption upon a wide variety of solid sorbents have been determined using a calorimeter of simple design.[1] An application of this principle to observe the heat from the adsorption-desorption process as it takes place in the chromatographic column is described herein.

A small thermistor, embedded in the column packing, is used to detect the temperature changes produced by the adsorption-desorption process. Since the magnitude of this temperature change may vary from, at most, a few degrees to as little as a tenth of a degree, the portion of the column containing the thermistor must be kept at nearly constant temperature if good sensitivity is desired. This is achieved by a constant temperature, circulating bath or by electrical resistance heating with a suitable controller. The thermistor, the brass block which houses and supports the thermistor, and the necessary heating jackets are referred to herein as the "cell". These cells provide an in situ analytical tool for sensing and recording the changes in column temperature which result from the heat generated by adsorption. The inner diameter of the cell is made the same as the inner diameter of the column; the packing is continuous through both the cells and the column; and there are no large obstructions to the liquid flow. The cells, described in detail later, are connected to the glass column by means of a kovar-glass seal. As many cells as are desired may be placed at predetermined positions down the column length, and the column behavior may be monitored without loss of material and without disturbing the column continuity. Not only can the progress of the separation, as it occurs on the column, be observed, but the collection of fractions can be accomplished automatically, and qualitative estimates of the differential heats of adsorption can be obtained.

2. Apparatus

Several different types of cells have been constructed. While they differ, depending on their intended use, they are similar to the one shown in figure 1. This cell is made in two sections, which are electrically insulated from each other by means of a Teflon gasket. A glass-coated bead thermistor (2,000 ohms at 20 °C) is centered between the two sections, as shown (D). It has been found that the 2,000-ohm thermistors give adequate response when used as one arm of a balanced-arm Wheatstone bridge. The platinum-iridium leads of the thermistor electrically bridge the two brass cell members. These sections are held together by spring-loading, which maintains a liquid-tight seal despite temperature changes. The column is packed with solid adsorbent so that it is continuous throughout the total length of the column, including the cell sections. The inner diameter is the same as that of the column so that the chromatographic separation may be recorded without disturbing the advancing liquid fronts. Figure 2 is a schematic representation of a typical column showing two different types of cells in a single column. The upper cell is the same as that shown in figure 1. In the upper cell, figure 2, water maintained at a constant temperature by an auxiliary water bath is circulated through a water jacket. For the lower cell, which is of one-piece design, an electrically-heated copper block is substituted for the water

[1] A. Groszek, J. Chromatog. 3, 454, (1960).

604529—61——3

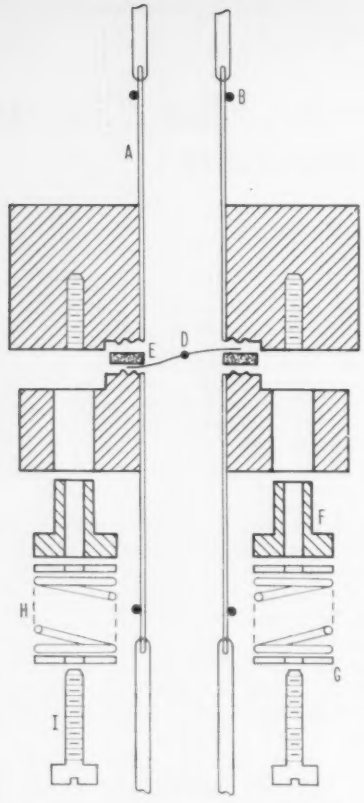

FIGURE 1. *Temperature sensing cell.*

A. Kovar to Pyrex graded seal
B. Wire soldered to kovar, used as electrical contact
C. Brass-cell body
D. Thermistor bead in place in packed column (bead, 0.01-in. diam)
E. Teflon gasket
F. Kel-F insulator
G. Brass washer
H. Spring
I. Screws holding cell halves together

jacket. The block is maintained at constant temperature by the transistorized proportionating controller[2] shown in figure 3.

3. Experimental Procedure

An example of the chromatogram obtained with this apparatus is given in figure 4. The test mixture contained equal volumes of *n*-heptane, carbon tetrachloride, and benzene. The mixture was chosen to illustrate different degrees of compound separation. Ten milliliters of this mixture were poured onto the top of a silica gel (28–200 mesh) packed column. The column was 6 ft long and ⅜ in. in diam. The cell was maintained at 30 °C. Ethyl alcohol was used to elute the test mixture.

[2] The author is indebted to Malcolm Morse of the Instrumentation Division for designing this low-cost controller and for the privilege of including it in this paper. The instrument provides control of ±0.02 °C for several hours at an operating temperature of 60 °C.

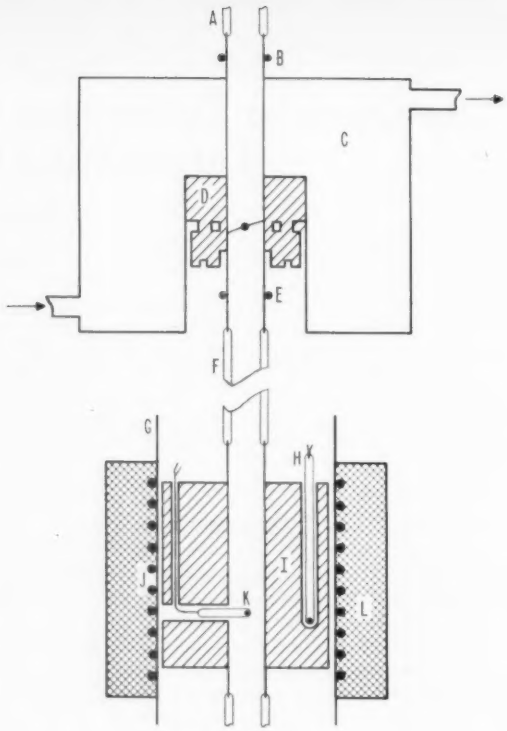

FIGURE 2. *Typical packed column.*

Two cells are shown. The top one is a two-piece cell being thermostated by a constant-temperature circulating liquid. The lower cell is a one-piece cell being thermostated by an electrically heated jacket which is maintained at constant temperature.

A. Kovar to Pyrex graded seal
B. Wire serving as electrical contact
C. Jacket containing thermostating liquid
D. Cell as shown in fig. 1
E. Electrical contact
F. Kovar to Pyrex graded seals
G. Brass tubing
H. Control thermistor
I. One-piece brass cell
J. Electrical heating wire
K. Sensing thermistor (glass rod, 0.08-in. diam, ½-in. length)
L. Glass insulation.

The cell was placed at the exit end of the column so that the refractive indices of the eluent could be compared directly with the recorded temperature variations. However, it could have been placed in any position down the length of the column, or several cells could have been used in series so as to follow the separation process. When a signal attenuation of 30 times was used, the record shown in figure 4 was obtained by using a 10-mv, potentiometric strip-chart recorder. The refractive index curve (dotted) was obtained by measuring successive 0.5-ml portions of the sample as it emerged from the bottom of the cell. Accumulative error in measuring the volume of these cuts is probably responsible for the phase shift between the two curves.

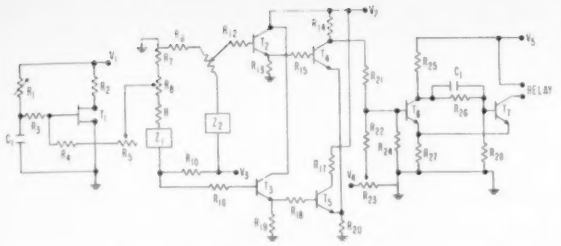

FIGURE 3. *Wiring diagram for transistorized proportionating controller.*

Resistance (R_i), ½ watt unless otherwise specified

1	10 K	15	100 ohm
2	470 ohm	16	470 ohm
3	10 ohm, 1 watt	17	1 K
4	1 K	18	100 ohm
5	10 K	19	1 K
6	800 ohm	20	510 ohm
7	100 ohm	21	5 K
8	50 ohm	22	5 K
9	100 ohm	23	1 K
10	1050 ohm	24	2.4 K
11	500 ohm	25	3.5 K
12	470 ohm	26	51 K
13	1 K	27	2.5 K
14	1 K	28	51 K

Capacitors (C_i)

1	2,000 mfd	2	10,000 mfd

Transistors (T_i)

1	2N489, 2N490, 2N491, 2N492	4	2N377
		5	2N377
2	2N377	6	2N377
3	2N377	7	2N377

Voltage sources (batteries B_i)

1	+22½ v	4	+6 v
2	+9 v	5	+9 v
3	+6 v		

Thermistors (Z_i)

1, 2 800-ohm thermistors at operating temperature.

Relay

Sigma, 7AOY 3,500 SD–SIL. 3,500-ohm dual coils, polarized.

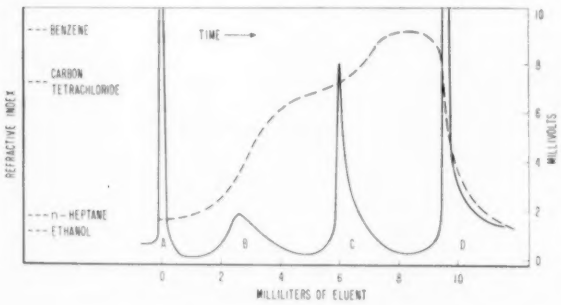

FIGURE 4. *Recorded chromatograph.*

Refractive index plot is shown as dashed curve. Refractive indices of the pure components are shown at left of figure. "A" is the peak due to the heat of adsorption of *n*-heptane; "B" the peak due to carbon tetrachloride, "C" that due to benzene and "D" that due to ethanol.

4. Discussion

This cell has been used with several different test mixtures. In all cases distinct peaks were obtained when the refractive indices showed that a separation of the components had taken place in the column. In general, a broad peak is indicative of incomplete separation, and the amount of tailing appears to be inversely proportional to the degree of separation.

The height and broadness of the peaks are influenced by many factors such as degree of resolution, flow rate, thermal conductivity, thermal diffusion, cell temperature, etc. Under constant column head-pressure, the flow rate is nearly constant, and the height and area under the peaks give valuable information concerning the relative differential heats of adsorption and quantity of material.

The cell may be used to actuate an automatic fraction collector. This can be done by using an adjustable limit-switch on the recorder to rotate the fraction collecting table when a new peak appears. For those materials which do not separate sharply, the heading and tailing of the peaks may be used to actuate the fraction collector. In this case, the rate of peak decay or buildup could be used as the controlling signal. This method would have the advantage afforded by the taking of fraction as a function of changing purity, but a combination of the first method together with the usual volume or time-actuated mechanism of the fraction collector would achieve nearly the same result with much simpler control.

When either the sample or the adsorbent is electrically conducting, the cell consisting of the single block should be used. The thermistors used in this cell are of the glass-enclosed probe type and are inserted through the side of the cell. The probe can be sealed in the block with the usual stuffing box arrangement or by making a liquid-tight seal with epoxy resin or soft solder. Such a thermistor has a much higher heat capacity than the bead type and the recorded peaks tend to be less high. The larger size of this probe does not seem to disrupt the flow pattern of the liquid. The problem of increased heat capacity can be minimized by using a low-gain d-c amplifier prior to recording the signal or by using thermistors of higher resistance.

The use of cells of this and similar types in conjunction with other analytical tools should make a systematic study of liquid-solid chromatographic separation more feasible.

The author is indebted to Miss Nancy Beach for her assistance in the performance of early experiments and to Herbert B. Lowey for his assistance in the design and fabrication of the cells.

(Paper 65C4—77)

JOURNAL OF RESEARCH of the National Bureau of Standards—C. Engineering and Instrumentation
Vol. 65C, No. 4, October-December 1961

Radiation Field From a Circular Disk Source[1]

J. H. Hubbell, R. L. Bach, and R. J. Herbold

(February 4, 1961)

A number of radiation shielding problems involve calculations of the response of an isotropic detector to radiation of arbitrary angular distribution from uniform finite plane sources. Series expansion methods previously used for treating the rectangular source are here extended to include the circular disk source with detector off-axis. These methods involve the family of integrals $\int_S (\cos\theta\, dS/r^2) P_l(\cos\theta)$ and the integral $\int_S (dS/r^2) \exp(-\mu r)$ where θ is obliquity with respect to the normal to the disk surface S, r is the distance from an element of source area, dS, to the detector, and μ is the attenuation coefficient. Tabulations of the first type of integral facilitate use of Legendre expansion representations of radiation directional distributions. The second integral relates primarily to exponentially attenuated radiation from a plane isotropic disk source, but the expansion coefficient solution can be readily adapted to take into account a point isotropic buildup factor of the polynomial form $\sum_{i=0}^{N} \beta_i(\mu r)^i$. This adaptation applies equally well to the corresponding expansion coefficients previously given for the rectangular source. Formulas and numerical results are presented.

1. Introduction

In radiation shielding, photometry and related studies, a frequently occurring problem is that of calculating the radiation field resulting from a finite plane source of radiation with arbitrary polar angular distribution $g(\theta)$. A number of authors have investigated the response of surface-type [1][2] detectors to rectangular and circular Lambert's-law radiators. Smith and Storm [2] have derived a generalized series expansion method for calculating the response of an azimuthally symmetric detector off-axis from a disk source with arbitrary surface angular distribution, in which evaluation of the series terms involves successive differentiation of the detector response to a differential element of the source area. The resulting formulas usually consist of triple or quadruple summations in which one sum can be obtained by recursion methods.

In a previous paper [3], a Legendre expansion method suggested by Berger and Lamkin [4] was applied to a rectangular source as part of a general study of the penetration of radiation into structures [5]. In the Berger-Lamkin method, the *geometric* relationship of detector to source is characterized by a set of Legendre coefficients, p_l, over which corresponding *penetration*-dependent coefficients, g_l, of a Legendre expansion of $g(\theta)$ may be summed. This has some advantage over the results in reference [2] in that not only are the geometrical and penetration parameters separated for economy of data tabulation, but use of the present Spencer-Fano [6] moments method provides most directly the g_l coefficients, rather than the actual angular distributions $g(\theta)$.

For small values of μt, where μ is the attenuation coefficient and t is the barrier thickness, the Legendre series solution does not converge adequately for the particular angular distribution for the unscattered radiation from a plane isotropic source [3]

$$g(\theta) = g^o(\theta) \equiv (\sigma/4\pi) \exp(-\mu t/\cos\theta)/\cos\theta, \quad (1)$$

in which $\sigma/4\pi$ is the source strength in units of radiation (e.g., photons) emitted per unit time from unit surface area into unit solid angle. The reason for this poor convergence is that, as $\mu t \to 0$, $g^o(\theta) \to (\sigma/4\pi)/\cos\theta$, and a function of the form $1/\cos\theta$ is not representable by the *positive* powers of $\cos\theta$ appearing in the Legendre polynomials. An alternative series expansion in powers of μt with geometry dependent coefficients, q_n, was provided for calculating the unscattered radiation component when $0 \leq \mu t \lesssim 1$.

The present work extends the two expansion methods in reference [3] to include the case of a circular disk source with detector off-axis. A typical example of this situation would be the estimation of the neutron flux around the face of a cylindrical thermal column of a research reactor [7]. In addition, it will be shown that if the scattering properties of the medium are given as a point isotropic buildup factor [6] in polynomial form [8, 9]

$$B(\mu r) \cong \sum_{i=0}^{N} \beta_i (\mu r)^i, \quad (2)$$

rather than as angular harmonics, g_l, at the exit surface of the barrier, the q_n expansion coefficients here and in reference [3] can often be used to evaluate the scattered as well as unscattered contribution to the radiation flux.

[1] Work supported jointly by the Office of Civil and Defense Mobilization the Navy Bureau of Yards and Docks, and the Defense Atomic Support Agency
[2] Figures in brackets indicate the literature references at the end of this paper.

[3] Here and in what follows, g^o and I^o will be used to denote the angular distribution and intensity of direct radiation, i.e., radiation which arrives at the detector from the source after having undergone no scattering interactions with the intervening medium.

2. Arbitrary Angular Distribution; Legendre Expansion of the Angular Response Function

2.1. Isotropic Detector (Flux)

If the emission from each source element, dS, of the disk, is independent of azimuth and uniform over the source surface S, the radiation intensity at any point in space, as measured by a small spherically symmetric detector, may be written as the integral

$$I=\int g(\theta)\cdot\psi_S(\theta)d(\cos\theta). \tag{3}$$

Here θ is the polar angle as indicated in figure 1. The angular distribution function $g(\theta)$ of radiation crossing the source-plane will now be defined as the radiation flux [4] (e.g., photons) traveling in direction θ per unit solid angle, unit time, and unit area normal to direction θ. $\psi_S(\theta)$, called the "angular response function" in reference [4], is the azimuthal angle subtended by the source area from the detector-to-source-plane vertical for a given θ-cone around this vertical.

There are a variety of ways in which the integral (3) may be evaluated, depending on the nature of $g(\theta)$ and S. The Legendre expansion method, especially advantageous if g_l coefficients happen to be already available, has been discussed in detail in references [3] and [4], but for convenience a brief summary is given as follows:

The two functions, $g(\theta)$ and $\psi_S(\theta)$, in (3) which are parametrically independent except in θ, may (if free of singularities) be expanded in Legendre harmonics as

$$g(\theta)=\sum_{l=0}^{\infty}(l+\tfrac{1}{2})g_l\cdot P_l(\cos\theta) \tag{4}$$

and

$$\psi_S(\theta)=\sum_{l=0}^{\infty}(l+\tfrac{1}{2})p_l\cdot P_l(\cos\theta). \tag{5}$$

[4] In this notation the radiation flux in direction θ per unit solid angle, unit time and *unit area of the source* would be $g(\theta)\cos\theta$, i.e., $g(\theta)$ may be identified with the angular distribution functions $g(z,\theta)$ and $\phi(\mu)$ of references [4] and [7], respectively, but differs from $G(R)$ of reference [2] according to $g(\theta)=G(R)/\cos\theta$.

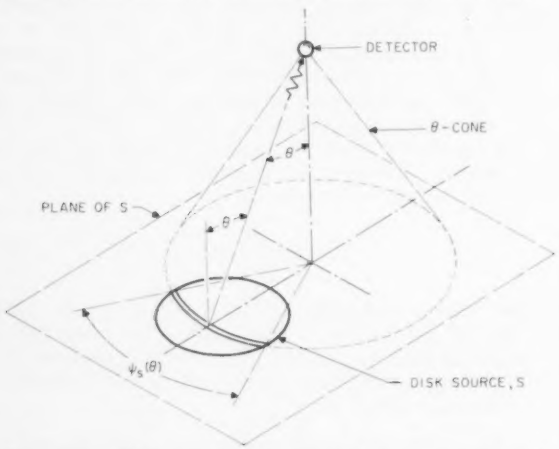

FIGURE 1. *Disk source and off-axis detector, showing polar angle θ and "angular response function," $\psi_S(\theta)$.*

When this is done, the integral (3) may be written as the series

$$I=\sum_{l=0}^{\infty}(l+\tfrac{1}{2})g_l\cdot p_l \tag{6}$$

which converges rapidly for many cases of interest.

The p_l coefficients may be evaluated in the usual way according to

$$p_l=\int_S P_l(\cos\theta)\cdot\psi_S(\theta)d(\cos\theta), \tag{7}$$

or since $\psi_S(\theta)d(\cos\theta)$ is a differential solid angle $d\Omega_S(\theta)$,

$$p_l=\int_S P_l(\cos\theta)d\Omega_S(\theta) \tag{8}$$

As in reference [3], the $\psi_S(\theta)$ and related p_l's are dependent on the relative, rather than on the absolute dimensions, so that we may select one dimension, here the disk radius, as the unit of length. The quantities ρ and h, as indicated in figure 2, are then the distances off axis and off disk-plane, respectively, measured in disk radii.

Since the polynomials $P_l(\cos\theta)$ are linear combinations of even or odd powers of $(\cos\theta)$ it is convenient to break up (8) into components $F_j(\rho,h)$, each over a particular power of $\cos\theta$, i.e.

$$F_j(\rho,h)=\int_S \cos^j\theta d\Omega(\theta,\rho,h), \tag{9}$$

from which we reconstruct the desired functions $p_l(\rho,h)$ according to

$$p_l(\rho,h)=\sum a_{lj}F_j(\rho,h), \tag{10}$$

where a_{lj} are the coefficients of x^j in the Legendre polynomial

$$P_l(x)=\sum a_{lj}x^j$$

of order l.

The differential solid angle, $d\Omega(\theta,\rho,h)$, can be written in cylindrical coordinates h, R, and ϕ around

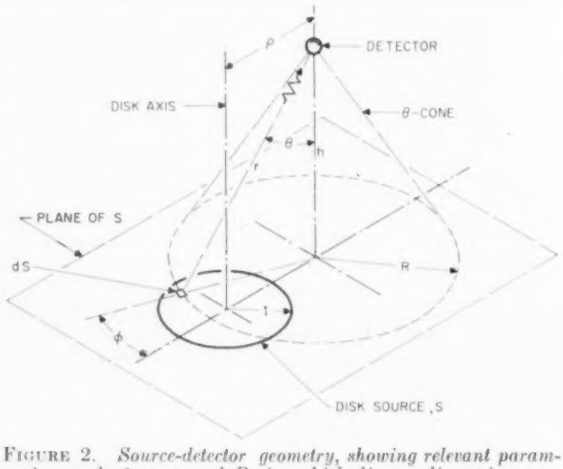

FIGURE 2. *Source-detector geometry, showing relevant parameters ρ, h, θ, ϕ, r and R, in which linear dimensions are measured in radii of the source disk.*

the perpendicular from detector to source-plane as

$$d\Omega(\theta,\rho,h)=\cos\theta\, dS/r^2=(h^2+R^2)^{-3/2}hR\, dR\, d\phi, \quad (11)$$

since $\cos\theta=h/\sqrt{h^2+R^2}$, $dS=R\, dR\, d\phi$, and $r^2=h^2+R^2$. The integral in (9) may now be written explicitly as the double integral [5]

$$F_j(\rho,h) = h^{j+1}\int_{R=\rho-1}^{\rho+1}\int_{\phi=-1/2\psi(\theta,\rho,h)}^{1/2\psi(\theta,\rho,h)}(h^2+R^2)^{-(j+3)/2}R\, d\, R d\phi, \quad (12)$$

in which the limits $\pm\frac{1}{2}\psi(\theta,\rho,h)$ of the azimuthal variable ϕ are indicated in figures 1 and 2. The angular response function $\psi(\theta,\rho,h)$ is the quantity $\psi_S(\theta)$ defined following eq (3), in which the generalized source-detector geometry symbol S has been replaced by the parameters ρ and h which characterize the disk source situation.

Now, since

$$\psi(\theta,\rho,h)=2\cos^{-1}\{(\rho^2+R^2-1)/2\rho R\}, \quad (13)$$

we may write (12) as the single integral

$$F_j(\rho,h)=h^{j+1}\int_{R=\rho-1}^{\rho+1}2R\, dR(h^2+R^2)^{-(j+3)/2} \times\cos^{-1}\{(\rho^2+R^2-1)/2\rho R\}. \quad (14)$$

Integration by parts and use of the substitution

$$R^2=\rho^2+1-2\rho\cos t \quad (15)$$

transforms (14) to the form

$$F_j(\rho,h)=\frac{h^{j+1}}{j+1}\times \left\{(\rho^2-1)\int_0^\pi \frac{dt}{(\rho^2+1-2\rho\cos t)(h^2+\rho^2+1-2\rho\cos t)^{\frac{j+1}{2}}} -\int_0^\pi\frac{dt}{(h^2+\rho^2+1-2\rho\cos t)^{\frac{j+1}{2}}}\right\}. \quad (16)$$

The first of the two integrals in (16) may be further reduced by use of the identity

$$\frac{1}{a^2(h^2+a^2)^j}=\frac{1}{a^2h^{2j}}-\sum_{i=0}^{j-1}\frac{1}{h^{2j-2i}}\cdot\frac{1}{(h^2+a^2)^{i+1}}, \quad (17)$$

in which $a^2=\rho^2+1-2\rho\cos t$.

Since at this point the evaluation of the integral for the case of odd j (and thus odd l) is quite different from that for even j, these cases will be treated separately in subsections A and B, as follows:

[5] The limits of integration $\rho-1$, $\rho+1$ in (12) refer to the case $1\leq\rho\leq\infty$. For $0\leq\rho<1$ the integral should be split into the ranges $0\leq R\leq 1-\rho$ and $1-\rho\leq R\leq 1+\rho$. However, the resulting expressions are identical.

A. Even j,l

Combining (16) and (17) we have for the F-integrals for even j, denoted as F_{2j}, where $j=0, 1, 2\ldots$,

$$F_{2j}(\rho,h)=\frac{h^{2j+1}}{2j+1} \times\left\{\frac{\rho^2-1}{h^{2j}}\int_0^\pi\frac{dt}{(\rho^2+1-2\rho\cos t)\sqrt{h^2+\rho^2+1-2\rho\cos t}} -(\rho^2-1)\left[\sum_{i=0}^{j-1}\frac{1}{h^{2j-2i}}\int_0^\pi\frac{dt}{(h^2+\rho^2+1-2\rho\cos t)^{i+3/2}}\right] -\int_0^\pi\frac{dt}{(h^2+\rho^2+1-2\rho\cos t)^{j+1/2}}\right\}. \quad (18)$$

The first integral in (18) can be evaluated in terms of complete and incomplete elliptic integrals of the first and second kinds. However, in combining these F_{2j}'s according to (10) to give p_{2l}, it can be shown that for $l>0$ this integral cancels out, i.e., the polynomial $\sum a_{lj}(2j+1)^{-1}$ has the properties

$$\sum a_{lj}(2j+1)^{-1}=\begin{bmatrix}1 \text{ for } l=0\\ 0 \text{ for } l>0, l \text{ even}\end{bmatrix}. \quad (19)$$

The zeroth coefficient $p_0(\rho,h)$ (which is the same as $F_0(\rho,h)$) is the response of an isotropic detector, at an off-axis position ρ,h, to radiation from a "perfectly diffuse" circular disk source, i.e., $g(\theta)=$ constant. Fortunately, $p_0(\rho,h)$ is also the solid angle subtended by a circular disk from the point ρ,h, and in the latter role has been discussed and evaluated by a number of authors [10, 11]. If we use one of these tabulations [6] for p_0, we need only evaluate the integral appearing in (18) in the summation and also in the final term. Factoring out the quantity $(h^2+\rho^2+1)^{-(n+1/2)}$ from this integral reduces it to the form

$$S_n(k)=\int_0^\pi(1-k^2\cos t)^{-(n+1/2)}dt, \quad (20)$$

in which n corresponds to the i and j in (18) and $k^2=2\rho/(h^2+\rho^2+1)\leq 1$. This family of integrals may be evaluated in terms of complete elliptic integrals of the first and second kinds [12].

$$S_0(k)=\frac{2}{\sqrt{1+k^2}}K\left(\sqrt{\frac{2k^2}{1+k^2}}\right), \quad (21)$$

$$S_1(k)=\frac{2}{(1-k^2)\sqrt{1+k^2}}E\left(\sqrt{\frac{2k^2}{1+k^2}}\right), \quad (22)$$

and for $n\geq 2$,

$$S_n(k)=\frac{1}{1-k^4}\left\{\left(1+\frac{2n-3}{2n-1}\right)S_{n-1}-\frac{2n-3}{2n-1}S_{n-2}\right\}. \quad (23)$$

[6] For tabulations of p_0 see, for example, references [10] and [11]. The parameters ρ and h in this paper were explicitly selected in order to use directly the extensive table in reference [11].

Extensive tabulations [13] of K and E exist in addition to an excellent polynomial approximation by Hastings [14] suitable for use on a high-speed computer.

Substituting (20) into (18) we have

$$F_{2j}(\rho,h)=\{\text{cancellation terms in } p_{2l}(\rho,h) \text{ for } l>0\}$$
$$-\frac{1}{2j+1}\left\{\left(\frac{h^2}{h^2+\rho^2+1}\right)^{j+1/2}S_j(k)+\frac{\rho^2-1}{h^2}\sum_{i=1}^{j}\left(\frac{h^2}{h^2+\rho^2+1}\right)^{i+1/2}S_i(k)\right\}. \quad (24)$$

The even-l response function coefficients $p_{2l}(\rho,h)$ may then be built up from the $F_{2j}(\rho,h)$'s in (24) as indicated in (10). Equation (10) may be written more explicitly for even l as

$$p_{2l}(\rho,h)=\sum_{j=0}^{l}\frac{(-1)^j}{2^{2l}}\binom{2l-j}{j}\binom{4l-2j}{2l-j}F_{2l-2j}(\rho,h), \quad (25)$$

in which the quantity

$$\binom{n}{r}=\frac{n!}{r!(n-r)!} \quad (26)$$

is the rth coefficient of an nth degree binomial expansion.

B. Odd j,l

Denoting the odd-j F-integrals in (16) as $F_{2j+1}(\rho,h)$ where $j=0, 1, 2, \ldots$, we have, using (17),

$$F_{2j+1}(\rho,h)=\frac{1}{2j+2}\left\{(\rho^2-1)\int_0^\pi\frac{dt}{(\rho^2+1-2\rho\cos t)}-\frac{\rho^2-1}{h^2}\left[\sum_{i=0}^{j}h^{2i+2}\int_0^\pi\frac{dt}{(h^2+\rho^2+1-2\rho\cos t)^{i+1}}\right]-h^{2j+2}\int_0^\pi\frac{dt}{(h^2+\rho^2+1-2\rho\cos t)^{j+1}}\right\}. \quad (27)$$

Since the integrand denominators have integers, rather than half-integers, as exponents, closed-form algebraic expressions result, rather than quantities in terms of tabulated higher functions or infinite series expansions. Use of standard integral tables [15] to evaluate (27) gives

$$F_{2j+1}(\rho,h)=\frac{\pi}{2j+2}\left\{1-\left(\frac{h^2}{\sqrt{(h^2-\rho^2+1)^2+4\rho^2h^2}}\right)^{j+1}P_j\left(\frac{h^2+\rho^2+1}{\sqrt{(h^2-\rho^2+1)^2+4\rho^2h^2}}\right)-\frac{\rho^2-1}{h^2}\sum_{i=0}^{j}\left(\frac{h^2}{\sqrt{(h^2-\rho^2+1)^2+4\rho^2h^2}}\right)^{i+1}\times P_i\left(\frac{h^2+\rho^2+1}{\sqrt{(h^2-\rho^2+1)^2+4\rho^2h^2}}\right)\right\}, \quad (28)$$

in which $(\cos\theta)^m$ is replaced by

$$\{(h^2+\rho^2+1)/\sqrt{(h^2-\rho^2+1)^2+4\rho^2h^2}\}^m$$

in the usual Legendre polynomials $P_n(\cos\theta)$ to give the quantities P_i and P_j in (28).

Substituting (28) into (10), we have for the first two odd-l coefficients

$$p_1(\rho,h)=\frac{\pi}{2}\left(1-\frac{h^2+\rho^2-1}{\sqrt{(h^2-\rho^2+1)^2+4\rho^2h^2}}\right) \quad (29)$$

and

$$p_3(\rho,h)=\frac{\pi}{8}\left\{-1+\frac{6h^2+\rho^2-1}{\sqrt{(h^2-\rho^2+1)^2+4\rho^2h^2}}-\frac{5h^2(h^2+\rho^2-1)(h^2+\rho^2+1)}{[(h^2-\rho^2+1)^2+4\rho^2h^2]^{3/2}}\right\}. \quad (30)$$

The higher odd-l terms can be written in a form comparable to (25) as

$$p_{2l+1}(\rho,h)=\sum_{j=0}^{l}\frac{(-1)^j}{2^{2l+1}}\times\binom{2l-j+1}{j}\binom{4l-2j+2}{2l-j+1}F_{2l-2j+1}(\rho,h) \quad (31)$$

using the $F_{2j+1}(\rho,h)$'s from (28).

The $p_1(\rho,h)$ coefficient in (29) is equivalent to the response of a plane detector parallel to the plane of a perfectly diffuse (Lambert's law) uniform circular disk source, and has been derived and discussed by a number of authors [16].

The $F_{2j}(\rho,h)$ and $F_{2j+1}(\rho,h)$ expressions in (24) and (28), and the expressions in (25) and (31) for their respective Legendre combinations were programed for evaluation of the $p_l(\rho,h)$'s on an IBM 704 computer. The resulting numerical values for the $p_l(\rho,h)$ are presented in table 1 for $0\leq\rho\leq10$, $0.1\leq h\leq10$ and $1\leq l\leq13$. The entries for $p_0(\rho,h)$ were taken from reference [11]. For ρ or h greater than 10, the source may be treated for all practical purposes as a point anisotropic source with the same angular distribution, $g(\theta)\cos\emptyset$, as each surface element of the source. The $p_l(\rho,h)$ coefficients in table 1 may now be combined with g_l coefficients as in equation (6) to give the radiation flux intercepted by a small spherical detector at coordinates ρ,h.

As a check on these $p_l(\rho,h)$'s, they may be inserted in (5) to reconstruct the angular response function $\psi(\theta,\rho,h)$. Three detector positions ($\rho=0.5$, $h=0.5$; $\rho=1$, $h=1$; $\rho=2$, $h=1$) are indicated in figure 3, and the exact angular response functions for these positions are given by the solid lines in figure 4. Summing over the first 10 terms in (5) gives us the approximations shown by the dashed lines in figure 4.

2.2. Cosine Detector

As has been discussed in reference [3], a similar analysis of a finite uniform plane source geometry may be performed in the case of a surface-element detector with response proportional to the cosine of the angle of incidence of the radiation. For the case of a surface-element detector parallel to the

TABLE 1.* *Coefficients $p_l(\rho,h)$ of the Legendre expansion (5) of the angular response function $\psi(\theta,\rho,h)$*

$p_l(\rho, h)$

h	l \ ρ	0	0.2	0.5	0.8	1.0
0.1	0	5.6580 (0)	5.6389 (0)	5.5092 (0)	4.9511 (0)	2.7036 (0)
	1	3.1105 (0)	3.1079 (0)	3.0872 (0)	2.9346 (0)	1.4924 (0)
	2	3.0951 (−1)	3.1855 (−1)	3.7857 (−1)	5.9042 (−1)	1.6880 (−1)
	3	−7.3913 (−1)	−7.3534 (−1)	−7.0554 (−1)	−5.1185 (−1)	−3.2419 (−1)
	4	−2.2677 (−1)	−2.3270 (−1)	−2.6957 (−1)	−3.3127 (−1)	−9.7153 (−2)
	5	3.3572 (−1)	3.3122 (−1)	2.9669 (−1)	1.2095 (−1)	1.4395 (−1)
	6	1.8207 (−1)	1.8596 (−1)	2.0681 (−1)	1.7067 (−1)	6.9956 (−2)
	7	−1.8038 (−1)	−1.7550 (−1)	−1.3959 (−1)	−1.8423 (−2)	−7.7337 (−2)
	8	−1.5130 (−1)	−1.5352 (−1)	−1.6127 (−1)	−7.5020 (−2)	−5.2967 (−2)
	9	1.0068 (−1)	9.5097 (−2)	6.1222 (−2)	5.8812 (−3)	4.6161 (−2)
	10	1.2734 (−1)	1.2811 (−1)	1.2488 (−1)	3.1191 (−2)	4.2324 (−2)
	11	−5.3333 (−2)	−4.8521 (−2)	−1.7867 (−2)	−1.7343 (−2)	−2.8446 (−2)
	12	−1.0734 (−1)	−1.0684 (−1)	−9.4741 (−2)	−2.2105 (−2)	−3.4397 (−2)
	13	2.2831 (−2)	1.8417 (−2)	−6.5421 (−3)	2.4535 (−2)	1.7852 (−2)
	l \ ρ	1.2	1.5	2.0	5.0	10.0
	0	6.0618 (−1)	1.7518 (−1)	5.3816 (−2)	2.6296 (−3)	3.1768 (−4)
	1	1.3539 (−1)	1.9422 (−2)	3.4561 (−3)	5.4493 (−5)	3.2047 (−6)
	2	−2.4825 (−1)	−8.3956 (−2)	−2.6553 (−2)	−1.3131 (−3)	−1.5879 (−4)
	3	−1.7525 (−1)	−2.8306 (−2)	−5.1412 (−3)	−8.1680 (−5)	−4.8063 (−6)
	4	1.0623 (−1)	5.6815 (−2)	1.9299 (−2)	9.8181 (−4)	1.1901 (−4)
	5	1.6643 (−1)	3.3581 (−2)	6.3309 (−3)	1.0196 (−4)	6.0060 (−6)
	6	−1.4981 (−2)	−3.9768 (−2)	−1.5289 (−2)	−8.1427 (−4)	−9.9063 (−5)
	7	−1.2740 (−1)	−3.6289 (−2)	−7.2270 (−3)	−1.1873 (−4)	−7.0039 (−6)
	8	−3.5553 (−2)	2.6539 (−2)	1.2454 (−2)	7.0782 (−4)	8.6547 (−5)
	9	7.8309 (−2)	3.6858 (−2)	7.9006 (−3)	1.3324 (−4)	7.8748 (−6)
	10	5.1249 (−2)	−1.5553 (−2)	−1.0188 (−2)	−6.3174 (−4)	−7.7741 (−5)
	11	−3.6546 (−2)	−3.5609 (−2)	−8.3855 (−3)	−1.4611 (−4)	−8.6560 (−6)
	12	−4.3885 (−2)	6.3576 (−3)	8.2513 (−3)	5.7324 (−4)	7.1095 (−5)
	13	1.1524 (−2)	3.2871 (−2)	8.7016 (−3)	1.5770 (−4)	9.3693 (−6)
0.2	0	5.0510 (0)	5.0156 (0)	4.7828 (0)	3.9593 (0)	2.4052 (0)
	1	3.0208 (0)	3.0113 (0)	2.9394 (0)	2.5521 (0)	1.4145 (0)
	2	5.9242 (−1)	6.0653 (−1)	6.9042 (−1)	8.1628 (−1)	2.6714 (−1)
	3	−6.0696 (−1)	−5.9725 (−1)	−5.0554 (−1)	−1.7057 (−1)	−2.5690 (−1)
	4	−4.0444 (−1)	−4.0939 (−1)	−4.2399 (−1)	−2.4971 (−1)	−1.4043 (−1)
	5	1.8601 (−1)	1.7310 (−1)	9.0334 (−2)	−7.4080 (−3)	9.3690 (−2)
	6	2.8843 (−1)	2.8648 (−1)	2.5294 (−1)	5.7523 (−2)	9.3989 (−2)
	7	−2.4333 (−2)	−1.3696 (−2)	4.0103 (−2)	−3.7853 (−2)	−3.5202 (−2)
	8	−2.0024 (−1)	−1.9326 (−1)	−1.3335 (−1)	−5.9687 (−2)	−6.4854 (−2)
	9	−4.9727 (−2)	−5.6315 (−2)	−7.1927 (−2)	2.6729 (−2)	1.0905 (−2)
	10	1.2879 (−1)	1.1895 (−1)	5.5438 (−2)	7.2910 (−2)	4.6952 (−2)
	11	8.1495 (−2)	8.3167 (−2)	6.2859 (−2)	1.8096 (−2)	1.7315 (−3)
	12	−7.0789 (−2)	−6.0437 (−2)	−1.2489 (−2)	−4.1686 (−2)	−3.3718 (−2)
	13	−8.8823 (−2)	−8.5486 (−2)	−4.0990 (−2)	−2.8918 (−2)	−7.7467 (−3)
	l \ ρ	1.2	1.5	2.0	5.0	10.0
	0	9.7005 (−1)	3.3005 (−1)	1.0554 (−1)	5.2489 (−3)	6.3507 (−4)
	1	3.6408 (−1)	7.0472 (−2)	1.3424 (−2)	2.1740 (−4)	1.2811 (−5)
	2	−2.4386 (−1)	−1.3978 (−1)	−5.0043 (−2)	−2.6108 (−3)	−3.1715 (−4)
	3	−3.4860 (−1)	−9.4767 (−2)	−1.9485 (−2)	−3.2513 (−4)	−1.9203 (−5)
	4	−5.6872 (−2)	6.5955 (−2)	3.2928 (−2)	1.9343 (−3)	2.3718 (−4)
	5	1.7291 (−1)	9.6607 (−2)	2.2940 (−2)	4.0426 (−4)	2.3975 (−5)
	6	1.2253 (−1)	−1.5020 (−2)	−2.1798 (−2)	−1.5809 (−3)	−1.9676 (−4)
	7	−3.1183 (−2)	−8.2335 (−2)	−2.4499 (−2)	−4.6802 (−4)	−2.7921 (−5)
	8	−6.7218 (−2)	−1.9212 (−2)	1.2973 (−2)	1.3466 (−3)	1.7111 (−4)
	9	−2.8126 (−3)	5.8673 (−2)	2.4463 (−2)	5.2123 (−4)	3.1338 (−5)
	10	2.3823 (−2)	3.7369 (−2)	−5.5921 (−3)	−1.1705 (−3)	−1.5279 (−4)
	11	−1.2139 (−2)	−3.2733 (−2)	−2.3072 (−2)	−5.6621 (−4)	−3.4373 (−5)
	12	−2.6654 (−2)	−4.1470 (−2)	−5.4447 (−4)	1.0276 (−3)	1.3873 (−4)
	13	9.2864 (−3)	1.0522 (−2)	2.0585 (−2)	6.0426 (−4)	3.7109 (−5)
0.5	0	3.4733 (0)	3.4184 (0)	3.1022 (0)	2.4123 (0)	1.7687 (0)
	1	2.5133 (0)	2.4802 (0)	2.2733 (0)	1.7426 (0)	1.1898 (0)
	2	1.1240 (0)	1.1232 (0)	1.0865 (0)	8.2414 (−1)	4.2719 (−1)
	3	0.0000	2.3936 (−2)	1.3416 (−1)	1.5252 (−1)	−7.3353 (−2)
	4	−4.4959 (−1)	−4.2364 (−1)	−2.6953 (−1)	−6.8444 (−2)	−1.6341 (−1)
	5	−3.0159 (−1)	−2.9631 (−1)	−2.1987 (−1)	6.2302 (−3)	−2.6599 (−2)
	6	4.4959 (−2)	2.5241 (−2)	−2.9195 (−2)	9.8306 (−2)	7.5291 (−2)
	7	2.2117 (−1)	1.9522 (−1)	6.6073 (−2)	7.1346 (−2)	4.7875 (−2)
	8	1.3498 (−1)	1.2808 (−1)	3.9757 (−2)	−1.6869 (−2)	−2.4193 (−2)
	9	−5.2276 (−2)	−3.2603 (−2)	−8.3723 (−3)	−5.7460 (−2)	−3.9802 (−2)
	10	−1.3847 (−1)	−1.1162 (−1)	−8.4522 (−3)	−2.8599 (−2)	−1.1920 (−4)
	11	−6.9165 (−2)	−6.2655 (−2)	1.9010 (−2)	8.6621 (−3)	2.8202 (−2)
	12	5.1793 (−2)	3.0551 (−2)	2.1923 (−2)	5.9185 (−3)	1.2729 (−2)
	13	9.5706 (−2)	6.8208 (−2)	−7.9961 (−3)	−2.0240 (−2)	−1.4838 (−2)

TABLE 1.* *Coefficients $p_l(\rho,h)$ of the Legendre expansion (5) of the angular response function ψ (θ,ρ,h)*—Continued

$p_l(\rho, h)$

h=0.5	l \ ρ	1.2	1.5	2.0	5.0	10.0
	0	1.1661 (0)	5.9692 (−1)	2.3242 (−1)	1.2945 (−2)	1.5826 (−3)
	1	6.7870 (−1)	2.6382 (−1)	6.9462 (−2)	1.3339 (−3)	7.9725 (−5)
	2	6.7922 (−2)	−1.0857 (−1)	−8.3311 (−2)	−6.2644 (−3)	−7.8526 (−4)
	3	−2.7369 (−1)	−2.3352 (−1)	−8.6034 (−2)	−1.9643 (−3)	−1.1908 (−4)
	4	−2.4935 (−1)	−9.7788 (−2)	1.5867 (−2)	4.3407 (−3)	5.7842 (−4)
	5	−6.2514 (−2)	8.1473 (−2)	7.3710 (−2)	2.3747 (−3)	1.4771 (−4)
	6	4.6779 (−2)	1.1907 (−1)	2.6715 (−2)	−3.1647 (−3)	−4.6834 (−4)
	7	2.2690 (−2)	3.0262 (−2)	−4.4313 (−2)	−2.6379 (−3)	−1.7041 (−4)
	8	−3.1217 (−2)	−4.9324 (−2)	−4.5078 (−2)	2.2555 (−3)	3.9367 (−4)
	9	−2.5263 (−2)	−4.4582 (−2)	1.1501 (−2)	2.7791 (−3)	1.8892 (−4)
	10	2.1162 (−2)	9.5174 (−4)	4.2228 (−2)	−1.4823 (−3)	−3.3618 (−4)
	11	4.0843 (−2)	1.7678 (−2)	1.3162 (−2)	−2.8121 (−3)	−2.0405 (−4)
	12	1.7192 (−2)	6.0857 (−4)	−2.6483 (−2)	8.0373 (−4)	2.8842 (−4)
	13	−8.5251 (−3)	−9.0943 (−3)	−2.4048 (−2)	2.7473 (−3)	2.1626 (−4)

h=1.0	l \ ρ	0	0.2	0.5	0.8	1.0
	0	1.8403 (0)	1.8071 (0)	1.6371 (0)	1.3488 (0)	1.1227 (0)
	1	1.5708 (0)	1.5394 (0)	1.3760 (0)	1.0921 (0)	8.6832 (−1)
	2	1.1107 (0)	1.0855 (0)	9.4773 (−1)	6.9040 (−1)	4.8242 (−1)
	3	5.8905 (−1)	5.7689 (−1)	4.9529 (−1)	3.0375 (−1)	1.3416 (−1)
	4	1.3884 (−1)	1.4450 (−1)	1.4522 (−1)	5.4083 (−2)	−5.9580 (−2)
	5	−1.4726 (−1)	−1.2475 (−1)	−4.2344 (−2)	−2.8548 (−2)	−8.8156 (−2)
	6	−2.4297 (−1)	−2.1313 (−1)	−8.4731 (−2)	5.7923 (−4)	−2.6783 (−2)
	7	−1.8715 (−1)	−1.6474 (−1)	−4.8632 (−2)	5.4400 (−2)	3.2267 (−2)
	8	−5.8573 (−2)	−5.6131 (−2)	−4.4268 (−3)	7.2884 (−2)	4.1359 (−2)
	9	6.0592 (−2)	4.0296 (−2)	9.2186 (−3)	4.7889 (−2)	1.1747 (−2)
	10	1.1660 (−1)	8.3307 (−2)	−6.4612 (−3)	9.6586 (−3)	−1.7466 (−2)
	11	9.8846 (−2)	7.0358 (−2)	−2.7259 (−2)	−1.0087 (−2)	−2.0649 (−2)
	12	3.3964 (−2)	2.6471 (−2)	−3.1179 (−2)	−5.3664 (−3)	−2.9665 (−3)
	13	−3.4778 (−2)	−1.6224 (−2)	−1.4585 (−2)	1.0427 (−2)	1.3218 (−2)

	l \ ρ	1.2	1.5	2.0	5.0	10.0
	0	9.0037 (−1)	6.1910 (−1)	3.2580 (−1)	2.4092 (−2)	3.1293 (−3)
	1	6.5297 (−1)	3.9677 (−1)	1.6583 (−1)	5.0026 (−3)	3.1407 (−4)
	2	2.8932 (−1)	8.8340 (−2)	−3.1552 (−2)	−1.0811 (−2)	−1.5173 (−3)
	3	−1.6324 (−2)	−1.2518 (−1)	−1.2927 (−1)	−6.9761 (−3)	−4.6313 (−4)
	4	−1.5564 (−1)	−1.8651 (−1)	−8.8713 (−2)	5.6155 (−3)	1.0564 (−3)
	5	−1.3742 (−1)	−1.0432 (−1)	1.4583 (−2)	7.6054 (−3)	5.6125 (−4)
	6	−5.2771 (−2)	3.1764 (−3)	7.5614 (−2)	−1.8398 (−3)	−7.7084 (−4)
	7	6.4034 (−3)	5.2785 (−2)	5.4384 (−2)	−7.1757 (−3)	−6.2598 (−4)
	8	7.7352 (−3)	3.7389 (−2)	−6.5513 (−3)	−1.1179 (−3)	5.6176 (−4)
	9	−2.1418 (−2)	3.4071 (−3)	−4.2034 (−2)	5.9087 (−3)	6.6240 (−4)
	10	−3.8294 (−2)	−7.6326 (−3)	−2.9432 (−2)	3.2646 (−3)	−3.7906 (−4)
	11	−2.6571 (−2)	6.0364 (−3)	3.1900 (−3)	−4.0690 (−3)	−6.7448 (−4)
	12	−2.4071 (−3)	1.8936 (−2)	1.9108 (−2)	−4.5379 (−3)	2.1756 (−4)
	13	1.0215 (−2)	1.3014 (−2)	1.0859 (−2)	1.9391 (−3)	6.6418 (−4)

h=2.0	l \ ρ	0	0.2	0.5	0.8	1.0
	0	6.6333 (−1)	6.5663 (−1)	6.2286 (−1)	5.6597 (−1)	5.1954 (−1)
	1	6.2832 (−1)	6.2033 (−1)	5.8026 (−1)	5.1359 (−1)	4.6008 (−1)
	2	5.6199 (−1)	5.5195 (−1)	5.0190 (−1)	4.3003 (−1)	3.5598 (−1)
	3	4.7124 (−1)	4.5928 (−1)	3.9695 (−1)	3.0454 (−1)	2.3208 (−1)
	4	3.6529 (−1)	3.5254 (−1)	2.8937 (−1)	1.8915 (−1)	1.1540 (−1)
	5	2.5447 (−1)	2.4285 (−1)	1.8468 (−1)	9.2889 (−2)	2.7138 (−2)
	6	1.4893 (−1)	1.4073 (−1)	9.8168 (−2)	2.7404 (−2)	−2.2682 (−2)
	7	5.7413 (−2)	5.4681 (−2)	3.6001 (−2)	−4.9330 (−3)	−3.6350 (−2)
	8	−1.3098 (−2)	−9.7870 (−3)	−3.7792 (−4)	−1.0030 (−2)	−2.5404 (−2)
	9	−6.1018 (−2)	−5.0573 (−2)	−1.4595 (−2)	1.1624 (−3)	−4.9848 (−3)
	10	−8.4305 (−2)	−6.8873 (−2)	−1.3479 (−2)	1.6823 (−2)	1.1925 (−2)
	11	−8.6195 (−2)	−6.8555 (−2)	−4.9232 (−3)	2.7909 (−2)	1.8444 (−2)
	12	−7.1549 (−2)	−5.5188 (−2)	4.1327 (−3)	3.0222 (−2)	1.4479 (−2)
	13	−4.6553 (−2)	−3.4932 (−2)	9.1247 (−3)	2.4418 (−2)	4.7874 (−3)

	l \ ρ	1.2	1.5	2.0	5.0	10.0
	0	4.6970 (−1)	3.9438 (−1)	2.8271 (−1)	4.1460 (−2)	5.9847 (−3)
	1	4.0376 (−1)	3.2134 (−1)	2.0086 (−1)	1.5787 (−2)	1.1832 (−3)
	2	2.9065 (−1)	2.0014 (−1)	8.9034 (−2)	−1.1646 (−2)	−2.6407 (−3)
	3	1.6107 (−1)	6.9906 (−2)	−2.1766 (−2)	−1.7831 (−2)	−1.6583 (−3)
	4	4.6708 (−2)	−3.2114 (−2)	−8.5503 (−2)	−3.1794 (−3)	1.4056 (−3)
	5	−3.0151 (−2)	−8.4575 (−2)	−8.9092 (−2)	1.1935 (−2)	1.8256 (−3)
	6	−6.2584 (−2)	−8.7743 (−2)	−5.0978 (−2)	1.0892 (−2)	−5.0880 (−4)
	7	−5.8611 (−2)	−5.9240 (−2)	−1.3490 (−3)	−2.4198 (−3)	−1.7496 (−3)
	8	−3.5329 (−2)	−2.3059 (−2)	3.1301 (−2)	−1.1062 (−2)	−2.0353 (−4)
	9	−1.0087 (−2)	2.0473 (−3)	3.6461 (−2)	−5.7689 (−3)	1.4767 (−3)
	10	3.4017 (−3)	9.2652 (−3)	2.1731 (−2)	5.5909 (−3)	7.3707 (−4)
	11	4.0067 (−3)	3.2242 (−3)	3.1477 (−3)	9.1154 (−3)	−1.0619 (−3)
	12	−4.2982 (−3)	−5.9353 (−3)	−6.8639 (−3)	1.5814 (−3)	−1.0761 (−3)
	13	−1.3803 (−2)	−9.7357 (−3)	−5.9984 (−3)	−7.0051 (−3)	5.6923 (−4)

TABLE 1.* *Coefficients $p_l(\rho,h)$ of the Legendre expansion (5) of the angular response function $\psi(\theta,\rho,h)$*—Continued

$p_l(\rho, h)$

h=5.0 l \ ρ	0	0.2	0.5	0.8	1.0
0	1.2202 (−1)	1.2174 (−1)	1.2033 (−1)	1.1776 (−1)	1.1547 (−1)
1	1.2083 (−1)	1.2047 (−1)	1.1863 (−1)	1.1520 (−1)	1.1235 (−1)
2	1.1848 (−1)	1.1797 (−1)	1.1528 (−1)	1.1050 (−1)	1.0628 (−1)
3	1.1502 (−1)	1.1427 (−1)	1.1041 (−1)	1.0358 (−1)	9.7641 (−2)
4	1.1051 (−1)	1.0947 (−1)	1.0417 (−1)	9.4882 (−2)	8.6923 (−2)
5	1.0503 (−1)	1.0368 (−1)	9.6759 (−2)	8.4810 (−2)	7.4740 (−2)
6	9.8700 (−2)	9.7005 (−2)	8.8421 (−2)	7.3820 (−2)	6.1761 (−2)
7	9.1627 (−2)	8.9600 (−2)	7.9414 (−2)	6.2393 (−2)	4.8664 (−2)
8	8.3946 (−2)	8.1617 (−2)	7.0009 (−2)	5.1001 (−2)	3.6090 (−2)
9	7.5798 (−2)	7.3219 (−2)	6.0477 (−2)	4.0086 (−2)	2.4596 (−2)
10	6.7330 (−2)	6.4572 (−2)	5.1080 (−2)	3.0033 (−2)	1.4624 (−2)
11	5.8690 (−2)	5.5842 (−2)	4.2057 (−2)	2.1148 (−2)	6.4728 (−3)
12	5.0028 (−2)	4.7193 (−2)	3.3619 (−2)	1.3649 (−2)	2.9255 (−4)
13	4.1487 (−2)	3.8775 (−2)	2.5939 (−2)	7.6574 (−3)	−3.9175 (−3)

l \ ρ	1.2	1.5	2.0	5.0	10.0
0	1.1277 (−1)	1.0806 (−1)	9.8893 (−2)	4.4590 (−2)	1.1307 (−2)
1	1.0889 (−1)	1.0291 (−1)	9.1512 (−2)	3.1724 (−2)	5.0832 (−3)
2	1.0140 (−1)	9.2079 (−2)	7.7719 (−2)	1.1644 (−2)	−2.2205 (−3)
3	9.0832 (−2)	7.9469 (−2)	5.9298 (−2)	−7.1460 (−3)	−5.0443 (−3)
4	7.7933 (−2)	6.3284 (−2)	3.8554 (−2)	−1.7407 (−2)	−2.3029 (−3)
5	6.3572 (−2)	4.5910 (−2)	1.7958 (−2)	−1.6477 (−2)	2.1603 (−3)
6	4.8683 (−2)	2.8750 (−2)	−2.3434 (−4)	−7.1132 (−3)	3.6874 (−3)
7	3.4173 (−2)	1.3078 (−2)	−1.4289 (−2)	4.4049 (−3)	1.2290 (−3)
8	2.0853 (−2)	−8.7710 (−5)	−2.3258 (−2)	1.1755 (−2)	−2.1739 (−3)
9	9.3700 (−3)	−1.0080 (−2)	−2.6958 (−2)	1.1721 (−2)	−2.9248 (−3)
10	1.6819 (−4)	−1.6621 (−2)	−2.6000 (−2)	5.4042 (−3)	−5.4759 (−4)
11	−6.5366 (−3)	−1.9815 (−2)	−2.1555 (−2)	−2.9324 (−3)	2.1682 (−3)
12	−1.0753 (−2)	−2.0093 (−2)	−1.5101 (−2)	−8.5369 (−3)	2.3570 (−3)
13	−1.2692 (−2)	−1.8125 (−2)	−8.1402 (−3)	−8.7686 (−3)	4.6573 (−5)

h=10.0 l \ ρ	0	0.2	0.5	0.8	1.0
0	3.1182 (−2)	3.1164 (−2)	3.1068 (−2)	3.0890 (−2)	3.0728 (−2)
1	3.1105 (−2)	3.1081 (−2)	3.0953 (−2)	3.0718 (−2)	3.0504 (−2)
2	3.0951 (−2)	3.0914 (−2)	3.0725 (−2)	3.0376 (−2)	3.0059 (−2)
3	3.0720 (−2)	3.0666 (−2)	3.0384 (−2)	2.9869 (−2)	2.9400 (−2)
4	3.0414 (−2)	3.0337 (−2)	2.9936 (−2)	2.9202 (−2)	2.8539 (−2)
5	3.0035 (−2)	2.9930 (−2)	2.9382 (−2)	2.8385 (−2)	2.7488 (−2)
6	2.9584 (−2)	2.9446 (−2)	2.8728 (−2)	2.7429 (−2)	2.6266 (−2)
7	2.9064 (−2)	2.8889 (−2)	2.7981 (−2)	2.6344 (−2)	2.4889 (−2)
8	2.8476 (−2)	2.8261 (−2)	2.7145 (−2)	2.5145 (−2)	2.3381 (−2)
9	2.7825 (−2)	2.7566 (−2)	2.6228 (−2)	2.3848 (−2)	2.1764 (−2)
10	2.7113 (−2)	2.6808 (−2)	2.5239 (−2)	2.2466 (−2)	2.0063 (−2)
11	2.6343 (−2)	2.5991 (−2)	2.4184 (−2)	2.1018 (−2)	1.8302 (−2)
12	2.5520 (−2)	2.5119 (−2)	2.3074 (−2)	1.9520 (−2)	1.6506 (−2)
13	2.4647 (−2)	2.4198 (−2)	2.1916 (−2)	1.7990 (−2)	1.4702 (−2)

l \ ρ	1.2	1.5	2.0	5.0	10.0
0	3.0532 (−2)	3.0176 (−2)	2.9429 (−2)	2.2412 (−2)	1.1118 (−2)
1	3.0245 (−2)	2.9776 (−2)	2.8801 (−2)	2.0042 (−2)	7.8735 (−3)
2	2.9677 (−2)	2.8988 (−2)	2.7568 (−2)	1.5688 (−2)	2.8106 (−3)
3	2.8838 (−2)	2.7832 (−2)	2.5777 (−2)	1.0051 (−2)	−1.9193 (−3)
4	2.7746 (−2)	2.6336 (−2)	2.3496 (−2)	4.0196 (−3)	−4.4729 (−3)
5	2.6422 (−2)	2.4540 (−2)	2.0810 (−2)	−1.4972 (−3)	−4.1608 (−3)
6	2.4890 (−2)	2.2487 (−2)	1.7818 (−2)	−5.7256 (−3)	−1.6836 (−3)
7	2.3181 (−2)	2.0229 (−2)	1.4627 (−2)	−8.1599 (−3)	1.3314 (−3)
8	2.1327 (−2)	1.7821 (−2)	1.1348 (−2)	−8.6369 (−3)	3.2194 (−3)
9	1.9360 (−2)	1.5318 (−2)	8.0921 (−3)	−7.3437 (−3)	3.1141 (−3)
10	1.7318 (−2)	1.2780 (−2)	4.9635 (−3)	−4.7585 (−3)	1.3036 (−3)
11	1.5235 (−2)	1.0261 (−2)	2.0567 (−3)	−1.5409 (−3)	−1.0422 (−3)
12	1.3148 (−2)	7.8155 (−3)	−5.4776 (−4)	1.6059 (−3)	−2.5824 (−3)
13	1.1089 (−2)	5.4916 (−3)	−2.7864 (−3)	4.0706 (−3)	−2.5433 (−3)

*The figures in parentheses in tables 1, 2, and 3 indicate the power of 10 by which the adjacent entry is to be multiplied; e.g., 2.2831 (−2)=0.022831.

source-plane, table 1 may be used in two different ways:

(a) If the angular distribution data is already in the form of g_l coefficients of a Legendre expansion as given in (4), a new set of coefficients $p'_l(\rho,h)$ may be obtained from the entries in table 1 according to

$$p'_l(\rho,h)=\{lp_{l-1}(\rho,h)+(l+1)p_{l+1}(\rho,h)\}/(2l+1) \qquad (32)$$

which can be combined with the g_l data as in (6).

(b) If the source data are given in terms of the actual angular distribution $g(\theta)$, which could be either a mathematical expression or experimental data, it would be simpler to modify the *source* angular distribution coefficients, that is, to generate Legendre coefficients g'_l of the quantity $g'(\theta)=\cos\theta\, g(\theta)$. These g'_l coefficients could then be combined directly with p_l values from table 1 in the same way as has been specified in (6) for an isotropic detector.

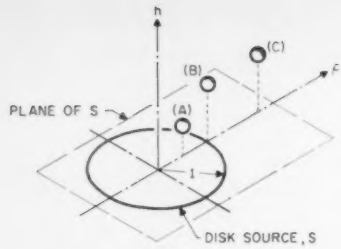

FIGURE 3. *Three examples of detector positions in which the distances off-axis and off source-plane, measured in disk radii, are (A) $\rho=0.5$, $h=0.5$, (B) $\rho=1$, $h=1$ and (C) $\rho=2$, $h=1$.*

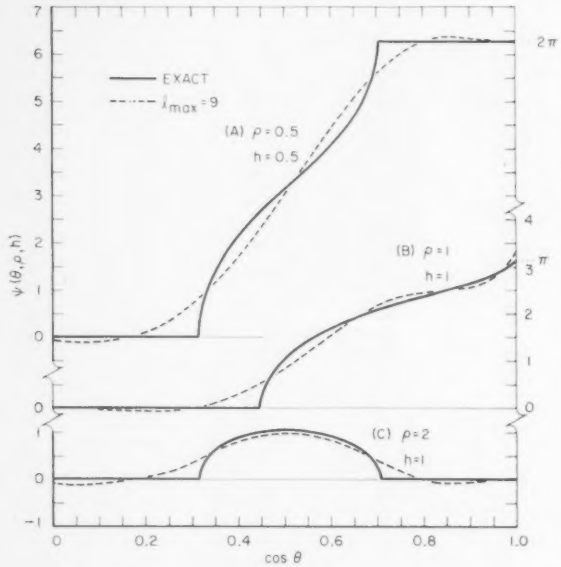

FIGURE 4. *Reconstruction of the response function $\psi(\theta,\rho,h)$ according to (5) for (A) $\rho=.5$, $h=.5$, (B) $\rho=1$, $h=1$ and (C) $\rho=2$, $h=1$ using table 1 and summing over terms $0\leq l\leq 9$. The reconstructed functions are shown as dotted lines and the exact functions as solid lines. Note that the scale for (B) is on the right-hand side.*

2.3. Limitation of the Legendre Expansion Method

The utility of this method is dependent on the oscillatory nature of $P_l(\cos\theta)$. Within any finite region between $\cos\theta$ and $\cos\theta+\Delta\cos\theta$ the increasing number of these oscillations, for increasing l, yields decreasing values of p_l and g_l as a result of higher and higher order cancellations. If both functions $\psi_S(\theta)$ and $g(\theta)$ are concentrated mostly within very *narrow* regions of $\cos\theta$, adequate convergence of (6) may not be achieved without going to exorbitantly high l's.

Evaluation of the unscattered radiation component provides an example of the above limitation. This problem has been qualitatively discussed in section 1, and will be treated in some detail in the following section.

3. Unscattered Radiation Component

3.1. $\tau\gtrsim 1$: Legendre Expansion

As in the rectangular source case [3], the Legendre sum (6) converges adequately for an angular distribution of the form (1) when the barrier thickness $\tau=\mu t$ is of the order of one or greater. In this region the behavior of $g(\theta)$ at the barrier exit surface lies between that of a "perfectly diffuse" plane source $\{g(\theta)=\text{constant}\}$ and that of a plane normal source $\{g(\theta)\propto\delta(\theta-0)\}$. The g_l^o coefficients are easily obtained from appropriate combinations of tabulated exponential integrals [17], and a sample tabulation of g_l^o's is given in reference [3] for $0\leq l\leq 13$ over the range $0.001\leq\tau\leq 100.0$.

3.2. $0\leq\tau\lesssim 1$; $h>0$: Power Series Expansion

Since one of the chief reasons for separate treatment of the unscattered radiation component is the inadequate convergence of (6) for $\tau<<1$, an alternative means of evaluating the integral

$$I^o(\tau,\rho,h)=\frac{\sigma}{4\pi}\int_S (dS/r^2)\exp(-\tau/\cos\theta) \qquad (33)$$

is desirable. Again, as in [3], no success was had in obtaining a closed-form result for $I^o(\tau,\rho,h)$ in (33). However, Sievert [18] has shown that by expanding $\exp(-\tau/\cos\theta)$ as a $(\tau/\cos\theta)^n$ power series, a solution corresponding to eq (10) in reference [3] may be written

$$I^o(\tau,\rho,h)=\frac{\sigma}{4\pi}\sum_{n=0}^{\infty} q_n(\rho,h)\tau^n, \qquad (34)$$

in which the $q_n(\rho,h)$ coefficients are evaluations of the integrals

$$q_n(\rho,h)=\frac{(-1)^n}{n!h^n}\int_{\rho-1}^{\rho+1}(h^2+R^2)^{\frac{n}{2}-1}2\cos^{-1}\left(\frac{\rho^2+R^2}{2\rho R}\right)RdR \qquad (35)$$

for $1\leq\rho\leq\infty$ and

$$q_n(\rho,h)=\frac{(-1)^n}{n!h^n}\left\{\int_0^{1-\rho}(h^2+R^2)^{\frac{n}{2}-1}2\pi RdR + \int_{1-\rho}^{1+\rho}(h^2+R^2)^{\frac{n}{2}-1}2\cos^{-1}\left(\frac{\rho^2+R^2-1}{2\rho R}\right)RdR\right\} \qquad (36)$$

for $0\leq\rho\leq 1$. As in the $p_l(\rho,h)$ evaluation, three distinct expressions arise from (35) and (36) depending on whether n is zero, even or odd, but by proper manipulation the distinctions between results from (35) and (36) were removed. In reference [18], $q_n(\rho,h)$ coefficients are given only for $n=0$, 1, and 2, of which $q_1(\rho,h)$ is not exact.

The zeroth coefficient $q_0(\rho,h)$, when multiplied by the source strength factor $\sigma/4\pi$, is the radiation field from a disk source in a nonattenuating medium (i.e., $\tau=0$). This can be written, for $h>0$, as [18]

$$q_0(\rho,h)=I^o_{\tau=0}4\pi/\sigma=\pi\ln\{(1+h^2-\rho^2+\sqrt{(1+h^2-\rho^2)^2+4\rho^2h^2})/2h^2\}. \quad (37)$$

Higher even-n terms (i.e., $n(e)=2, 4, 6, \ldots$) are closed-form purely algebraic expressions, the next two of which are

$$q_2(\rho,h)=\frac{\pi}{2!h^2} \quad (38)$$

and

$$q_4(\rho,h)=\frac{\pi}{4!h^4}(h^2+\rho^2+\tfrac{1}{2}). \quad (39)$$

These are included in the general expression for the even-n terms:

$$q_{n(e)}(\rho,h)=\frac{\pi}{n\cdot n!}\left\{-1+\left(\frac{h^2+\rho^2+1}{h^2}\right)^{n/2}\left\{\sum_{i=0}^{i_{\max}\le n/4}\binom{2i}{i}\binom{n/2}{2i}\left(\frac{\rho}{h^2+\rho^2+1}\right)^{2i}+\frac{\rho^2-1}{\rho^2+1}\sum_{i=0}^{i_{\max}\le(n/4-1/2)}\binom{2i}{i}\left(\frac{\rho}{\rho^2+1}\right)^{2i}\left[\left(\frac{h^2}{h^2+\rho^2+1}\right)^{n/2}-\sum_{m=0}^{2i}(-1)^m\binom{n/2}{m}\left(\frac{\rho^2+1}{h^2+\rho^2+1}\right)^m\right]\right\}\right\}. \quad (40)$$

The odd-n terms (i.e., $n(o)=1, 3, 5, \ldots$) are all included in the series-expansion solution

$$q_{n(o)}(\rho,h)=-\frac{\pi}{n\cdot n!}\left\{-1+\left(\frac{h^2+\rho^2+1}{h^2}\right)^{n/2}\left\{\sum_{i=0}^{\infty}\binom{2i}{i}\binom{n/2}{2i}\left(\frac{\rho}{h^2+\rho^2+k}\right)^{2i}+\frac{\rho^2-1}{\rho^2+1}\sum_{i=0}^{\infty}\binom{2i}{i}\left(\frac{\rho}{\rho^2+1}\right)^{2i}\left[\left(\frac{h^2}{h^2+\rho^2+1}\right)^{n/2}-\sum_{m=0}^{2i}(-1)^m\binom{n/2}{m}\left(\frac{\rho^2+1}{h^2+\rho^2+1}\right)^m\right]\right\}\right\}, \quad (41)$$

which strongly resembles (40), except that here the quantities $\binom{n/2}{2i}$ and $\binom{n/2}{m}$ are now coefficients of the *infinite* series expansion of half-integral powers of a binomial [19], i.e.,

$$(1+x)^{n/2}=\sum_{m=0}^{\infty}\binom{n/2}{m}x^m. \quad (42)$$

These are readily generated using the recursion

$$\left.\begin{aligned}&\binom{n/2}{0}=1\\&\binom{n/2}{1}=n/2, \text{ and}\\&\binom{n/2}{m}=-\frac{2(m-1)-n}{2m}\binom{n/2}{m-1},\end{aligned}\right\} \quad (43)$$

which is also valid when $n/2$ is an integer, since $\binom{n/2}{m}$, using (43), is zero for $m>n/2$.

By setting $\rho=0$ in (37), (40) and (41) and substituting the resulting values for $q_n(\rho,h)$ in (34), we find the on-axis unscattered flux to be

$$I^o(0,h)=(\sigma/4\pi)2\pi\left[\ln\frac{\sqrt{h^2+1}}{h}+\sum_{n=1}^{\infty}\frac{(-1)^n}{n\cdot n!}\left\{\left(\frac{\sqrt{h^2+1}}{h}\right)^n-1\right\}\tau^n\right]. \quad (44)$$

This series can be identified with the familiar on-axis solution in terms of exponential integrals [20]

$$I^o(0,h)=(\sigma/4\pi)\int_h^{\sqrt{h^2+1}}\frac{e^{-\mu r}}{r^2}2\pi r dr$$

$$=(\sigma/4\pi)2\pi\{E_1(\tau)-E_1(\tau\sqrt{h^2+1}/h)\}. \quad (45)$$

Equations (37), (40) and (41) were programed for evaluation on an IBM 704 computer and a resulting set of $q_n(\rho,h)$ coefficients for $0\le\rho\le10$, $0.1\le h<10$ and $0\le n\le9$ is given in table 2.

3.3. Comparison of Legendre and Power Series Expansions

As a partial check on tables 1 and 2, and because the unscattered radiation component is of some general interest, the quantities $I^o(\tau,\rho,h)4\pi/\sigma$ as defined in (33) were evaluated using the methods of the preceding two sections, and are given in table 3. Numbers preceded by asterisks were evaluated using the Legendre expansion approach (6) with g_l^o values from reference [3] and $0\le l\le13$; the others are evaluated using the τ^n series (34) for $0\le n\le20$.

Some notion of the convergence for each method may be obtained from table 4, in which partial sums over $0\le l\le13$ and $0\le n\le13$ for $\tau=1.0$ are given for the three situations shown in figure 3. A qualitative comment about the Legendre sums for these three cases is that in each case the first two terms contribute over 80 percent of the result.

For scattered radiation the tendency is toward even faster convergence. For example, the Fermi approximation [21]

$$g(\theta)=(1+\sqrt{3}\cos\theta)/(1+\sqrt{3}/2), \quad (46)$$

used in reference [7] for the angular distribution of neutrons from a reactor thermal-column face, has been shown by Placzek [22] to be in error by less than one percent for $0.1<\cos\theta<1$, with a maximum error of 7.2 percent at $\cos\theta=0$. The Legendre expansion coefficients for the $g(\theta)$ in (46) are: $g_0=1.072$, $g_1=0.6188$ and $g_{l\ge2}=0$, which may be used with the p_l values in table 1 according to (6).

TABLE 2. *Coefficients $q'_n(\rho,h)$ $[=h^n q_n(\rho,h)]$ of the $(\tau/h)^n$ power series expansion (34) of the unscattered component $(4\pi/\sigma)I^0(\tau,\rho,h)$ of the radiation flux, from a circular plane isotropic source, incident on a detector at position ρ,h separated from the source-plane by an attenuating layer of thickness $\tau=\mu t$. Each term contains the factor h^n in order to include meaningful tabulations in the region $\rho>1, h\approx 0$ as in (47).*

$q_n'(\rho,h)=h^n q_n(\rho,h)$

$h=0$	n \ ρ	0	0.2	0.5	0.8	1.0
	0					
	1					
	2					
	3		[No physical solution within the radiating surface.]			
	4					
	5					
	6					
	7					
	8					
	9					
	n \ ρ	1.2	1.5	2.0	5.0	10.0
	0	3.6157 (0)	1.8465 (0)	9.0378 (−1)	1.2825 (−1)	3.1574 (−2)
	1	−2.9533 (0)	−2.2364 (0)	−1.6252 (0)	−6.3151 (−1)	−3.1455 (−1)
	2	1.5708 (0)	1.5708 (0)	1.5708 (0)	1.5708 (0)	1.5708 (0)
	3	−6.8470 (−1)	−8.2092 (−1)	−1.0803 (0)	−2.6311 (0)	−5.2425 (0)
	4	2.5395 (−1)	3.5997 (−1)	5.8905 (−1)	3.3379 (0)	1.3155 (1)
	5	−8.1621 (−2)	−1.3336 (−1)	−2.6896 (−1)	−3.4200 (0)	−2.6475 (1)
	6	2.3069 (−2)	4.3179 (−2)	1.0617 (−1)	2.9467 (0)	4.4507 (1)
	7	−5.8064 (−3)	−1.2414 (−2)	−3.6969 (−2)	−2.1951 (0)	−6.4288 (1)
	8	1.3158 (−3)	3.2080 (−3)	1.1551 (−2)	1.4425 (0)	8.1446 (1)
	9	−2.7095 (−4)	−7.5263 (−4)	−3.2677 (−3)	−8.4902 (−1)	−9.1932 (1)
$h=0.1$	n \ ρ	0	0.2	0.5	0.8	1.0
	0	1.4499 (1)	1.4373 (1)	1.3619 (1)	1.1476 (1)	7.3908 (0)
	1	−5.6862 (0)	−5.6239 (0)	−5.2804 (0)	−4.5455 (0)	−3.7113 (0)
	2	1.5708 (0)	1.5708 (0)	1.5708 (0)	1.5708 (0)	1.5708 (0)
	3	−3.5397 (−1)	−3.6436 (−1)	−4.1803 (−1)	−5.1342 (−1)	−5.9576 (−1)
	4	6.6759 (−2)	7.1995 (−2)	9.9484 (−2)	1.5054 (−1)	1.9766 (−1)
	5	−1.0736 (−2)	−1.2326 (−2)	−2.1058 (−2)	−3.8949 (−2)	−5.7335 (−2)
	6	1.4985 (−3)	1.8581 (−3)	3.9747 (−3)	8.9266 (−3)	1.4676 (−2)
	7	−1.8441 (−4)	−2.5003 (−4)	−6.7332 (−4)	−1.8285 (−3)	−3.3511 (−3)
	8	2.0270 (−5)	3.0378 (−5)	1.0316 (−4)	3.3788 (−4)	6.8960 (−4)
	9	−2.0120 (−6	−3.3635 (−6)	−1.4403 (−5)	−5.6805 (−5)	−1.2903 (−4)
	n \ ρ	1.2	1.5	2.0	5.0	10.0
	0	3.6033 (0)	1.8269 (0)	9.0031 (−1)	1.2819 (−1)	3.1571 (−2)
	1	−2.9136 (0)	−2.2276 (0)	−1.6225 (0)	−6.3138 (−1)	−3.1454 (−1)
	2	1.5708 (0)	1.5708 (0)	1.5708 (0)	1.5708 (0)	1.5708 (0)
	3	−6.8715 (−1)	−8.3178 (−1)	−1.0816 (0)	−2.6316 (0)	−5.2428 (0)
	4	2.5525 (−1)	3.6128 (−1)	5.9036 (−1)	3.3393 (0)	1.3157 (1)
	5	−8.2135 (−2)	−1.3399 (−1)	−2.6977 (−1)	−3.4220 (0)	−2.6479 (1)
	6	2.3238 (−2)	4.3419 (−2)	1.0657 (−1)	2.9489 (0)	4.4516 (1)
	7	−5.8551 (−3)	−1.2493 (−2)	−3.7159 (−2)	−2.1971 (0)	−6.4304 (1)
	8	1.3282 (−3)	3.2312 (−3)	1.1608 (−2)	1.4440 (0)	8.1470 (1)
	9	−2.7379 (−4)	−7.5869 (−4)	−3.2857 (−3)	−8.5009 (−1)	−9.1963 (1)
$h=0.2$	n \ ρ	0	0.2	0.5	0.8	1.0
	0	1.0236 (1)	1.0117 (1)	9.4210 (0)	7.6461 (0)	5.3698 (0)
	1	−5.1510 (0)	−5.0914 (0)	−4.7664 (0)	−4.1033 (0)	−3.4555 (0)
	2	1.5708 (0)	1.5708 (0)	1.5708 (0)	1.5708 (0)	1.5708 (0)
	3	−3.6743 (−1)	−3.7767 (−1)	−4.3050 (−1)	−5.2415 (−1)	−6.0468 (−1)
	4	7.0686 (−2)	7.5922 (−2)	1.0341 (−1)	1.5446 (−1)	2.0159 (−1)
	5	−1.1547 (−2)	−1.3161 (−2)	−2.2013 (−2	−4.0116 (−2)	−5.8685 (−2)
	6	1.6360 (−3)	2.0060 (−3)	4.1776 (−3)	9.2316 (−3)	1.5075 (−2)
	7	−2.0430 (−4)	−2.7278 (−4)	−7.1178 (−4)	−1.8991 (−3)	−3.4547 (−3)
	8	2.2788 (−5)	3.3482 (−5)	1.0971 (−4)	3.5247 (−4)	7.1350 (−4)
	9	−2.2952 (−6)	−3.7445 (−6)	−1.5412 (−5)	−5.9523 (−5)	−1.3389 (−4)
	n \ ρ	1.2	1.5	2.0	5.0	10.0
	0	3.2477 (0)	1.7714 (0)	8.9009 (−1)	1.2803 (−1)	3.1561 (−2)
	1	−2.8313 (0)	−2.2021 (0)	−1.6145 (0)	−6.3098 (−1)	−3.1449 (−1)
	2	1.5708 (0)	1.5708 (0)	1.5708 (0)	1.5708 (0)	1.5708 (0)
	3	−6.9432 (−1)	−8.3732 (−1)	−1.0857 (0)	−2.6332 (0)	−5.2436 (0)
	4	2.5918 (−1)	3.6521 (−1)	5.9429 (−1)	3.3432 (0)	1.3161 (1)
	5	−8.3689 (−2)	−1.3586 (−1)	−2.7221 (−1)	−3.4279 (0)	−2.6490 (1)
	6	2.3753 (−2)	4.4146 (−2)	1.0775 (−1)	2.9556 (0)	4.4542 (1)
	7	−6.0032 (−3)	−1.2734 (−2)	−3.7643 (−2)	−2.2032 (0)	−6.4351 (1)
	8	1.3660 (−3)	3.3015 (−3)	1.1780 (−2)	1.4488 (0)	8.1542 (1)
	9	−2.8243 (−4)	−7.7708 (−4)	−3.3402 (−3)	−8.5330 (−1)	−9.2057 (1)

TABLE 2. *Coefficients* $q'_n(\rho,h)$ $[=h^n q_n(\rho,h)]$ *of the* $(\tau/h)^n$ *power series expansion (34) of the unscattered component* $(4\pi/\sigma)I^0(\tau,\rho,h)$ *of the radiation flux, from a circular plane isotropic source, incident on a detector at position* ρ,h *separated from the source-plane by an attenuating layer of thickness* $\tau=\mu t$. *Each term contains the factor* h^n *in order to include meaningful tabulations in the region* $\rho>1, h\approx 0$ *as in (47)*—Continued.

$q_n'(\rho,h)=h^n q_n(\rho,h)$

$h=0.5$	n \ ρ	0	0.2	0.5	0.8	1.0
	0	5.0562 (0)	4.9753 (0)	4.5353 (0)	3.6855 (0)	2.9550 (0)
	1	−3.8832 (0)	−3.8383 (0)	−3.6032 (0)	−3.1826 (0)	−2.8363 (0)
	2	1.5708 (0)	1.5708 (0)	1.5708 (0)	1.5708 (0)	1.5708 (0)
	3	−4.4420 (−1)	−4.5354 (−1)	−5.0155 (−1)	−5.8610 (−1)	−6.5868 (−1)
	4	9.8175 (−2)	1.0341 (−1)	1.3090 (−1)	1.8195 (−1)	2.2907 (−1)
	5	−1.7967 (−2)	−1.9734 (−2)	−2.9378 (−2)	−4.8879 (−2)	−6.6468 (−2)
	6	2.8180 (−3)	3.2613 (−3)	5.8178 (−3)	1.1587 (−2)	1.8090 (−2)
	7	−3.8751 (−4)	−4.7714 (−4)	−1.0318 (−3)	−2.4543 (−3)	−4.2497 (−3)
	8	4.7480 (−5)	6.2749 (−5)	1.6557 (−4)	4.6921 (−4)	8.9969 (−4)
	9	−5.2476 (−6)	−7.5023 (−6)	−2.4234 (−5)	−8.1650 (−5)	−1.7321 (−4)
	n \ ρ	1.2	1.5	2.0	5.0	10.0
	0	2.2550 (0)	1.4874 (0)	8.2602 (−1)	1.2690 (−1)	3.1494 (−2)
	1	−2.4916 (0)	−2.0556 (0)	−1.5625 (0)	−6.2825 (−1)	−3.1416 (−1)
	2	1.5708 (0)	1.5708 (0)	1.5708 (0)	1.5708 (0)	1.5708 (0)
	3	−7.4054 (−1)	−8.7450 (−1)	−1.1135 (0)	−2.6442 (0)	−5.2491 (0)
	4	2.8667 (−1)	3.9270 (−1)	6.2177 (−1)	3.3707 (0)	1.3188 (1)
	5	−9.4997 (−2)	−1.4935 (−1)	−2.8953 (−1)	−3.4095 (0)	−2.6573 (1)
	6	2.7574 (−2)	4.9451 (−2)	1.1626 (−1)	3.0026 (0)	4.4727 (1)
	7	−7.1192 (−3)	−1.4516 (−2)	−4.1153 (−2)	−2.2463 (0)	−6.4683 (1)
	8	1.6543 (−3)	3.8277 (−3)	1.3040 (−2)	1.4823 (0)	8.2044 (1)
	9	−3.4929 (−4)	−9.1603 (−4)	−3.7422 (−3)	−8.7601 (−1)	−9.2716 (1)
$h=1.0$	n \ ρ	0	0.2	0.5	0.8	1.0
	0	2.1776 (0)	2.1463 (0)	1.9878 (0)	1.7219 (0)	1.5118 (0)
	1	−2.6026 (0)	−2.5805 (0)	−2.4687 (0)	−2.2805 (0)	−2.1288 (0)
	2	1.5708 (0)	1.5708 (0)	1.5708 (0)	1.5708 (0)	1.5708 (0)
	3	−6.3824 (−1)	−6.4562 (−1)	−6.8363 (−1)	−7.5100 (−1)	−8.0972 (−1)
	4	1.9635 (−1)	2.0159 (−1)	2.2907 (−1)	2.8013 (0)	3.2725 (−1)
	5	−4.8767 (−2)	−5.0998 (−2)	−6.3027 (−2)	−8.6736 (−2)	−1.1015 (−1)
	6	1.0181 (−2)	1.0886 (−2)	1.4817 (−2)	2.3138 (−2)	3.1998 (−2)
	7	−1.8368 (−3)	−2.0161 (−3)	−3.0566 (−3)	−5.4471 (−3)	−8.2091 (−3)
	8	2.9219 (−4)	3.3053 (−4)	5.6368 (−4)	1.1504 (−3)	1.8895 (−3)
	9	−4.1608 (−5)	−4.8702 (−5)	−9.4190 (−5)	−2.2055 (−4)	−3.9469 (−4)
	n \ ρ	1.2	1.5	2.0	5.0	10.0
	0	1.2993 (0)	1.0123 (0)	6.6582 (−1)	1.2302 (−1)	3.1257 (−2)
	1	−1.9698 (0)	−1.7394 (0)	−1.4173 (0)	−6.1877 (−1)	−3.1298 (−1)
	2	1.5708 (0)	1.5708 (0)	1.5708 (0)	1.5708 (0)	1.5708 (0)
	3	−8.7743 (−1)	−9.9202 (−1)	−1.2063 (0)	−2.6832 (0)	−5.2687 (0)
	4	3.8485 (−1)	4.9087 (−1)	7.1995 (−1)	3.4688 (0)	1.3286 (1)
	5	−1.4065 (−1)	−2.0193 (−1)	−3.5482 (−1)	−3.6193 (0)	−2.6869 (1)
	6	4.4362 (−2)	7.1540 (−2)	1.4981 (−1)	3.1736 (0)	4.5389 (1)
	7	−1.2351 (−2)	−2.2333 (−2)	−5.5516 (−2)	−2.4045 (0)	−6.5876 (1)
	8	3.0830 (−3)	6.2418 (−3)	1.8369 (−2)	1.6064 (0)	8.3854 (1)
	9	−6.9802 (−4)	−1.5806 (−3)	−5.4956 (−3)	−9.6077 (−1)	−9.5095 (1)
$h=2.0$	n \ ρ	0	0.2	0.5	0.8	1.0
	0	7.0103 (−1)	6.9603 (−1)	6.7068 (−1)	6.2738 (−1)	5.9133 (−1)
	1	−1.4833 (0)	−1.4777 (0)	−1.4491 (0)	−1.3995 (0)	−1.3572 (0)
	2	1.5708 (0)	1.5708 (0)	1.5708 (0)	1.5708 (0)	1.5708 (0)
	3	−1.1102 (0)	−1.1148 (0)	−1.1391 (0)	−1.1831 (0)	−1.2226 (0)
	4	5.8905 (−1)	5.9428 (−1)	6.2177 (−1)	6.7282 (−1)	7.1995 (−1)
	5	−2.5030 (−1)	−2.5392 (−1)	−2.7251 (−1)	−3.0818 (−1)	−3.4218 (−1)
	6	8.8721 (−2)	9.0473 (−2)	9.9902 (−2)	1.1843 (−1)	1.3672 (−1)
	7	−2.6983 (−2)	−2.7684 (−2)	−3.1511 (−2)	−3.9278 (−2)	−4.7227 (−2)
	8	7.1878 (−3)	7.4236 (−3)	8.7303 (−3)	1.1475 (−2)	1.4395 (−2)
	9	−1.7037 (−3)	−1.7722 (−3)	−2.1583 (−3)	−2.9996 (−3)	−3.9319 (−3)
	n \ ρ	1.2	1.5	2.0	5.0	10.0
	0	5.5179 (−1)	4.8995 (−1)	3.9168 (−1)	1.0970 (−1)	3.0342 (−2)
	1	−1.3098 (0)	−1.2327 (0)	−1.1012 (0)	−5.8485 (−1)	−3.0839 (−1)
	2	1.5708 (0)	1.5708 (0)	1.5708 (0)	1.5708 (0)	1.5708 (0)
	3	−1.2693 (0)	−1.3517 (0)	−1.5157 (0)	−2.8335 (0)	−5.3464 (0)
	4	7.7754 (−1)	8.8357 (−1)	1.1127 (0)	3.8615 (0)	1.3679 (1)
	5	−3.8510 (−1)	−4.6789 (−1)	−6.6249 (−1)	−4.2401 (0)	−2.8063 (1)
	6	1.6060 (−1)	2.0899 (−1)	3.3307 (−1)	3.9066 (0)	4.8085 (1)
	7	−5.7991 (−2)	−8.0941 (−2)	−1.4532 (−1)	−3.1058 (0)	−7.0780 (1)
	8	1.8501 (−2)	2.7732 (−2)	5.6119 (−2)	2.1742 (0)	9.1364 (1)
	9	−5.2954 (−3)	−8.5329 (−3)	−1.9471 (−2)	−1.3612 (0)	−1.0506 (2)

TABLE 2. *Coefficients* $q'_n(\rho,h)$ $[=h^n q_n(\rho,h)]$ *of the* $(\tau/h)^n$ *power series expansion (34) of the unscattered component* $(4\pi/\sigma)\ I^\circ(\tau,\rho,h)$ *of the radiation flux, from a circular plane isotropic source, incident on a detector at position* ρ,h *separated from the source-plane by an attenuating layer of thickness* $\tau=\mu t$. *Each term contains the factor* h^n *in order to include meaningful tabulations in the regular* $\rho>1, h\approx 0$ *as in (47)*—Continued

$q_n'(\rho,h)=h^n q_n(\rho,h)$

$h=5.0$	n \ ρ	0	0.2	0.5	0.8	1.0
	0	1.2322 (−1)	1.2303 (−1)	1.2206 (−1)	1.2031 (−1)	1.1873 (−1)
	1	−6.2216 (−1)	−6.2168 (−1)	−6.1922 (−1)	−6.1471 (−1)	−6.1063 (−1)
	2	1.5708 (0)	1.5708 (0)	1.5708 (0)	1.5708 (0)	1.5708 (0)
	3	−2.6440 (0)	−2.6461 (0)	−2.6568 (0)	−2.6767 (0)	−2.6949 (0)
	4	3.3379 (0)	3.3432 (0)	3.3707 (0)	3.4217 (0)	3.4688 (0)
	5	−3.3713 (0)	−3.3793 (0)	−3.4215 (0)	−3.5003 (0)	−3.5735 (0)
	6	2.8376 (0)	2.8467 (0)	2.8946 (0)	2.9846 (0)	3.0689 (0)
	7	−2.0473 (0)	−2.0555 (0)	−2.0983 (0)	−2.1820 (0)	−2.2599 (0)
	8	1.2925 (0)	1.2988 (0)	1.3324 (0)	1.3962 (0)	1.4568 (0)
	9	−7.2531 (−1)	−7.2949 (−1)	−7.5174 (−1)	−7.9429 (−1)	−8.3502 (−1)
	n \ ρ	1.2	1.5	2.0	5.0	10.0
	0	1.1686 (−1)	1.1355 (−1)	1.0699 (−1)	6.2828 (−2)	2.5193 (−2)
	1	−6.0574 (−1)	−5.9704 (−1)	−5.7943 (−1)	−4.4372 (−1)	−2.8111 (−1)
	2	1.5708 (0)	1.5708 (0)	1.5708 (0)	1.5708 (0)	1.5708 (0)
	3	−2.7170 (0)	−2.7572 (0)	−2.8422 (0)	−3.7163 (0)	−5.8610 (0)
	4	3.5264 (0)	3.6325 (0)	3.8615 (0)	6.6104 (0)	1.6428 (1)
	5	−3.6636 (0)	−3.8314 (0)	−4.2021 (0)	−9.4298 (0)	−3.6895 (1)
	6	3.1734 (0)	3.3702 (0)	3.8150 (0)	1.1237 (1)	6.9160 (1)
	7	−2.3574 (0)	−2.5430 (0)	−2.9723 (0)	−1.1505 (1)	−1.1130 (2)
	8	1.5331 (0)	1.6802 (0)	2.0286 (0)	1.0332 (1)	1.5695 (2)
	9	−8.8671 (−1)	−9.8760 (−1)	−1.2322 (0)	−8.2664 (0)	−1.9705 (2)
$h=10.0$	n \ ρ	0	0.2	0.5	0.8	1.0
	0	3.1260 (−2)	3.1248 (−2)	3.1183 (−2)	3.1064 (−2)	3.0955 (−2)
	1	−3.1338 (−1)	−3.1332 (−1)	−3.1299 (−1)	−3.1239 (−1)	−3.1184 (−1)
	2	1.5708 (0)	1.5708 (0)	1.5708 (0)	1.5708 (0)	1.5708 (0)
	3	−5.2491 (0)	−5.2501 (0)	−5.2556 (0)	−5.2657 (0)	−5.2750 (0)
	4	1.3155 (1)	1.3161 (1)	1.3188 (1)	1.3239 (1)	1.3286 (1)
	5	−2.6377 (1)	−2.6392 (1)	−2.6475 (1)	−2.6630 (1)	−2.6772 (1)
	6	4.4071 (1)	4.4106 (1)	4.4292 (1)	4.4637 (1)	4.4957 (1)
	7	−6.3116 (1)	−6.3180 (1)	−6.3512 (1)	−6.4133 (1)	−6.4710 (1)
	8	7.9093 (1)	7.9188 (1)	7.9691 (1)	8.0629 (1)	8.1501 (1)
	9	−8.8102 (1)	−8.8226 (1)	−8.8881 (1)	−9.0106 (1)	−9.1247 (1)
	n \ ρ	1.2	1.5	2.0	5.0	10.0
	0	3.0823 (−2)	3.0582 (−2)	3.0074 (−2)	2.5072 (−2)	1.5708 (−2)
	1	−3.1117 (−1)	−3.0995 (−1)	−3.0736 (−1)	−2.8060 (−1)	−2.2207 (−1)
	2	1.5708 (0)	1.5708 (0)	1.5708 (0)	1.5708 (0)	1.5708 (0)
	3	−5.2864 (0)	−5.3073 (0)	−5.3522 (0)	−5.8645 (0)	−7.4117 (0)
	4	1.3344 (1)	1.3450 (1)	1.3679 (1)	1.6428 (1)	2.6245 (1)
	5	−2.6947 (1)	−2.7270 (1)	−2.7971 (1)	−3.6829 (1)	−7.4395 (1)
	6	4.5349 (1)	4.6076 (1)	4.7666 (1)	6.8833 (1)	1.7584 (2)
	7	−6.5419 (1)	−6.6735 (1)	−6.9633 (1)	−1.1031 (2)	−3.5647 (2)
	8	8.2576 (1)	8.4579 (1)	8.9016 (1)	1.5475 (2)	6.3271 (2)
	9	−9.2656 (1)	−9.5289 (1)	−1.0116 (2)	−1.9305 (2)	−9.9885 (2)

TABLE 3. *Unscattered component* $(4\pi/\sigma)I^\circ(\tau,\rho,h)$ *of the radiation flux calculated (a) using table 1 of this work and table 2 of reference [3] (numbers preceded by asterisks) and (b) using table 2 of this work (no asterisks).*

$(4\pi/\sigma)\ I^\circ\ (\tau,\ \rho,\ h)$

$h=0.1$	τ \ ρ	0	0.2	0.5	0.8	1.0	1.2	1.5	2.0	5.0	10.0
	0	1.45 (1)	1.44 (1)	1.36 (1)	1.15 (1)	7.39 (0)	3.60 (0)	1.83 (0)	9.00 (−1)	1.28 (−1)	3.16 (−2)
	0.01	1.39 (1)	1.38 (1)	1.31 (1)	1.10 (1)	7.03 (0)	3.33 (0)	1.62 (0)	7.53 (−1)	7.84 (−2)	1.17 (−2)
	0.02	1.34 (1)	1.33 (1)	1.26 (1)	1.06 (1)	6.71 (0)	3.08 (0)	1.44 (0)	6.31 (−1)	4.81 (−2)	4.31 (−3)
	0.05	1.20 (1)	1.19 (1)	1.13 (1)	9.54 (0)	5.86 (0)	2.47 (0)	1.02 (0)	3.76 (−1)	1.13 (−2)	
	0.1	1.01 (1)	1.00 (1)	9.57 (0)	8.11 (0)	4.81 (0)	1.76 (0)	5.99 (−1)	1.66 (−1)		
		*1.00 (1)	*9.98 (0)	*9.56 (0)	*8.02 (0)	*4.72 (0)	*1.65 (0)				
	0.2	7.38 (0)	7.34 (0)	7.10 (0)	6.12 (0)	3.45 (0)	9.94 (−1)				
		*7.27 (0)	*7.24 (0)	*7.04 (0)	*6.07 (0)	*3.41 (0)	*9.38 (−1)	*2.09 (−1)	*4.56 (−2)	*1.36 (−3)	*1.34 (−4)
	0.5	*3.50 (0)	*3.50 (0)	*3.46 (0)	*3.17 (0)	*1.66 (0)	*2.51 (−1)	*2.74 (−2)	*3.45 (−3)	*2.17 (−5)	*1.72 (−5)
	1.0	*1.38 (0)	*1.38 (0)	*1.38 (0)	*1.32 (0)	*6.63 (−1)	*4.25 (−2)	*1.03 (−3)	*2.49 (−4)		
	2.0	*3.08 (−1)	*3.08 (−1)	*3.08 (−1)	*3.05 (−1)	*1.49 (−1)	*2.11 (−3)				
	5.0	*7.22 (−3)	*7.22 (−3)	*7.21 (−3)	*7.21 (−3)	*3.54 (−3)					
	10.0	*2.61 (−5)	*2.61 (−5)	*2.61 (−5)	*2.61 (−5)	*1.29 (−5)					

TABLE 3. *Unscattered component $(4\pi/\sigma)I^{\circ}(\tau,\rho,h)$ of the radiation flux calculated (a) using table 1 of this work and table 2 of reference [3] (numbers preceded by asterisks) and (b) using table 2 of this work (no asterisks)*—Continued

$(4\pi/\sigma)\ I^{\circ}\ (\tau,\ \rho,\ h)$

h	τ \ ρ	0	0.2	0.5	0.8	1.0	1.2	1.5	2.0	5.0	10.0
0.2	0	1.02 (1)	1.01 (1)	9.42 (0)	7.65 (0)	5.37 (0)	3.25 (0)	1.77 (0)	8.90 (−1)	1.28 (−1)	3.16 (−2)
	0.01	9.98 (0)	9.87 (0)	9.19 (0)	7.44 (0)	5.20 (0)	3.11 (0)	1.67 (0)	8.13 (−1)	1.00 (−1)	1.92 (−2)
	0.02	9.74 (0)	9.62 (0)	8.96 (0)	7.25 (0)	5.04 (0)	2.98 (0)	1.57 (0)	7.43 (−1)	7.83 (−2)	1.17 (−2)
	0.05	9.04 (0)	8.94 (0)	8.32 (0)	6.71 (0)	4.60 (0)	2.63 (0)	1.31 (0)	5.70 (−1)	3.76 (−2)	2.63 (−3)
	0.1	8.01 (0)	7.92 (0)	7.38 (0)	5.93 (0)	3.97 (0)	2.15 (0)	9.78 (−1)	3.70 (−1)	1.12 (−2)	1.01 (−3)
	0.2	6.35 (0)	6.28 (0)	5.88 (0)	4.71 (0)	3.17 (0)	1.49 (0)	5.66 (−1)	1.62 (−1)		
		*6.39 (0)	*6.36 (0)	*5.88 (0)	*4.70 (0)	*3.02 (0)	*1.46 (0)	*5.36 (−1)	*1.38 (−1)	*3.48 (−3)	*3.16 (−4)
	0.5	3.37 (0)	3.35 (0)	3.19 (0)	2.60 (0)	1.55 (0)					
		*3.36 (0)	*3.34 (0)	*3.19 (0)	*2.58 (0)	*1.55 (0)	*5.79 (−1)	*1.37 (−1)	*2.19 (−2)	*1.62 (−4)	*4.90 (−6)
	1.0	*1.37 (0)	*1.37 (0)	*1.34 (0)	*1.14 (0)	*6.35 (−1)	*1.67 (−1)	*1.73 (−2)	*1.02 (−3)		
	2.0	*3.08 (−1)	*3.08 (−1)	*3.06 (−1)	*2.80 (−1)	*1.42 (−1)	*2.06 (−2)	*5.93 (−4)			
	5.0	*7.22 (−3)	*7.22 (−3)	*7.21 (−3)	*7.08 (−3)	*3.48 (−3)	*1.04 (−4)	*7.67 (−7)			
	10.0	*2.61 (−5)	*2.61 (−5)	*2.61 (−5)	*2.61 (−5)	*1.27 (−5)	*2.71 (−8)				
0.5	0	5.06 (0)	4.98 (0)	4.53 (0)	3.69 (0)	2.96 (0)	2.26 (0)	1.49 (0)	8.26 (−1)	1.27 (−1)	3.15 (−2)
	0.01	4.98 (0)	4.90 (0)	4.46 (0)	3.62 (0)	2.90 (0)	2.21 (0)	1.45 (0)	7.95 (−1)	1.15 (−1)	2.58 (−2)
	0.02	4.90 (0)	4.82 (0)	4.39 (0)	3.56 (0)	2.84 (0)	2.16 (0)	1.41 (0)	7.66 (−1)	1.04 (−1)	2.11 (−2)
	0.05	4.68 (0)	4.61 (0)	4.19 (0)	3.38 (0)	2.69 (0)	2.02 (0)	1.30 (0)	6.84 (−1)	7.74 (−2)	1.16 (−2)
	0.1	4.34 (0)	4.27 (0)	3.87 (0)	3.11 (0)	2.45 (0)	1.81 (0)	1.13 (0)	5.68 (−1)	4.74 (−2)	4.30 (−3)
	0.2	3.73 (0)	3.66 (0)	3.32 (0)	2.63 (0)	2.03 (0)	1.47 (0)	8.69 (−1)	3.94 (−1)	1.79 (−2)	
	0.5	2.38 (0)	2.34 (0)	2.11 (0)	1.63 (0)	1.21 (0)	8.07 (−1)	4.09 (−1)	1.38 (−1)		
		*2.38 (0)	*2.34 (0)	*2.11 (0)	*1.63 (0)	*1.21 (0)	*8.07 (−1)	*4.08 (−1)	*1.36 (−1)	*1.72 (−3)	6.69 (−5)
	1.0	1.16 (0)	1.14 (0)	1.03 (0)	7.78 (−1)	5.43 (−1)	3.26 (−1)				
		*1.16 (0)	*1.14 (0)	*1.03 (0)	*7.77 (−1)	*5.43 (−1)	*3.26 (−1)	*1.30 (−1)	*2.73 (−2)	*1.87 (−5)	
	2.0	*2.93 (−1)	*2.90 (−1)	*2.69 (−1)	*2.03 (−1)	*1.32 (−1)	*6.64 (−2)	*1.73 (−2)	*1.62 (−3)		
	5.0	*7.21 (−3)	*7.20 (−3)	*7.04 (−3)	*5.76 (−3)	*3.29 (−3)	*1.09 (−3)	*9.00 (−5)	*6.03 (−7)		
	10.0	*2.61 (−5)	*2.61 (−5)	*2.61 (−5)	*2.31 (−5)	*1.22 (−5)	*2.29 (−6)	*2.52 (−8)			
1.0	0	2.18 (0)	2.15 (0)	1.99 (0)	1.72 (0)	1.51 (0)	1.30 (0)	1.01 (0)	6.66 (−1)	1.23 (−1)	3.13 (−2)
	0.01	2.15 (0)	2.12 (0)	1.96 (0)	1.70 (0)	1.49 (0)	1.26 (0)	9.95 (−1)	6.52 (−1)	1.17 (−1)	2.83 (−2)
	0.02	2.13 (0)	2.10 (0)	1.94 (0)	1.68 (0)	1.47 (0)	1.20 (0)	9.78 (−1)	6.38 (−1)	1.11 (−1)	2.56 (−2)
	0.05	2.05 (0)	2.02 (0)	1.87 (0)	1.61 (0)	1.41 (0)	1.20 (0)	9.29 (−1)	5.99 (−1)	9.57 (−2)	1.90 (−2)
	0.1	1.93 (0)	1.90 (0)	1.76 (0)	1.51 (0)	1.31 (0)	1.12 (0)	8.53 (−1)	5.39 (−1)	7.45 (−2)	1.15 (−2)
	0.2	1.71 (0)	1.69 (0)	1.55 (0)	1.32 (0)	1.14 (0)	9.62 (−1)	7.20 (−1)	4.37 (−1)	4.52 (−2)	4.24 (−3)
	0.5	1.20 (0)	1.18 (0)	1.07 (0)	8.96 (−1)	7.56 (−1)	6.18 (−1)	4.37 (−1)	2.35 (−1)	1.02 (−2)	
		*1.21 (0)	*1.18 (0)	*1.07 (0)	*8.94 (−1)	*7.55 (−1)	*6.17 (−1)	*4.37 (−1)	*2.42 (−1)	*9.31 (−3)	*3.96 (−4)
	1.0	6.64 (−1)	6.51 (−1)	5.85 (−1)	4.73 (−1)	3.87 (−1)	3.02 (−1)	1.95 (−1)	8.65 (−2)		
		*6.64 (−1)	*6.51 (−1)	*5.84 (−1)	*4.73 (−1)	*3.87 (−1)	*3.04 (−1)	*1.95 (−1)	*8.65 (−2)	*1.06 (−3)	*2.27 (−6)
	2.0	2.05 (−1)	2.01 (−1)	1.77 (−1)	1.37 (−1)						
		*2.06 (−1)	*2.01 (−1)	*1.77 (−1)	*1.38 (−1)	*1.06 (−1)	*7.67 (−2)	*4.22 (−2)	*1.29 (−2)	*6.65 (−6)	
	5.0	*6.54 (−3)	*6.42 (−3)	*5.70 (−3)	*4.21 (−3)	*2.95 (−3)	*1.79 (−3)	*6.51 (−4)	*7.40 (−5)		
	10.0	*2.58 (−5)	*2.56 (−5)	*2.41 (−5)	*1.78 (−5)	*1.14 (−5)	*5.57 (−6)	*1.13 (−6)	*2.66 (−8)		
2.0	0	7.01 (−1)	6.96 (−1)	6.71 (−1)	6.27 (−1)	5.91 (−1)	5.52 (−1)	4.90 (−1)	3.92 (−1)	1.10 (−1)	3.03 (−2)
	0.01	6.94 (−1)	6.89 (−1)	6.63 (−1)	6.20 (−1)	5.85 (−1)	5.45 (−1)	4.84 (−1)	3.86 (−1)	1.07 (−1)	2.88 (−2)
	0.02	6.86 (−1)	6.81 (−1)	6.56 (−1)	6.14 (−1)	5.78 (−1)	5.39 (−1)	4.78 (−1)	3.81 (−1)	1.04 (−1)	2.74 (−2)
	0.05	6.65 (−1)	6.60 (−1)	6.35 (−1)	5.93 (−1)	5.58 (−1)	5.20 (−1)	4.60 (−1)	3.65 (−1)	9.60 (−2)	2.35 (−2)
	0.1	6.31 (−1)	6.26 (−1)	6.02 (−1)	5.61 (−1)	5.27 (−1)	4.90 (−1)	4.32 (−1)	3.40 (−1)	8.40 (−2)	1.83 (−2)
	0.2	5.67 (−1)	5.63 (−1)	5.40 (−1)	5.02 (−1)	4.70 (−1)	4.35 (−1)	3.81 (−1)	2.96 (−1)	6.44 (−2)	1.10 (−2)
	0.5	4.13 (−1)	4.09 (−1)	3.91 (−1)	3.60 (−1)	3.34 (−1)	3.05 (−1)	2.62 (−1)	1.95 (−1)	2.91 (−2)	2.41 (−3)
		*4.14 (−1)	*4.10 (−1)	*3.90 (−1)	*3.59 (−1)	*3.34 (−1)	*3.07 (−1)	*2.62 (−1)	*1.95 (−1)	*3.00 (−2)	*2.18 (−3)
	1.0	2.44 (−1)	2.41 (−1)	2.28 (−1)	2.06 (−1)	1.89 (−1)	1.70 (−1)	1.41 (−1)	9.74 (−2)	7.83 (−3)	
		*2.43 (−1)	*2.41 (−1)	*2.28 (−1)	*2.07 (−1)	*1.89 (−1)	*1.70 (−1)	*1.40 (−1)	*9.74 (−2)	*7.69 (−3)	*2.35 (−4)
	2.0	8.47 (−2)	8.36 (−2)	7.79 (−2)	6.85 (−2)	6.09 (−2)	5.29 (−2)	4.12 (−2)			
		*8.44 (−2)	*8.33 (−2)	*7.79 (−2)	*6.85 (−2)	*6.09 (−2)	*5.29 (−2)	*4.12 (−2)	*2.50 (−2)	*6.16 (−4)	
	5.0	*3.59 (−3)	*3.52 (−3)	*3.17 (−3)	*2.60 (−3)	*2.16 (−3)	*1.72 (−3)	*1.14 (−3)	*4.77 (−4)	*2.28 (−7)	
	10.0	*1.89 (−5)	*1.84 (−5)	*1.61 (−5)	*1.24 (−5)	*9.55 (−6)	*6.86 (−6)	*3.45 (−6)	*9.02 (−7)		

TABLE 3. *Unscattered component* $(4\pi/\sigma)I^{\circ}(\tau,\rho,h)$ *of the radiation flux calculated (a) using table 1 of this work and table 2 of reference [3] (numbers preceded by asterisks) and (b) using table 2 of this work (no asterisks)*—Continued

$(4\pi/\sigma)\ I^{\circ}(\rho, h, \tau)$

h=5.0	τ \ ρ	0	0.2	0.5	0.8	1.0	1.2	1.5	2.0	5.0	10.0
	0	1.23 (−1)	1.23 (−1)	1.22 (−1)	1.20 (−1)	1.19 (−1)	1.17 (−1)	1.14 (−1)	1.07 (−1)	6.28 (−2)	2.52 (−2)
	0.01	1.22 (−1)	1.22 (−1)	1.21 (−1)	1.19 (−1)	1.18 (−1)	1.16 (−1)	1.12 (−1)	1.06 (−1)	6.27 (−2)	2.51 (−2)
	0.02	1.21 (−1)	1.21 (−1)	1.20 (−1)	1.18 (−1)	1.16 (−1)	1.14 (−1)	1.11 (−1)	1.05 (−1)	6.11 (−2)	2.41 (−2)
	0.05	1.17 (−1)	1.17 (−1)	1.16 (−1)	1.14 (−1)	1.13 (−1)	1.11 (−1)	1.08 (−1)	1.01 (−1)	5.85 (−2)	2.25 (−2)
	0.1	1.11 (−1)	1.11 (−1)	1.10 (−1)	1.09 (−1)	1.07 (−1)	1.05 (−1)	1.02 (−1)	9.60 (−2)	5.46 (−2)	2.02 (−2)
	0.2	1.01 (−1)	1.01 (−1)	9.96 (−2)	9.81 (−2)	9.66 (−2)	9.50 (−2)	9.20 (−2)	8.62 (−2)	4.74 (−2)	1.61 (−2)
	0.5	7.44 (−2)	7.43 (−2)	7.35 (−2)	7.22 (−2)	7.10 (−2)	6.96 (−2)	6.71 (−2)	6.23 (−2)	3.10 (−2)	8.26 (−3)
		*7.24 (−2)	*7.24 (−2)	*7.24 (−2)	*7.20 (−2)	*7.14 (−2)	*7.03 (−2)	*6.80 (−2)	*6.24 (−2)	*3.14 (−2)	*8.50 (−3)
	1.0	4.49 (−2)	4.48 (−2)	4.43 (−2)	4.33 (−2)	4.25 (−2)	4.14 (−2)	3.97 (−2)	3.62 (−2)	1.53 (−2)	2.71 (−3)
		*4.50 (−2)	*4.49 (−2)	*4.44 (−2)	*4.33 (−2)	*4.25 (−2)	*4.14 (−2)	*3.96 (−2)	*3.62 (−2)	*1.53 (−2)	*2.72 (−3)
	2.0	1.64 (−2)	1.63 (−2)	1.60 (−2)	1.56 (−2)	1.52 (−2)	1.47 (−2)	1.39 (−2)	1.23 (−2)	3.76 (−3)	
		*1.66 (−2)	*1.66 (−2)	*1.62 (−2)	*1.57 (−2)	*1.52 (−2)	*1.47 (−2)	*1.38 (−2)	*1.22 (−2)	*3.77 (−3)	*2.94 (−4)
	5.0	*7.91 (−4)	*7.87 (−4)	*7.66 (−4)	*7.29 (−4)	*6.97 (−4)	*6.60 (−4)	*5.97 (−4)	*4.83 (−4)	*5.71 (−5)	*3.77 (−7)
	10.0	*5.09 (−6)	*5.05 (−6)	*4.83 (−6)	*4.45 (−6)	*4.13 (−6)	*3.78 (−6)	*3.20 (−6)	*2.27 (−6)	*5.99 (−8)	

h=10.0	τ \ ρ	0	0.2	0.5	0.8	1.0	1.2	1.5	2.0	5.0	10.0
	0	3.13 (−2)	3.12 (−2)	3.12 (−2)	3.11 (−2)	3.10 (−2)	3.08 (−2)	3.06 (−2)	3.01 (−2)	2.51 (−2)	1.57 (−2)
	0.01	3.09 (−2)	3.09 (−2)	3.09 (−2)	3.08 (−2)	3.06 (−2)	3.05 (−2)	3.03 (−2)	2.98 (−2)	2.48 (−2)	1.55 (−2)
	0.02	3.06 (−2)	3.06 (−2)	3.06 (−2)	3.04 (−2)	3.03 (−2)	3.02 (−2)	3.00 (−2)	2.95 (−2)	2.45 (−2)	1.53 (−2)
	0.05	2.97 (−2)	2.97 (−2)	2.97 (−2)	2.95 (−2)	2.94 (−2)	2.93 (−2)	2.91 (−2)	2.86 (−2)	2.37 (−2)	1.46 (−2)
	0.1	2.83 (−2)	2.83 (−2)	2.82 (−2)	2.81 (−2)	2.80 (−2)	2.79 (−2)	2.76 (−2)	2.72 (−2)	2.24 (−2)	1.36 (−2)
	0.2	2.56 (−2)	2.56 (−2)	2.55 (−2)	2.54 (−2)	2.53 (−2)	2.52 (−2)	2.50 (−2)	2.45 (−2)	2.00 (−2)	1.18 (−2)
	0.5	1.89 (−2)	1.89 (−2)	1.89 (−2)	1.88 (−2)	1.87 (−2)	1.86 (−2)	1.84 (−2)	1.80 (−2)	1.43 (−2)	7.75 (−3)
		*1.76 (−2)	*1.76 (−2)	*1.77 (−2)	*1.79 (−2)	*1.80 (−2)	*1.81 (−2)	*1.82 (−2)	*1.83 (−2)	*1.40 (−2)	*7.86 (−3)
	1.0	1.15 (−2)	1.15 (−2)	1.14 (−2)	1.14 (−2)	1.13 (−2)	1.12 (−2)	1.11 (−2)	1.08 (−2)	8.20 (−3)	3.82 (−3)
		*1.15 (−2)	*1.15 (−2)	*1.15 (−2)	*1.14 (−2)	*1.13 (−2)	*1.13 (−2)	*1.11 (−2)	*1.08 (−2)	*8.20 (−3)	*3.80 (−3)
	2.0	4.21 (−3)	4.21 (−3)	4.19 (−3)	4.16 (−3)	4.13 (−3)	4.09 (−3)	4.03 (−3)	3.90 (−3)	2.68 (−3)	9.31 (−4)
		*4.33 (−3)	*4.32 (−3)	*4.30 (−3)	*4.25 (−3)	*4.21 (−3)	*4.16 (−3)	*4.08 (−3)	*3.91 (−3)	*2.67 (−3)	*9.33 (−4)
	5.0	*2.08 (−4)	*2.08 (−4)	*2.06 (−4)	*2.04 (−4)	*2.04 (−4)	*2.01 (−4)	*1.93 (−4)	*1.82 (−4)	*9.37 (−5)	*1.36 (−5)
	10.0	*1.39 (−6)	*1.38 (−6)	*1.37 (−6)	*1.34 (−6)	*1.31 (−6)	*1.28 (−6)	*1.22 (−6)	*1.10 (−6)	*3.53 (−7)	*1.26 (−8)

TABLE 4. *Comparison of convergence in calculating the unscattered component* $(4\pi/\sigma)I^{\circ}(\tau,\rho,h)$ *in the case* $\tau=\mu l=1$, *for the three situations (A), (B), and (C) indicated in figure 3. For each situation the first column contains partial sums*

$$\sum_{l=0}^{L}(l+\tfrac{1}{2})g_l(\tau)\,p_l(\rho,h)$$

and the second column contains sums

$$\sum_{n=0}^{N}q_n(\rho,h)\tau^n.$$

L,N	(A): ρ=0.5, h=0.5		(B): ρ=1, h=1		(C): ρ=2, h=1	
	Legendre sum	τ^n-series sum	Legendre sum	τ^n series sum	Legendre sum	τ^n-series sum
0	0.34031	4.5353	0.12316	1.5118	0.035740	0.66582
1	.84669	−2.6711	.31658	−0.6170	.072679	−0.75149
2	.99567	3.6122	.38273	0.9538	.068353	0.81932
3	.99211	−0.4003	.37916	.1441	.071785	−0.38701
4	1.01738	1.6941	.38475	.4713	.081105	0.33294
5	1.02484	0.7540	.38774	.3612	.079699	−0.02187
6	1.02365	1.1264	.38665	.3932	.082707	0.12793
7	1.02628	0.9943	.38793	.3850	.084872	.07242
8	1.02590	1.0367	.38753	.3869	.084935	.09079
9	1.02615	1.0243	.38718	.3865	.086201	.08529
10	1.02619	1.0276	.38727	.3865	.086348	.08679
11	1.02655	1.0268	.38688	.3865	.086408	.08641
12	1.02677	1.0270	.38685	.3865	.086602	.08650
13	1.02685	1.0269	.38672	.3865	.086496	.08648

A physical interpretation of the rather wild oscillations in the first few terms of the τ^n series is that the zeroth term would be the result for a bare disk source ($\tau=0$), from which the radiation absorbed in the barrier of thickness τ must be subtracted. This subtraction is accomplished by a succession of undershoots and overshoots which are quickly damped out if τ is small enough.

3.4. $h\approx 0$, $\rho>1$: Power Series Solution In or Near Plane of Disk

If both source and detector are embedded in a homogeneous attenuating medium, the series (34) is valid except for $h=0$, where the concept of "barrier thickness" τ becomes meaningless. As $h\to 0$, $q_n\to\infty$ as $1/h^n$, but at the same time $\tau^n\to 0$ as h^n, while $q_0(\rho,0)$ is a finite but indeterminate quantity of the form $\{\infty-\infty\}$.

The series (34) can still be used if the indeterminacy is removed from the product $q_n\tau^n$ by multiplying and dividing q_n and τ^n, respectively, by h^n, resulting in a series of the form

$$I^{\circ}(\tau,\rho,h)=(\sigma/4\pi)\sum_{n=0}^{\infty}q'_n(\rho,h)(\mu\cdot 1)^n, \qquad (47)$$

in which $q'_n(\rho,h)=h^n q_n(\rho,h)$ and $\mu\cdot 1=\tau/h=\mu t/h=\mu h/h=$the radius of the disk source measured in mean-free-paths of the attenuating medium, and $q'_0(\rho,h)=q_0(\rho,h)$.

For $h=0$, $\rho>1$ the expression in (37) reduces to

$$q_0(\rho,0)=\ln\left(\frac{\rho^2}{\rho^2-1}\right). \tag{48}$$

4. Buildup Factor

When both source and detector are embedded in a homogeneous medium, the secondary, or scattered radiation contribution I^s is often taken into account by means of a buildup factor [6]

$$B(\mu r)=(I^o+I^s)/I^o.$$

Such a buildup factor may then be used to evaluate the total flux I from a point isotropic source according to

$$I=I^o+I^s=I^oB(\mu r)=(\sigma/4\pi)B(\mu r)\exp(-\mu r)/r^2. \tag{49}$$

In references [8] and [9] $B(\mu r)$ is expressed as a set of polynomial coefficients β_i, in the notation of reference [9], as defined in equation (2), with $N=3$.

Now, since the integration of (33) was performed term by term over the expansion

$$\exp(-\tau/\cos\theta)=\exp(-\mu r)=\sum_{n=0}^{\infty}(-1)^n(\mu r)^n/n!, \tag{50}$$

no new integrands appear if these series terms are multiplied by terms $\beta_i(\mu r)^i$ of the polynomial representation of $B(\mu r)$. If this multiplication is performed, the total radiation flux as defined in (49) may be written as the series

$$I=I^o+I^s=(\sigma/4\pi)\sum_{n=0}^{\infty}\beta'_n q_n\tau^n, \tag{51}$$

in which $\tau=\mu h$. The modified buildup coefficients β'_n are generated from β_i's, such as are given in [8] or [9], as

$$\beta'_n=\sum_{i=0}^{N}(-1)^i\{n!/(n-i)!\}\beta_i \tag{52}$$

in which $n!/(n-i)!=0$ for $i>n$. For $N=3$ the

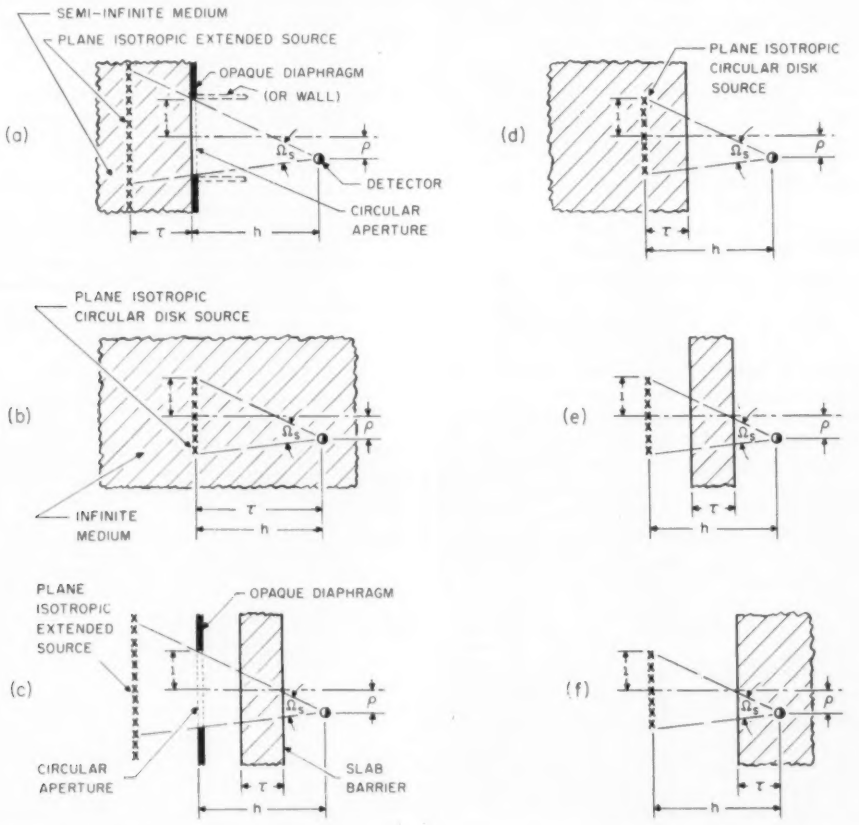

FIGURE 5. *Some circular aperture or disk source situations to which results are applicable. (a): I^o+I^s calculable using $p_i(p,h)$, $q_i(\tau)$ coefficients. (b): I^o+I^s calculable using β'_i,$q_i(\rho,h)$ coefficients. (a–f): I^o calculable using either $p_i(\rho,h)$ and $g_i{}^o$, or $q_i(\rho,h)$ coefficients.*

first five modified buildup coefficients are

$$\left.\begin{aligned}
&\beta_0'=\beta_0\simeq 1\\
&\beta_1'=\beta_0-\beta_1\\
&\beta_2'=\beta_0-2\beta_1+2\cdot 1\beta_2\\
&\beta_3'=\beta_0-3\beta_1+3\cdot 2\beta_2-3\cdot 2\cdot 1\beta_3\\
\text{and}\\
&\beta_4'=\beta_0-4\beta_1+4\cdot 3\beta_2-4\cdot 3\cdot 2\beta_3.
\end{aligned}\right\} \qquad (53)$$

Such a set of β_n' coefficients, once generated, may be applied as in (51) to either the disk-source $q_n(\rho,h)$'s in table 3 of this work or the rectangular source $q_n(a,b)$'s in table 3 of reference [3].

5. Discussion

Situations to which results in this paper may be applied are schematized in figure 5.

The Legendre method of section 2 can be used to calculate $I=I^o+I^s$ in such cases as figure 5a in which the source is distributed in a uniform layer (or layers) parallel to the exit surface of the medium. If g_l angular harmonic coefficients are used which have been calculated assuming an infinite medium, the result will be an overestimate because of the depression, in the realistic case, of flux near a boundary. This flux depression results from the one-way nature of the radiation traversal across the boundary. For gamma rays the infinite medium g_l's may be a rather good approximation, whereas for neutrons more realistic g_l's including the boundary effect may have to be used.

The unscattered component I^o may in principle be calculated for all situations in figure 5a–f using either the Legendre $p_l(\rho,h)$'s of section 2 or the $q_n(\rho,h)$'s of section 3, but in practice the Legendre series (6) converges better for barriers of the order of one mean free path or thicker while the $q_n(\rho,h)$ series (34) converges better for barriers of less than a mean free path.

Adaptation of polynomial representations of point isotropic source buildup factors, as suggested in section 4 for use with the $q_n(\rho,h)$'s of section 3 for computation of $I=I^o+I^s$, is strictly valid only for the situation in figure 5b, although some qualitative results may be obtained in the other situations depending on how little the physical situation departs from figure 5b.

The authors thank M. J. Berger and L. V. Spencer for their interest, encouragement and helpful criticisms regarding this effort. The authors are also indebted to A. B. Chilton, E. W. Emery, D. C. Kleinecke, J. H. Smith, and M. L. Storm for their reviews of the manuscript and suggestions towards clarity and accuracy of presentation.

6. References

[1] For an excellent review of this literature, see A. I. Mahan and W. F. Malmborg, Radiation characteristics of semicircular, circular and rectangular surface sources, J. Opt. Soc. Am. **44,** 644 (1954).

[2] J. H. Smith and M. L. Storm, Generalized off-axis distributions from disk sources of radiation, J. Appl. Phys. **25,** 519 (1954).

[3] J. H. Hubbell, R. L. Bach, and J. C. Lamkin, Radiation field from a rectangular source, J. Research NBS **64C,** 121 (1960).

[4] M. J. Berger and J. C. Lamkin, Sample calculations of gamma-ray penetration into shelters: Contributions of sky shine and roof contamination, J. Research NBS **60,** 109 (1958) RP2827.

[5] L. V. Spencer, Structure shielding against fallout radiation from nuclear weapons (to be published as an NBS Monograph).

[6] U. Fano. L. V. Spencer, and M. J. Berger, Penetration and diffusion of X-rays, Encyclopedia of physics (Springer-Verlag **38** II, 1959).

[7] I. G. Weinberg and E. R. Cohen, Neutron-flux distribution from a thermal column face, Nucleonics **13,** No. 7, 25 (1955).

[8] J. H. Hubbell, Dose due to distributed gamma-ray sources (unpublished).

[9] M. A. Capo, Polynomial approximation of gamma ray buildup factors for a point isotropic source, APEX–510, Nov. 1958.

[10] A. H. Jaffey, Solid angle subtended by a circular aperture at point and spread sources: Formulas and some tables, Rev. Sci. Instr. **25,** 349 (1954).

[11] A. V. H. Masket, R. L. Macklin, and H. W. Schmitt, Tables of solid angles and activations, ORNL–2170 (Nov. 1956).

[12] L. F. Epstein and J. H. Hubbell, Evaluation of a generalized elliptic-type integral (to be published).

[13] A. Fletcher, Guide to tables of elliptic functions, Mathematical tables and other aids to computation, **3,** 229 (1948–49).

[14] C. Hastings, Jr., Approximations for digital computers (Princeton Univ. Press, 1955).

[15] W. Gröbner and N. Hofreiter, Integraltafel II, Bestimmte Integrale (Springer-Verlag, 1958); see esp. eq 332.38a.

[16] Although identifiable with a result of R. A. Herman, A treatise on geometrical optics (Cambridge Univ. Press, London, 1900), p. 217, ex. 13, the form of the result in (29) seems to have first been published by P. D. Foote, Bull. NBS **12,** 583 (1915).

[17] G. Placzek, The functions $E_n(x)=\int_1^\infty e^{-xu}u^{-n}du$, MT–1, NRC No. 1547, Chalk River, Ont. (1946).

[18] R. M. Sievert, Die Intensitätsverteilung der primären γ-Strahlung in der Nähe medizinischer Radiumpräparate, Acta Radiol. (Stockholm) **1,** 89 (1921).

[19] See, for example, H. B. Dwight, Tables of integrals and other mathematical data, 3d ed., p. 2, eq 5.3–5.5 (McGraw-Hill, N.Y., 1957).

[20] See, for example, Nuclear engineering handbook, H. Etherington, ed.: Ch. 7.3, Nuclear radiation shielding, E. P. Blizard, p. 7–104 (McGraw-Hill, N.Y., 1958).

[21] E. Fermi, Sul moto dei neutroni nelle sostanze idrogenate, Ricerca Sci. **7,** part 2, 13 (1936)

[22] G. Placzek, The angular distribution of neutrons emerging from a plane surface, Phys. Rev. **72,** 556 (1947).

(Paper 65C4–78)

JOURNAL OF RESEARCH of the National Bureau of Standards—C. Engineering and Instrumentation
Vol. 65C, No. 4, October–December 1961

The Bauschinger Effect and Residual Microstresses in Alpha Brass

Clarence J. Newton

(July 5, 1961)

The Bauschinger effect in alpha brass, specifically the lowering of the yield strength in the direction opposite to the preceding plastic deformation, was studied by an examination of both tensile and compressive elastic limits measured at the quarter-cycle stages throughout a complete cycle of uniaxial plastic strain of one percent amplitude. X-ray measurements of axial residual directed microstresses indicated that the latter could be correlated with the decrease of the elastic limit measured in the direction opposite to the preceding deformation only at the first quarter-cycle of deformation. After 3 quarter-cycles the axial residual stress was always tensile regardless of the direction of previous deformation; whereas the elastic limits continue to show strong directionality.

1. Introduction

Although it is nearly 80 years since Bauschinger [1][1] first reported the effect which may be described very broadly as the anisotropic modification of the plastic properties of a metal specimen that has undergone a preceding plastic deformation, a simple quantitative explanation for the phenomenon has not yet been established. Perhaps the most common aspect of this effect is the raising of the yield strength of a plastically deformed metallic specimen in the direction of previous deformation and the lowering of the yield strength in the opposite or reverse direction. The basis of an explanation often advanced for this phenomenon is the difference in degree of susceptibility to slip in differently oriented crystal grains or regions of differing hardness within the specimen [2]. This inhomogeniety of slip is thought to give rise to a system of residual internal stresses upon release of the deforming load; and, upon reapplication of load, these residual stresses presumably modify the external stress required for yielding.

Residual stresses in metals can be calculated from measurements obtained by means of X-ray diffraction [3]. If the stresses are random in sign and magnitude in the diffracting material, the X-ray diffraction lines are observed to be broadened; if the stresses are nonrandom, the peak of the line will be shifted. This latter effect, the change in Bragg angle of diffraction after plastic deformation of a specimen, implies a nonzero net stress in the diffracting material, which is usually observed to be of such a sign as to oppose the prior deformation. S. L. Smith and W. A. Wood [4] observed such residual stresses by means of X-rays and believed them to be related to the Bauschinger effect.

Recently a detailed quantitative study was made of this type of residual "oriented microstress" and its relation to the Bauschinger effect by B. M. Rovinskiy and V. M. Sinayskiy [5]. These experimenters worked with three groups of specimens of 40X steel (Russian designation), each group having had a different thermal or strain-rate history. The specimens, after having been annealed, were compressed uniaxially by different amounts, ranging from 0.30 percent to 1.46 percent. Although the authors do not give details of their X-ray procedures, they state that back-reflection X-ray patterns of the (310) spacing (using cobalt radiation) after these prestrains enabled them to calculate the residual microstress, σ_R, in each case. The direction of σ_R is not specified, but it is presumed to be axial. The conventional 0.2 percent yield strengths in compression and in tension were then determined, and the difference, $\Delta\sigma$, between them was obtained for each degree of prestrain. Both the yield strength difference and the residual stress were found to go through a maximum at a deformation near 1 percent. The value of prestrain that resulted in these simultaneous maximums near 1 percent depended on the thermal and strain-rate history of the specimen. The ratio of σ_R to $\Delta\sigma$ was found to differ from one group of specimens to another, but to vary by only a few percent within a group. These authors observed that this ratio, in most cases somewhat greater than unity, was comparable to that observed for the ratio of the X-ray stress, measured on a specimen under load, to the applied mechanical stress. They concluded that, if one keeps in mind the coefficient of correspondence between stresses determined by X-ray and mechanical methods, one can predict the magnitude of the reduction of the yield strength during reversed loading of a specimen from the size of the residual oriented microstress observed with X-rays. Thus the Bauschinger effect after uniaxial plastic deformation is, according to this picture, the result of the establishment of a residual oriented microstress that can be summed with the macrostress created by the external load. Or, in equation form,

$$\sigma_A = \sigma_0 + \alpha\sigma_R,$$

where σ_A is the yield strength of the annealed mate-

[1] Figures in brackets indicate the literature references at the end of this paper.

rial, σ_0 is the yield strength observed in the reverse direction after a plastic deformation of the specimen, α is constant nearly equal to unity, and σ_R is the oriented axial residual microstress measured by X-ray diffraction. Or, from another viewpoint, the reduction of the yield strength is

$$\Delta\sigma = \sigma_A - \sigma_0 = \alpha\sigma_R.$$

Since the residual stresses in a specimen are balanced internally by stresses of the opposite sign, there is a further corollary implicit in this model, that is, that the region or crystals that support the additive stress observed by means of X-rays is that same region in which plastic flow first begins, thus determining the yield strength.

This article on the Bauschinger effect by Rovinskiy and Sinayskiy was of sufficient interest that it was decided to investigate the Bauschinger effect and the state of residual stress at appropriate stages in specimens that had undergone a complete cycle of plastic deformation, unlike those of Rovinskiy and Sinayskiy, which had been plastically deformed in one direction only.

2. Experimental Material, Procedure, and Results

When a metal specimen containing a residual internal stress system is sectioned, it is assumed that at the exposed surface the stress component normal to the surface vanishes and the components of stress parallel to the surface are not affected. A few years ago an X-ray study of residual stresses on various sections of plastically deformed iron by C. J. Newton and H. C. Vacher [7] yielded results consistent with this long-held hypothesis. The procedure in that study employed an X-ray beam normally incident on the sections of the specimen with the diffraction pattern recorded on photographic film. The observed lattice spacing was compared with that of the annealed material. A similar procedure was used in this study of sections of alpha brass specimens, except that the diffracted X-rays were detected by means of a diffractometer (counter) technique instead of by film.

The alpha (Cu=70, Zn=30, Pb<0.07 percent) brass specimens which served both for elastic limit measurement and for X-ray residual stress measurements, were machined from 1 by ⅜ in. bars, to be 7½ in. long with a gage length of 1¼ in. and a reduced section measuring 0.625 by 0.373 in. X-ray examination indicated no appreciable preferred orientation in the material. The plastic extension was performed on a hydraulic testing machine using Templin grips, the plastic compression was made possible by careful machining of the ends of the specimens and by the use of massive steel guides around the specimen undergoing compression. During the course of interrupted straining, resistance wire strain gages were used to follow the amount of strain. The routine of the mechanical testing and strain measurements, along with a discussion of the difficulties that sometimes arise when one attempts to measure very small permanent sets, and hence elastic limits, with resistance gages, has been previously reported [8]. The elastic limit was taken to be the stress required to give the specimen a permanent set of 2×10^{-5}, as indicated by gages not previously subjected to large plastic strains.

The values of the limit for various conditions of the brass specimens are listed in table 1. It is difficult to specify precisely the reliability of these values, most of which are the average of several observations. The precision of the testing machine is high, but variations from one specimen to another may be large. A reasonable estimate of average uncertainty might be about $\pm1\times10^3$ psi.

TABLE 1. *Elastic limits and oriented residual stresses*

Plastic deformation state of specimen			Elastic limits in 10^3 psi		Axial residual stress in 10^3 psi
Description	Net plastic prestrain (%)	Cum. plastic prestrain (%)	In tension	In compression	
Annealed	0	0	14	13	(Reference zero).
Positive cycle (initial deformation extension)					
E	+1	1	15	3	−9
E-C	0	2	4	16	+2
E-C-C-	−1	3	5	20	+5
E-C-C-E	0	4	20	3	+7
Negative cycle (initial deformation compression)					
C	−1	1	4	16	+8
C-E	0	2	17	3	−3
C-E-E-	+1	3	.....	.....	+4
C-E-E-C	0	4	.....	.....	+8

E=Extended plastically 1%.
C=Compressed plastically 1%.
Average uncertainty approximately $\pm1\times10^3$ psi.
Different specimens were used for the X-ray residual stress measurements (last column) than were used for the elastic limit determinations.

One can see in table 1 that essentially symmetrical results of elastic limits with respect to plastic extension or compression were obtained when the directions of limit determination and prestrain are taken into account. The effect of plastic deformation was to raise slightly the elastic limit measured in the same direction as the deformation and to lower by a large amount the limit measured in the opposite direction; this is in accord with the Bauschinger effect. When a second plastic deformation, reversed in direction, was made, the elastic limits were affected by roughly the same amounts relative to the values pertaining to the original material in the annealed state, but reversed in direction. This demonstrated that it is the direction of the immediately preceding deformation that is of major importance with regard to the elastic limits. The third step in the positive cycle of plastic deformation, at a minus 1 percent net strain, showed a small increase in both tensile and compressive elastic limits. And finally, the last step of the cycle, an extension of 1 percent to reverse the net strain to zero, resulted in a strong reversal of the elastic limits, as expected.

Elastic limit determinations were made during only the first two steps in the negative cycle of deformation, since the results were obviously symmetrical with those of the positive cycle.

Longitudinal and crosssections were cut from the reduced sections of new test specimens at quarter-cycle stages of one complete cycle each of positive and negative 1 percent plastic deformation. The sections were mounted without heat in acrylic cement and carefully mechanically polished, electro-polished, and etched until all surface disturbance was removed. The X-ray diffraction measurements were made on a commercial horizontal diffractometer with cobalt $K\alpha_1$ characteristic radiation, using a proportional counter as a detector. Each specimen was continuously rotated about an axis normal to its surface in order to bring more grains into diffracting position. The position of the peak of the (400) line, near the 2θ diffraction angle of 153°, was determined by the analytical method of three-point parabola fitting of D. P. Koistinen and R. E. Marburger [9], as described in the SAE Information Report TR–182 [10]. Corrections were made in the intensity at each point for the Lorentz and polarization factors, and all values of the calculated Bragg angle were corrected for specimen temperature variation. The precision of peak determination was approximatly $\pm 0.02°$ in 2θ.

The value of the crystal lattice spacing observed normal to the surface of a given section compared to that of the annealed material enabled one to calculate the sum of the principal stresses parallel to the surface of the section. Because of the uniaxial manner of deformation, it was assumed that one principal stress σ_A, was axial in the specimen and two equal principal stresses, each σ_T, were at right angles to the axis. Hence, measurements on the cross section yielded a value, $2\sigma_T$, twice the transverse stress, and those on the longitudinal section yielded $(\sigma_A+\sigma_T)$, the sum of the axial stress plus the transverse stress. Therefore, the axial residual stress was calculated for each pre-strain condition by subtracting one-half the sum of the stresses found in the cross section from the sum of the stresses found on the longitudinal section. That is, $\sigma_A=(\sigma_A+\sigma_T)-\frac{1}{2}(2\sigma_T)$. The resulting values of axial residual stress are listed in table 1. Because of the involved nature of the calculation and the many possible sources of error, only an estimate of average uncertainty, $\pm 1\times 10^3$ psi, is expressed as a measure of precision of the results.

The behavior here again shows a kind of symmetry between the cycle of plastic deformation begun with an axial extension and the cycle begun with axial compression. After the first 1 percent plastic deformation, a residual axial stress is observed that is opposite in sign from the deformation; that is to say, after extension, a residual compressive stress is observed, and, after compression, a residual tensile stress is observed. That is the common behavior that has often been reported. After the second quarter step in the deformation cycles, the observed stress, though smaller in magnitude, has reversed sign so that it continues to be directed opposite to the deformation. After the third and fourth quarter steps, however, the residual stress is tensile in all cases, regardless of direction of deformation. This behavior is shown graphically in figure 1.

These residual stresses, resulting in a change in the X-ray diffraction peak position, are oriented microstresses, indicating a nonzero average component of stress present in the coherently diffracting material of many grains of the specimen in the X-ray beam. Another type of microstress, in which the residual stresses may be random in magnitude and sign as one goes from grain to grain, results in a broadening of the diffraction line. Two other factors in the specimen may increase line breadth: random microstress that varies within each grain (microstress of the "third kind," as it is sometimes called) and very small particle size. Previous study of individual diffraction spots on stationary film patterns made with a monochromatic misorientation goniometer [6], using some of the same specimens, however, revealed that neither of these factors were significant under the conditions of this investigation.

Line breadth measurements were made on the (400) diffraction line of the brass using cobalt $K\alpha_1$ radiation, employing the diffractometer with a 3° beam slit, a 0.1° receiving slit, Soller slits, scanning rate of 0.2° per min, rate meter time constant of 8 sec, recording chart speed of 0.4 in. per min, and specimen spinner in use. Since the $\alpha_1-\alpha_2$ doublet was not fully resolved in these patterns, one-half the breadth of the low-angle side of the α_1 line was measured at half-peak intensity and multiplied by two. Measurements on the cross and longitudinal sections of a specimen were very nearly equal and were averaged together. The observed breadth was corrected for instrumental broadening by the method

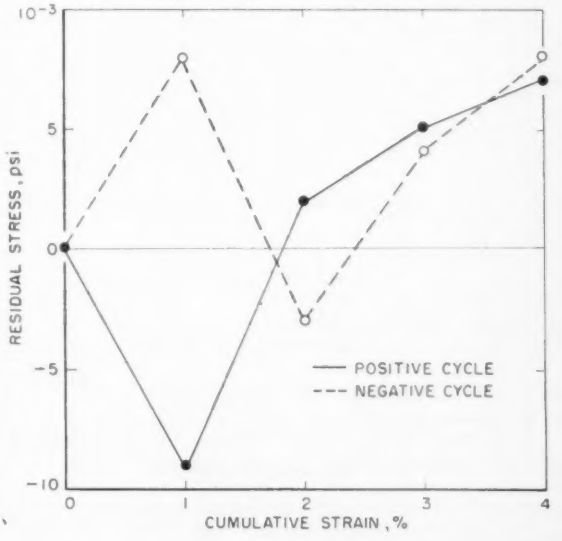

FIGURE 1. *Axial oriented residual stress versus cumulative plastic strain through one complete cycle of deformation.*

described by H. P. Klug and L. E. Alexander [11] for high-angle diffractometer lines. The maximum random microstress, without regard to sign, is given, according to B. D. Cullity [12], by

$$\sigma_{Mx}=\frac{E}{4\tan\theta}(\beta)$$

where σ_{Mx} is the maximum random tensile or compressive microstress, E is Young's modulus of the material, θ is the Bragg angle of diffraction, and β is the corrected line breadth. The values of β and σ_{Mx} are to be found in table 2. The precision in β is estimated to be about $\pm 0.05°$, which is reflected as an uncertainty of $\pm 0.7\times 10^3$ psi in σ_{Mx}.

It is apparent that the maximum random microstress is of the same order of magnitude as the residual directed microstresses. One may also see that there is no significant difference in the random stress level in the annealed specimen and those of the first two quarter steps of both the deformation cycles, after which the stresses rise markedly.

3. Discussion

The essential conclusion of Rovinskiy and Sinayskiy was that the Bauschinger effect can be explained by summing the residual directed microstress, determined by X-ray diffraction, with the externally applied macrostress to account for the lowered elastic limit measured in the direction opposite to a preceding plastic deformation (which we shall call the "reverse elastic limit"). The results of this study clearly demonstrate that this conclusion cannot with validity be extended to those cases where the immediately preceding deformation has itself been preceded by a plastic deformation in the opposite direction. This inequality of the residual stress and the decrease of the reverse elastic limit, $\Delta\sigma$, beyond the first quarter-cycle is presented graphically in figure 2, where both quantities are plotted against the cumulative strain. Throughout at least the first four quarter-cycle steps of a cycle of deformation, the Bauschinger effect, as can be seen in table 1, depends to a very high degree upon only the immediately preceding deformation. The effect of earlier deformations seems to be merely to increase slightly the difference between the forward and reverse elastic limits. An entirely different situation exists with regard to the X-ray determined residual axial stresses. As can be seen in table 1 and figure 2, only the first quarter-cycle shows an axial residual stress that approximates the Bauschinger decrease in reverse elastic limit. The residual stress at the second quarter-cycle, $+2\times 10^3$ psi, agrees in sign but not in magnitude with the decrease, $+10\times 10^3$ psi, in the limit. Clearly something other than the immediately preceding deformation is beginning to have an important effect. After the third and fourth quarter-cycles of deformation, the direction effect of the immediately preceding deformation is increasingly masked by this cumulative factor. At this point, specimens in the positive cycle and the negative cycle are indistinguishable on the basis of the axial residual stresses observed, whereas the Bauschinger effect, that is, the directionality in elastic limit, is undiminished.

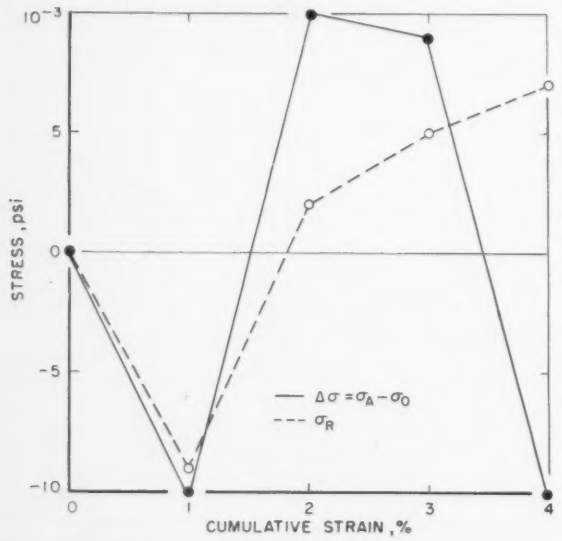

FIGURE 2. *Decrease in elastic limit and axial oriented residual stress versus cumulative plastic strain through one complete cycle of deformation.*

σ_A = Elastic limit of annealed material.
σ_o = Elastic limit observed in reverse direction after deformation.
σ_R = Axial oriented residual microstress measured by X-ray diffraction.

The validity of the various methods of calculating residual stresses from X-ray measurements continues to be open to some question. A new approach has recently been used by D. M. Vasil'ev [13,14] to compute the internal stress system from measurements on sections. He assumes as usual that the stress components lying in the plane of the cut are not affected by the cut. He does not make the usual assumption, however, that the component normal to the surface of the cut is relaxed to zero; but rather that, in the equations relating strain to stresses in this region reached by X-rays, it appears multiplied by a factor k, to be evaluated, which lies between zero and one. He computes k from data obtained from additional X-ray measurements. His resulting values of k vary typically from 0.2 in the case of aluminum (99.99 percent pure) examined with Cr Kα radiation to 0.7 in the case of Fe_3C examined with Cr Kα radiation. A surprising result of his measurements and calculations is that all principal stresses, both axial and transverse, after either uniaxial extension or compression, are always compressive. This is obviously in conflict with the usual result that the residual axial stress is opposite to the direction of deformation, as was used by Rovinskiy and Sinayskiy for the basis of their explanation of the Bauschinger effect. It is also in conflict with our result that, after cyclic axial deformation, the residual axial stress becomes tensile regardless of the direction of the last axial deformation.

No attempt was made in this study to evaluate k by the somewhat complex procedure of multiple inclined incidence X-ray exposures of Vasil'ev. However, calculations were made of the axial stresses

using a $\underline{k}$ of 0.4, Vasil'ev's value for copper with cobalt radiation. These calculations yielded results containing both tensile and compressive stresses, at least qualitatively similar to those obtained by the accepted procedure and listed in table 1. These newer values were not added to the table, however, because they did not seem to add appreciably to the results already presented, and, moreover, there does not appear to be adequate evidence that the value of 0.4 used for $\underline{k}$ was more nearly correct than the usual value zero.

While the directed residual stresses seem gradually to lose any relationship with the elastic limits as the plastic strain cycle passes the three-quarter mark, the values of the maximum random microstress calculated from diffraction line breadth measurements and listed in table 2 show an abrupt change after the third quarter step in the deformation cycle. Since no such marked change in the Bauschinger effect is observed at this point, it seems clear that the latter, at least in the cyclic case, is the result of some factor or factors other than either of these types of microstresses revealed by X-ray diffraction.

TABLE 2. *Results of line breadth measurements*

Plastic condition of specimen	Corrected line breadth $\beta(2\theta°)$	Max. random microstress σ_{Mx} (10^3 psi)
Annealed	0.35	5.2
Positive cycle of deformation		
E	0.30	4.5
E–C	.35	5.2
E–C–C	.50	7.5
E–C–C–E	.55	8.2
Negative cycle of deformation		
C	0.35	5.2
C–E	.35	5.2
C–E–E	.50	7.5
C–E–E–C	.50	7.5

E=extended 1%. C=compressed 1%.
Average uncertainty in β approximately $\pm 0.05°$.
Average uncertainty in σ_{Mx} approximately $\pm 0.7 \times 10^3$ psi.

It may be that the Rovinskiy and Sinayskiy model of the part played by the oriented microstress is correct for the first deformation of an annealed material; but that, as the material is subjected to further strain of a cyclic nature, another type of residual stress arises that is always tensile in character and increasing, perhaps asympotically, in magnitude, while that associated with the Bauschinger effect is outweighed or masked, after the third quarter stage, altogether. The rise of this conjectural new type of residual stress is also indicated at this point in the cycle by the increase in line broadening. The Bauschinger effect, in the meantime, is not affected at all; the elastic limits are as strongly directional at the end of a cycle of deformation as at the beginning. One must conclude, therefore, that an explanation of the Bauschinger effect that is valid in all cases must be based on some model other than the additive action of those types of residual microstress that are revealed by X-ray diffraction effects of peak shift or broadening.

The plastic properties of metals in general are being explained with increasing success on the basis of the dislocation theory of behavior as exemplified in the work of A. H. Cottrell [15], N. F. Mott [16], and many others. Some application of the theory has been made to the problem of the mechanism of the Bauschinger effect, as for example in the work of R. L. Wooley [17] and that of S. N. Buckley and K. M. Entwistle [18]. A critical review of these theories is beyond the scope of this paper; it appears, however, that there does not yet seem to be a theory sufficiently complete to enable one to predict quantitatively the behavior of the forward and reverse elastic limits of a cyclically deformed polycrystalline specimen such as used in this study. No doubt the complexity of the physical situation in experiments such as this with polycrystalline brass is such that it would be difficult, if not impossible, to apply dislocation theory quantitatively and with rigor. It has been suggested that the Bauschinger effect is a result of the nonsymmetry of the stress potential associated with a dislocation arrangement after flow, as, for example, arising from a pile-up against obstacles on the slip plane or from the interaction of other dislocations on parallel slip planes. If this is true, the elastic stresses in the crystal lattice would probably be quite localized, on the scale of perhaps 10^2 or 10^3 interatomic distances; whereas the stresses associated with X-ray measurements are averaged over much larger dimensions. Even if the tool of X-ray microstress measurement were sufficiently sensitive to reveal the nature of a localized dislocation configuration after an initial deformation of the order of 1 percent, it should probably not be surprising that this information would become masked by more gross structural effects and would cease to be a major contributor to the X-ray microstress after the cumulative effects of reversed plastic strain past the middle of a strain cycle became important in the specimen.

4. Summary and Conclusions

The principal experimental facts reported in this study may be summarized as follows:

(a) The elastic limits indicated a strong Bauschinger effect in alpha brass throughout a complete cycle of axial plastic deformation of 1 percent amplitude.

(b) There was no marked change in the effect as the cycle progresses; only a slight hardening was apparent.

(c) The axial oriented residual microstress was not additive to the applied stress to account for the Bauschinger effect in the latter part of the cycle; in fact, after the third-quarter stage, the microstress appears always to become positive in sign (tensile).

(d) The random maximum microstress (X-ray line broadening) remains near the value found in the annealed material until it exhibits a marked change at the three-quarter cycle condition of the specimen.

These facts point to the following conclusions:

(a) The effect of the cyclic deformation on the elastic limits seems to require two mechanisms (at least): one to account for the forward limit hardening; a second to account for the large reduction of the reverse limit. Neither mechanism would appear to be strongly affected by the cumulative strain of one complete cycle of 1 percent amplitude of plastic deformation.

(b) Since both the oriented and the maximum random microstresses measured by X-ray techniques show a marked change in character after three-quarters of a cycle of deformation while the Bauschinger effect does not, they are not directly related to the Bauschinger effect, at least under these conditions of reversed plastic deformation.

(c) The cyclic uniaxial working of this material leads to a residual stress in the axial direction. Determined by X-ray diffraction, this is a positive (tensile) stress.

The author acknowledges the cooperation of colleagues at the National Bureau of Standards who made significant contributions to this investigation: in particular, H. C. Vacher, who supplied valuable assistance in the planning stage, E. Escalante, who assisted in the measurements of elastic limits, and P. D. Sarmiento, who assisted in the preparation of specimens for X-ray diffraction examination.

5. References

[1] J. Bauschinger, Mitt. mech. tech. lab. Munchen., Heft **13,** 1 (1886), and Min. Proc. Inst. Civil Eng., **87,** 463 (1886–87).

[2] C. S. Barrett, Structure of metals, 2d ed., 359–60 (McGraw-Hill Book Co., Inc., New York, N.Y., 1952).

[3] C. S. Barrett, Structure of metals, 2d ed., pp. 316–335 (McGraw-Hill Book Co., Inc., New York, N.Y., 1952).

[4] S. L. Smith and W. A. Wood, Internal stress created by plastic flow in mild steel, and stress-strain curves for the atomic lattice of higher carbon steels, Proc. Royal Soc. London **182,** 404–14 (1944).

[5] B. M. Rovinskiy and V. M. Sinayskiy, On the nature of the Bauschinger effect, Izvestia Akad. Nauk SSSR, Metallurgiia i Toplivo (Proceedings of the USSR Academy of Sciences, Department of Technical Sciences, Metallurgy and Fuel) No. 6, 137–41, 1959).

[6] C. J. Newton and H. C. Vacher, X-ray diffraction measurement of intragranular misorientation in alpha brass subjected to reversed plastic strain, J. Research NBS. **65C** (Eng. & Instr.) No. 1, 57–63 (1961).

[7] C. J. Newton and H. C. Vacher, Residual lattice strains in sectioned bars of plastically deformed iron, J. Metals, Trans. Section, AIME, TN 281E, **7,** No. 11, Pt. 1, 1193–92 (1955).

[8] C. J. Newton, False negative permanent strains observed with resistance wire strain gages, ASTM Bul. No. 235, 42–44 (1959).

[9] D. P. Koistinen and R. E. Marburger, Simplified procedure for calculating peak position in X-ray residual stress measurements on hardened steel, ASM Trans. **51,** 537 (1959).

[10] A. L. Christenson, ed., The measurement of stress by X-ray, SAE Information Report TR-182, The Soc. Automotive Eng., New York, N.Y.

[11] H. P. Klug and L. E. Alexander, X-ray diffraction procedures, 510 (John Wiley & Sons, Inc., New York, N.Y., 1954).

[12] B. D. Cullity, Elements of X-ray diffraction, 265 (Addison-Wesley Publ. Co., Inc., Reading, Mass., 1956).

[13] D. M. Vasil ' ev, On microstresses occurring in plastic deformation of polycrystalline specimens, Zhurnal Teknicheskoi Fiziki **28,** No. 11, 2527–42, Nov. 1958. J. Tech. Phys. USSR, (Eng. Trans). **3** (**28**),2315–28 (Sept.-Dec. 1958).

[14] D. M. Vasil ' ev, Microstresses created in metals during plastic deformation II, Fizika Tverdogo Tela **1,** No. 11, 1736–1746, (Nov. 1959). Soviet Physics Solid State (Eng. Trans.), **1,** No. 11, 1586–95 (May 1960).

[15] A. H. Cottrell, Dislocations and plastic flow in crystals, 114 (Oxford University Press, London, 1953).

[16] N. F. Mott, A theory of work hardening of metal crystals, Phil. Mag. Ser. 7 **43,** 1151–78 (1952).

[17] R. L. Wooley, The Bauschinger effect in some face-centered and body-centered cubic metals, Phil. Mag. Ser. 7 **44,** 597–618 (1953).

[18] S. N. Buckley and K. M. Entwistle, The Bauschinger effect in superpure aluminum single crystals and polycrystals, Acta Met. **4,** 352–61, (1956).

(Paper 65C4—79)

JOURNAL OF RESEARCH of the National Bureau of Standards—C. Engineering and Instrumentation
Vol. 65C, No. 4, October–December 1961

A Study by Polarization Techniques of the Corrosion Rates of Aluminum and Steel Underground for Sixteen Months

W. J. Schwerdtfeger

(July 6, 1961)

One aluminum and one steel specimen were exposed underground for 16 months in order to make a running survey of their corrosion rates as influenced by weather and time.

Cathodic and anodic data were obtained periodically as a basis for calculating rates of corrosion. Automatic polarizing and recording equipment, housed indoors, was used for making the measurements. The method is adaptable for field use in making corrosion rate or soil corrosivity studies where commercial power sources are not available.

1. Introduction

The present investigation was carried out to evaluate polarization techniques for measuring rates of corrosion of aluminum and steel underground. An exposure period of at least 1 year was decided upon in order to study the effects of time and climatic changes on the corrosion rates of these materials in one environment. For convenience, both materials were placed underground outside of the laboratory which housed the measuring apparatus.

The theory upon which the measurements were based has been applied to the measurement of local action corrosion currents on steel exposed to aqueous environments in the laboratory [1].[1] Briefly stated, the method consists of noting the value of cathodic and anodic current applied in increasing amounts to a corroding specimen which coincides with a change-in-slope (break) in the respective polarization curve and which is indicative of the current necessary to stop local-action corrosion.

A logarithmic relationship between the value of current at the break in the controlling polarization curve and the rate of polarization (based on the curve) was observed to be reasonably applicable to both the steel and the aluminum. A similar relationship was described previously [2] together with related work of other investigators [3].

The technique described here could be put to practical use in the field for measuring corrosion rates (based on weight loss), screening metals and alloys for long-time exposure in aqueous environments, or for measuring soil corrosivity.

2. Experimental Procedure

2.1. Preparation and Exposure of Specimens

Two specimens were used, one of low carbon steel and one of high purity aluminum. Each specimen was in the form of a tube (about 1.87 in. o.d. by 12 in. long) with rubber caps sealed on the ends, leaving about 0.4 ft^2 of outer surface for exposure to the soil.

Before capping, the ends of the specimens were rounded with a file and smoothed with fine abrasive cloth. The outer and inner surfaces of the steel tube were cleaned with a motor-driven wire brush to remove any trace of scale or superficial rust. The surfaces of the aluminum tube were polished with fine abrasive cloth, and scrubbed under hot water. Each specimen was then weighed to the nearest milligram. An insulated stranded-copper wire was then soldered to an inside edge of each tube and the soldered joint coated with paint. Next, the inside surfaces of the tubes were coated with a film of rust-preventive oil and the rubber caps pressed on and sealed. The lead wire came through a hole bored in the center of one of the caps. The area where the wire protruded was sealed with bitumen.

The two specimens were buried underground outside of the laboratory, Washington, D.C., in soil having a resistivity of about 7500 ohm-cm. They were spaced 3 ft apart in a vertical position in holes dug 30 in. deep with a post-hole auger. An auxiliary electrode (steel channel 1.5 in. by 4 in. by 19 in.) was similarly buried about 20 ft away from the specimens. The rubber-covered wires from the specimens, auxiliary electrode and one for a reference electrode, led to the laboratory where polarization measurements were made.

2.2. Electrical Measurements

Potential and polarization measurements were made periodically (on 40 occasions) during the 16 months that the specimens were exposed. The separate potentials were measured with a 200,000 ohm/v voltmeter and the polarization data were obtained with a two-pen (current and potential) strip-chart recorder. The circuit used for balancing out IR drop, automatically applying polarizing current, and recording current and potential, has been previously described [4]. A copper-copper sulfate half-cell was used for the reference electrode. When measurements were to be made, the reference electrode was placed on the surface of the earth about 3 ft from the specimens and between them and the auxiliary electrode. The auxiliary electrode served either as an anode or a cathode.

[1] Figures in brackets indicate the literature references at the end of this paper.

Apparatus for obtaining polarization data has also been built for field use by using dry batteries and controls for manually varying the polarizing current. Portable indicating-type instruments consisting of a potentiometer (galvanometer-type null indicator) and a milliammeter are used. An earth-auger (1 in. diam) appropriately fitted with a cross-bar for turning, is used as the auxiliary electrode. When obtaining polarization data in the field equal increments of polarizing current are applied at approximately equal time intervals (1 or 2 min intervals).

2.3. Removal of Corrosion Products

After 483 days of underground exposure, the aluminum and steel specimens were removed for cleaning, weight loss determinations and pit-depth measurements. The aluminum specimen was submerged in hot water and brushed with a stiff-bristle brush. After the rubber caps were taken off, the wire and solder were removed by applying heat from a soldering iron. The specimen was then placed in concentrated nitric acid for 5 min, washed in running water, dried, and weighed. The effectiveness of the cleaning procedure was checked by repeating the nitric acid treatment and reweighing. There was no significant difference between the two weighings, indicating that the specimen was free of corrosion products.

Rust which had formed on the steel specimen was very adherent. First, the steel was cleaned cathodically in a 3 percent NaCl solution for 5 hr at a current density of 1 amp/ft.^{2} The specimen was then immersed for 2 hr in a 10 percent ammonium citrate solution (at 150 °F) made alkaline with ammonium hydroxide. Finally the steel was hand brushed (wire brush), washed, dried, and weighed.

3. Results and Discussion

Some of the polarization data covering the 16 months of exposure are shown for steel and aluminum, respectively, in figures 1 and 2. The dates are given so that the data can be related to the time of year. The initial curves were obtained after the specimens were in the ground for 3 days and the final curves shown were run on the day preceding their removal. All data were taken from the recorder charts and plotted on semi-log scale. The corrosion current controls the magnitude of the polarizing currents Ip and $-Iq$ [1], indicated by the breaks in the curves (fig. 1 and 2). It will be observed in figures 1 and 2, that the current Iq approaches in value the current Ip with the passing of time, particularly for the steel. Thus, the tendency is a change from cathodic to mixed control.

The polarizing currents, Ip and Iq, used in calculating the values of corrosion current were obtained as shown in figures 1 and 2. Polarization rates ($\Delta V/\Delta I$) were calculated at the slightly larger values of current indicated by arrows on the curves. These rates seem to bear a logarithmic relation to the currents Ip as shown by previous work [2]. Data from the previous work on steel in a NaCl solution and

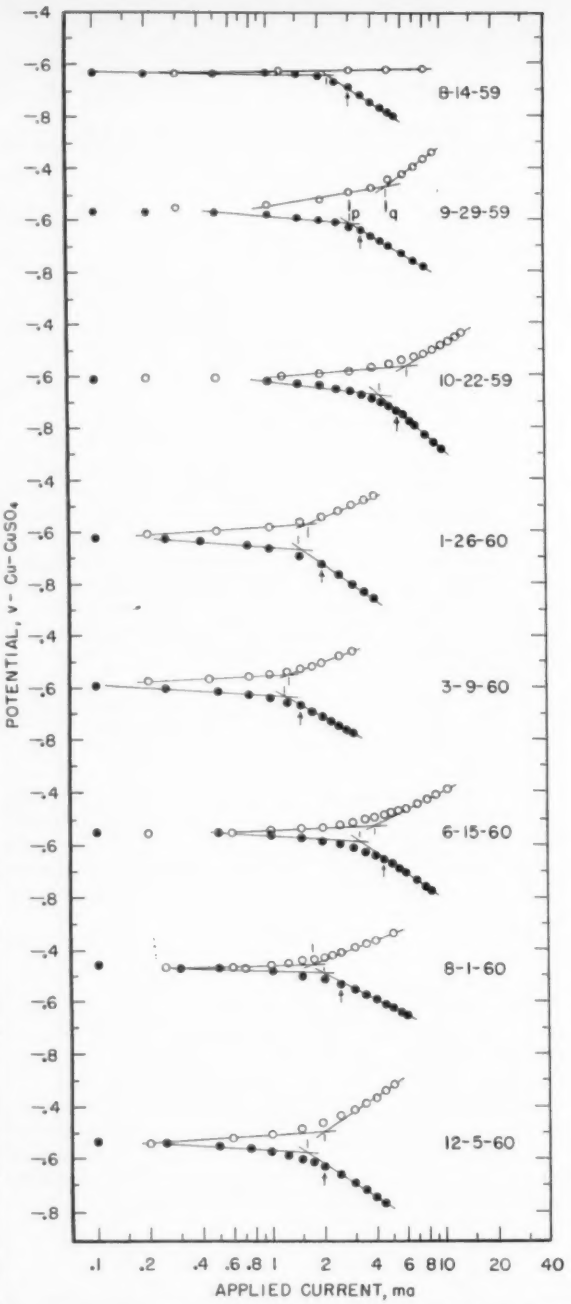

FIGURE 1. *Typical polarization curves of the underground steel specimen during the 16 month exposure period.* ●*Cathodic,* ○*Anodic.*

To convert applied current to current density (ma/ft^2), multiply by 2.5.

the present data are shown in figure 3. The present data for aluminum also appear to fit reasonably well. Thus, knowing the polarization rate ($\Delta V/\Delta I$), it is possible to estimate the current Ip from the

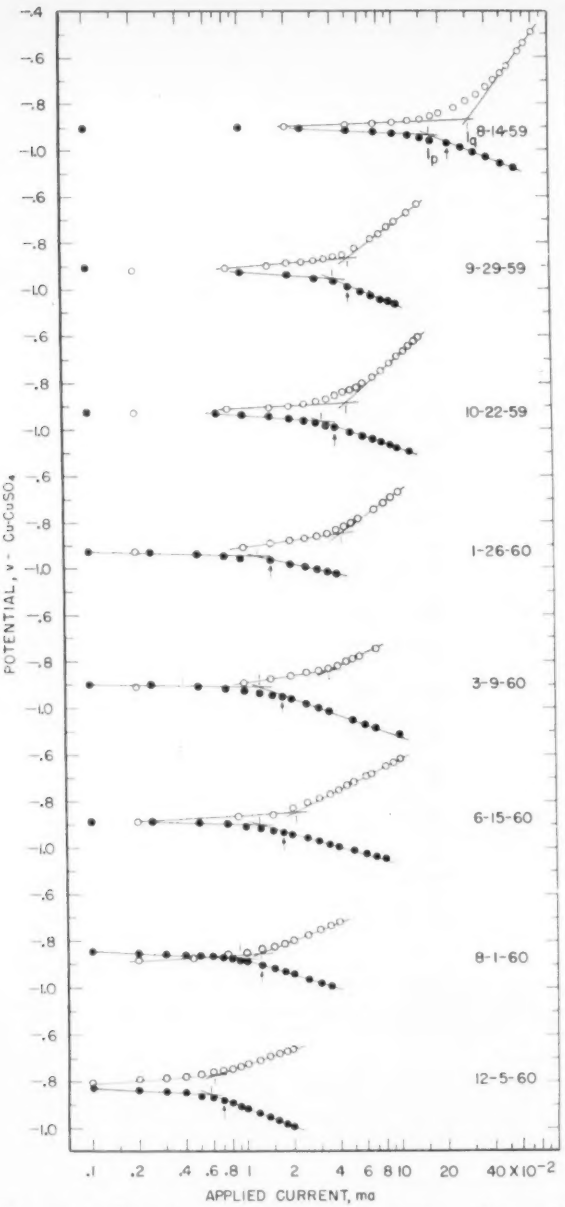

FIGURE 2. *Typical polarization curves of the underground aluminum specimen during the 16 month exposure period.* ●*Cathodic,* ○*Anodic.*

To convert applied current to current density (ma/ft²), multiply by 2.5.

curve (fig. 3). The empirical equation for data (fig. 3) may be written:

$Ip = c\ R^{-n}$; or $\log Ip = \log c - n \log R.$, where $c = 100$ (y—intercept), $R = \Delta V/\Delta I$ in mv/ma/ft², $n = -1.1$ (slope of curve) and Ip is expressed in ma/ft.²

This relationship would be useful where the break in the curve is not readily apparent. The author is currently investigating the scope of this relationship with possible application to ferrous alloys such as stainless steels. When the type of control is predominantly anodic, the anodic polarization data should fit the relationship.

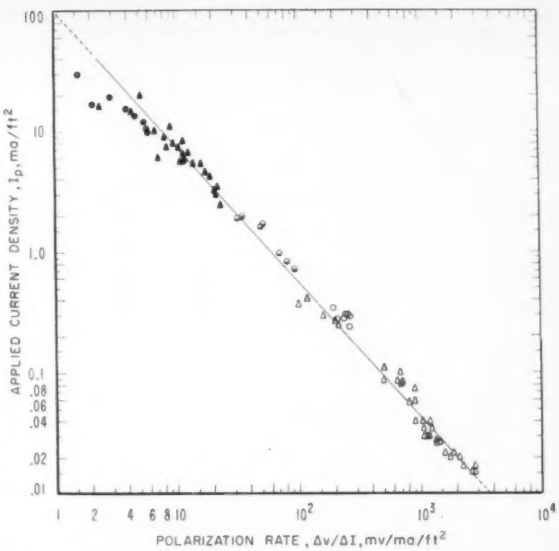

FIGURE 3. *Logarithmic relationship (cathodic polarization), for steel and aluminum, between the polarizing current, Ip, and the polarization rate, $\Delta V/\Delta I$.*

▲Bare steel underground (covering 16 months exposure); △bare aluminum underground (covering 16 months exposure); ●bare steel in 3 percent sodium chloride solution (covering 14 days exposure); ○coated steel (carbonate coating) in 3 percent sodium chloride solution (covering 29 days exposure); ◒coated steel (carbonate, progressively damaged) in 3 percent sodium chloride solution (covering 36 days exposure).

All data obtained for the steel and aluminum from the polarization curves (semi-log scale) used for calculating weight losses are shown respectively in tables 1 and 2. The calculated and actual weight loss for steel agree within 6 percent. On a percentage basis the same cannot be said for the aluminum but, considering the relatively small weight loss involved, the calculated weight loss is considered quite significant. Actually, the difference (about 50 mg) between the actual (as weighed) and calculated corrosion losses could be largely cleaning error for a soft metal such as aluminum.

For the first 3 months of exposure, polarization data were obtained more frequently than later. During this initial period, changes in the corrosion rate of both steel and aluminum appeared to be occurring frequently. Also, the corrosion rates were higher and seemed to be influenced more by changes in the weather and the passing of time. The effects of time, temperature, and rainfall on the corrosion current for steel and aluminum in this particular underground environment are shown in figure 4. Potentials of both the steel and aluminum are also plotted with soil resistance and climatological data. For the steel, the corrosion current (i_0) varied considerably for the first 2 months of exposure. The rainfall early in September 1959 and again early in October lowered the soil resistance and apparently caused the two peaks (fig. 4) in the corrosion current.

TABLE 1. *Weight loss calculated from polarization data on a steel specimen exposed underground for 16 months*

Time of year	Polarizing current [a] at break in curve		Corrosion [b] current i_o	Exposure time	Weight loss	
	Cathodic Ip	Anodic Iq			Calculated [c] cumulative	Actual
	ma	*ma*	*ma*	*Days*	*mg*	*mg*
8-12-59	2.5	10.0 [d]	2.0	1	50	
14	2.3	9.2 [e]	1.8	3	145	
19	2.4	4.8 [d]	1.6	8	357	
25	2.3	4.6 [d]	1.5	14	582	
9-4-59	6.6	13.2 [d]	4.4	24	1332	
8	5.9	8.4 [e]	3.5	28	1712	
18	3.5	4.2	1.9	38	2387	
29	3.0	5.0	1.9	49	2909	
10-1-59	7.9	13.5 [e]	5.0	51	3084	
9	4.1	6.7	2.5	59	3824	
22	4.4	6.4	2.6	72	4669	
11-4-59	2.3	7.3	2.3	85	5482	
13	2.8	7.7	2.1	94	5978	
30	2.7	6.5	1.9	111	6828	
12-22-59	2.0	4.9	1.4	133	7708	
1-13-60	1.9	2.8 [e]	1.1	155	8423	
26	1.4	1.7	0.77	168	8725	
2-19-60	1.3	1.4 [e]	0.67	192	9157	
3-4-60	1.0	1.5	0.60	206	9381	
9	1.2	1.3	0.62	211	9457	
25	1.7	1.9	0.90	227	9761	
4-6-60	2.2	2.3	1.1	239	10061	
28	2.7	2.7 [d]	1.3	261	10721	
5-20-60	2.5	2.5	1.3	283	11435	
23	3.0	3.0 [d]	1.5	286	11540	
6-2-60	3.5	3.5 [d]	1.8	296	11940	
15	3.2	4.0	1.8	309	12526	
30	2.7	3.0	1.4	324	13088	
7-18-60	2.2	2.6	1.2	342	13674	
26	2.3	2.6	1.2	350	13914	
28	1.9	1.8	0.92	352	13969	
8-1-60	1.9	1.7	0.90	356	14060	
19	3.6	3.4	1.7	374	14645	
9-1-60	2.2	2.3	1.1	387	15100	
14	3.0	3.1	1.5	400	15522	
10-11-60	2.9	2.7	1.4	427	16467	
26	2.2	2.3	1.1	442	16954	
11-23-60	2.0	2.1	1.0	470	17723	
12-5-60	1.6	2.0	0.89	482	18005	
6				483	18027	19055

[a] From curves in figure 1 and other curves not shown.
[b] $i_o = Ip\ Iq/(Ip+Iq)$.
[c] Weight loss (g) $= K\,t\,i$, where $K = 2.8938 \times 10^{-4}$ g per coulomb, $i = i_o$ = Average current (amp) for the period (t in seconds) between successive readings. The value of i_o at the instant of exposure and at the end of exposure is taken as the initial and final values, respectively, as calculated.
[d] No anodic run; value based on other Ip/Iq ratios around that time.
[e] No apparent break; value based inversely on relative cathodic and anodic polarization rates $\Delta V/\Delta I$ and Ip.

TABLE 2. *Weight loss calculated from polarization data on an aluminum specimen exposed underground for 16 months*

Time of year	Polarizing current [a] at break in curve		Corrosion [b] current i_o	Exposure time	Weight loss	
	Cathodic Ip	Anodic Iq			Calculated [c] cumulative	Actual
	ma	*ma*	*ma*	*Days*	*mg*	*mg*
8-12-59	0.15	0.30 [d]	0.10	1	0.8	
14	.17	.31	.11	3	2.6	
19	.12	.25	.081	8	6.4	
25	.10	.20	.067	14	10.0	
9-4-59	.11	.20	.071	24	15.6	
18	.043	.080	.028	38	21.1	
29	.040	.050	.022	49	23.4	
10-1-59	.039	.050 [d]	.022	51	23.8	
9	.035	.050	.021	59	25.1	
22	.032	.048	.019	72	27.2	
11-4-59	.030	.050	.019	85	29.3	
13	.024	.043	.015	94	30.5	
30	.035	.068	.023	111	33.1	
12-22-59	.034	.062	.022	133	37.2	
1-13-60	.023	.055	.016	155	40.6	
26	.012	.043	.009	168	41.9	
2-19-60	.016	.042	.012	192	43.8	
3-4-60	.012	.037	.009	206	45.0	
9	.011	.035	.008	211	45.3	
25	.014	.033	.010	227	46.5	
4-6-60	.016	.056	.012	239	47.6	
28	.016	.040	.011	261	49.7	
5-20-60	.014	.042 [d]	.011	283	51.7	
23	.011	.033	.009	286	51.9	
6-15-60	.012	.022	.008	309	53.6	
30	.009	.020	.006	324	54.4	
7-18-60	.008	.015	.005	342	55.1	
26	.008	.015	.005	350	55.4	
8-1-60	.009	.012	.005	356	55.6	
19	.011	.013	.006	374	56.5	
9-1-60	.008	.011	.005	387	57.0	
14	.011	.012	.006	400	57.6	
10-11-60	.007	.011	.004	427	58.7	
26	.006	.007	.003	442	59.1	
11-23-60	.007	.007	.004	470	60.0	
12-5-60	.006	.006	.003	482	60.4	
6				483	60.7	109

[a] From curves in figure 2 and other curves not shown.
[b] $i_o = Ip\ Iq/(Ip+Iq)$.
[c] Same as footnote in table 1, except $K = 0.9316 \times 10^{-4}$ g per coulomb.
[d] No anodic run; value based on other Ip/Iq ratios around that time.

During the next 5 months, the corrosion current continued to decrease, presumably due to the drop in air temperature and resultant lowering of soil temperature. The lowest value of corrosion current was observed in March 1960, the coldest time of the year when the soil resistance was maximum. From this time until the beginning of June, air temperatures continued to rise, soil resistance became lower, and the corrosion current again increased. During the summer 1960, fluctuations in the corrosion current apparently were caused by rainfall. With the coming of colder weather, the soil resistance again increased and the corrosion current diminished. The major fluctuations in potential of the steel occurred during the early months of exposure. After the corrosion products began to build up, there was a tendency for the potential to become gradually more electropositive.

The corrosion rate of the aluminum seemed to be less affected by changes in weather than that of the steel. The current for the aluminum (fig. 4) dropped considerably during the first 2 months and gradually thereafter. In contrast with the steel, the aluminum corrosion current decreased about 30-fold while that of the steel decreased around 8-fold during the 16 months.

After the specimens had been cleaned, the pit depths were also measured. On the steel, the maximum pit depth was 0.035 in. and the six deepest pits averaged 0.03 in. For the aluminum, the maximum pit depth was 0.008 in. The six deepest pits averaged 0.007 in.

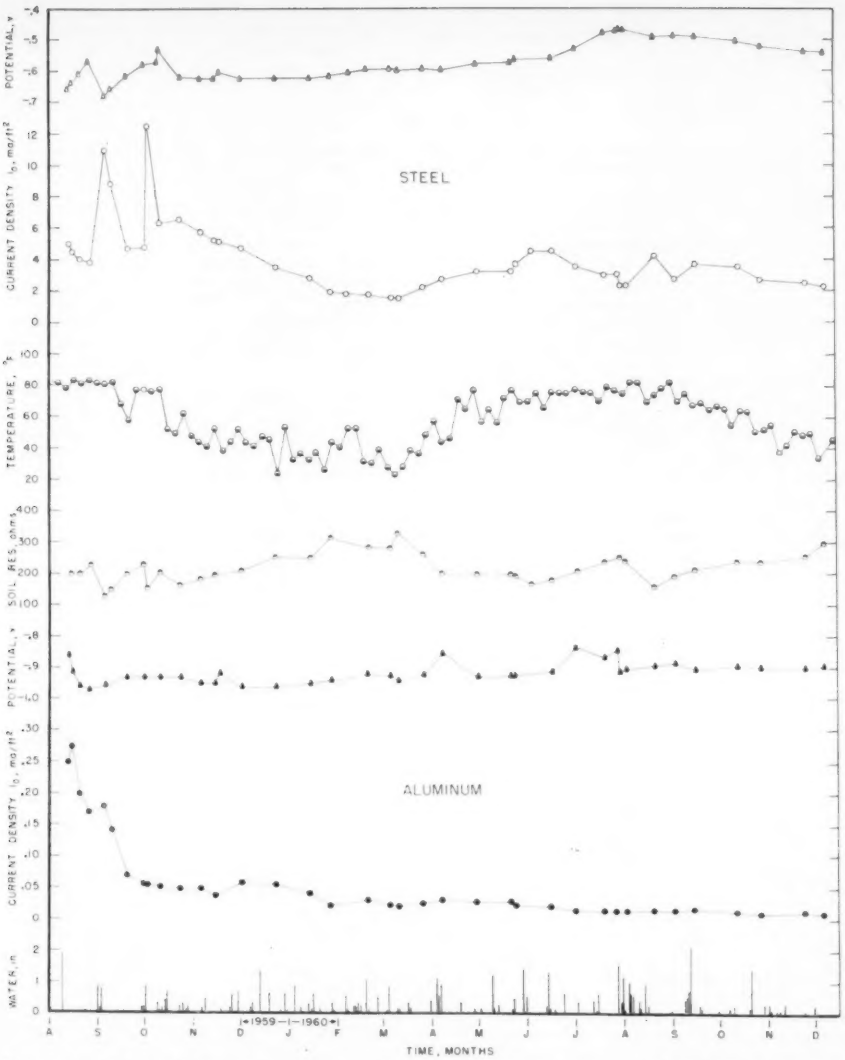

FIGURE 4. *Effect of time and weather on the corrosion rate and potential of steel and aluminum exposed underground for 16 months.*

△ Potential, steel; ○ corrosion current, steel; ◒ air temperature; ▲ potential, aluminum; ● corrosion current, aluminum; ◓ soil resistance, between steel specimen and reference electrode; | precipitation (water) in area—U.S. Weather Bureau.

4. Summary

A steel and an aluminum specimen were exposed underground for 16 months to a soil having an average resistivity of about 7500 ohm-cm. During this time, cathodic and anodic polarization curves were automatically recorded on 40 occasions with the idea of evaluating a technique for measuring rates of corrosion and noting the effects of the weather on such rates.

The weight loss of each material caused by corrosion agreed quite well with the calculated losses based on the polarization data. The cathodic polarization data for both the steel and aluminum seem to fit reasonably well a logarithmic relationship, discussed in a previous publication [2], which is helpful in anticipating rates of corrosion.

Both materials corroded at a faster rate during the early months of exposure than later. The corrosion rate of the aluminum diminished more rapidly and to a greater degree than that of the steel. The corrosion rate of the steel was affected more by temperature and rainfall than was that of the aluminum.

This investigation was not intended to evaluate the relative merits of the metals exposed to corrosion. While their relative behavior is of interest, it must be remembered that only one soil environment was involved.

The weather data were copied from the local climatological data sheets, U.S. Department of Commerce, Weather Bureau.

5. References

[1] W. J. Schwerdtfeger, Measurement of the corrosion rate of a metal from its polarizing characteristics, J. Electrochem. Soc. **99**, 407 (1952).

[2] W. J. Schwerdtfeger and Raul J. Manuele, Coatings formed on steel by cathodic protection and their evaluation by polarization measurements, J. Research NBS **65C,** (July-Sept. 1961).

[3] R. V. Skold and T. E. Larson, Measurement of the instantaneous corrosion rate by means of polarization data, Corrosion **13,** 139 *t* (Feb. 1957).

[4] W. J. Schwerdtfeger, Current and potential relations for the cathodic protection of steel in a high-resistivity environment, J. Research NBS **63C,** 37 (July-Sept. 1959), Corrosion **16** (May 1960).

(Paper 65C4–80)

JOURNAL OF RESEARCH of the National Bureau of Standards—C. Engineering and Instrumentation
Vol. 65C, No. 4, October–December 1961

Publications of the National Bureau of Standards

Selected Abstracts

On the spectrum of terrestrial radio noise at extremely low frequencies, H. R. Raemer. *J. Research NBS* **65D** (*Radio Propagation*) *No. 6,* (*November–December 1961*) *70 cents.*

A theory of the frequency spectrum of radio noise at extremely low frequency (ELF) is presented and the results compared with recent measurements of the first five "Schumann" resonant modes (between 8 and 34 c/s) made by Balser and Wagner [1960]. The source of this noise is assumed to be return strokes in vertical cloud-ground lightning flashes distributed randomly in time, uniformly in angular displacement along the earth relative to the observer, and with statistics of stroke duration, inter-stroke intervals, and strokes per flash taken from studies of thunderstorms reported by J. C. Williams. Thus, the mathematical model for the noise sources is an extremely simple one, being analogous to the shot effect in electron devices. The electromagnetic model employs the familiar waveguide mode theory, assumes a sharply bounded homogeneous ionosphere, and neglects the earth's magnetic field.

Agreement between the shape of the theoretical and observed spectrum is good for the first three modes and rather poor for the higher modes.

It is found by matching the theoretical resonant frequencies to the observed resonances that the product of effective ionosphere height h and the square root of effective conductivity $\sqrt{\sigma_i}$ is a decreasing function of frequency. The functional dependence of this quantity on frequency is determined and used in the calculation of the mode spectrum.

Discrepancies between the theory and experimental results are believed to be partially due to the artificiality of the sharply bounded homogeneous ionosphere model and to failure to give sufficient probability weighting to equatorial regions of abnormally high thunderstorm activity.

These last items are the subjects of continuing work on the extension of the theory.

Bibliography of temperature measurement—January 1953 to June 1960, C. Halpern and R. J. Moffat, *NBS Mono. 27* (*1961*) *15 cents.*

There are presented more than 500 references to the field of temperature measurement. These references were collected from two general sources: Scientific and technical literature, and government reports. The period covered is from 1953 to June 1960, with some from earlier dates. For convenience of the user, the references are divided into a number of categories based on the type of instrument used. Some references to calibration of instruments and to scientific theories, on which temperature measurement is based, are also presented.

Corrected optical pyrometer readings, D. E. Poland, J. W. Green, and J. L. Margrave, *NBS Mono. 30* (*1961*) *55 cents.*

The table of corrected optical pyrometer readings enables optical pyrometer users to convert observed temperature immediately to the true temperature, if the effective emissivity of the material being observed is known. The table gives observed temperatures from 1,000 to 3,000 °K in increments of 5 degrees, from 3,000 to 5,000 °K in increments of 10 degrees, from 5,000 to 10,000 °K in increments of 50 degrees, and from 10,000 to 39,900 °K in increments of 100 degrees. For these, true temperatures are tabulated for 49 emissivities ranging from 0.02 to 0.98 in increments of 0.02. These calculations were made on a 650 electronic computer using Planck's law, and the value $C_2=1.438$ cm deg for the radiation constant.

Publications of the National Bureau of Standards July 1, 1957, to June 30, 1960 (Includes titles of papers published in outside journals 1950 to 1959), B. L. Arnold, *NBS Misc. Publ. 240* (*1961*) *$2.25.*

This Supplement lists the publications of the National Bureau of Standards from July 1, 1957, to June 30, 1960. A brief abstract for each publication is given. It also includes a list of those papers by Bureau authors that have appeared in non-National Bureau of Standards Journals from 1950 through 1959. Subject and author indexes are included, and general publication information is furnished. This catalog and previous lists (see page 2) give reference to the publications printed by the Bureau during the period 1901 to June 30, 1957.

NBS—source of American standards, W. A. Wildhack, *ISA J.* **8,** *No. 2, 45–50* (*February 1961*).

A general description of the National Bureau of Standards and its program is given, with particular emphasis on development of standards and provision of calibration services.

Calculation of properties of magnetic deflection systems, S. Penner, *Rev. Sci. Instr.* **32,** *No. 2, 150–160* (*February 1961*).

A convenient matrix method for calculating properties of magnetic deflection systems is presented. This method is applicable to particle beams of small spatial and angular extent, and small energy spread. Equations for quadrupole lenses and for deflecting magnets are given. Examples are given to show the procedure for calculating the parameters of magnet systems.

Stepless variable resistor for high currents, C. R. Yokley and J. B. Shumaker, Jr., *Rev. Sci. Instr.* **32,** *No. 1, 6–8* (*January 1961*).

A variable-area water rheostat has been applied to the problem of current control in electric arc and plasma generating equipment. Resistance between 0.5 and 30 ohms can be obtained by adjusting the height of circulating water which surrounds pairs of fixed vertical aluminum plates. The electrolyte is ordinary city water which is circulated through the tank and discharged. No special filtering, pumping, or other treatment is used. The unit is located in the open air outside the laboratory and all control functions are operated from a remote switching panel. The unit has been operated using a maximum of 125 amp at 400 v dc and 1000 amp at 230 v dc.

Physical quantities proposed for radiation measurements, L. S. Taylor, *Proc. IXth Intern. Congress of Radiology, July 23–30, 1959* (*München, Germany*), *1301–1302* (*1960*).

This is the introductory statement for a symposium on radiation measurements. It was designed to outline the background in one phase of the problem of radiation quantities units.

Improving rectifier circuits, G. F. Montgomery, *Electronics, p. 86–87* (*April 7, 1961*).

The conventional half-wave rectifier and voltage doubler circuits can be modified to use an inductor-input filter advantageously. The results of these modifications are reduced peak rectifier current and improved load-voltage regulation and smoothing. The first modification requires an additional rectifier; the second requires a two-winding input inductor.

The robustness of life testing procedures derived from the exponential distribution, M. Zelen and M. C. Dannemiller, *Technometrics* **3,** *No. 1, 29–49* (*February 1961*).

Almost all the statistical procedures in current use for evaluating the reliability of components or equipment rest on the assumption that the failure times follow the exponential distribution. However, in practical situations one rarely has enough data to determine whether failure times are actually exponential. This paper studies the behavior of several statistical life testing procedures based on the exponential failure law if the true failure law is the Weibull distribution. It is found that these statistical techniques, which are widely used, are very sensitive to departures from initial assumptions. Applying these techniques to life test data when the exponential failure law is not satisfied may result in substantially increasing the probability of accepting components or equipments having poor mean-time-to-failure.

How to evaluate accuracy, W. J. Youden, *Materials Research and Standards* (*Am. Soc. Testing Materials, Philadelphia, Pa.*) **1,** *No. 4, 268–271* (*April 1961*).

This paper is one of a series of four integrated papers on errors of measurement under preparation by four authors for the

June 1960 ASTM meeting. It presents a logical breakdown of the error in a measurement into (*a*) the systematic error inherent in the procedure, (*b*) the local systematic error of the laboratory using the procedure and (*c*) the random error (precision). This breakdown should facilitate efforts to attain better accuracy. Several methods are given for identifying sources of error in measurements.

Improved standard for the calibration of vibration pickups, R. R. Bouche, *Exp. Mech., 1–6 (April 1961).*

As part of a continuing program on the development of primary vibration standards, an electrodynamic standard was modified so that it is free of transverse motion throughout almost all of its frequency range. In the vibration-pickup calibration service recently established at the National Bureau of Standards, the standard is used at frequencies from 10 cps to 2,000 cps at accelerations up to 10 g.

Velocity and acceleration pickups in common use calibrated on the standard provide reasonably accurate secondary vibration standards for use by government and industrial research laboratories. However an assembly of a small coil used with a magnet has been found to be a more accurate secondary vibration standard.

The development of more stable gage blocks, M. R. Meyerson, T. R. Young, and W. R. Ney, *ASTM Bull.* **1,** *No. 5, 368–374 (May 1961).*

American precision tool manufacturers have requested a higher degree of accuracy in gage blocks and their calibration than is currently available in order to keep pace with the needs of the missile, aircraft, and other precision industries. To meet this need, a long-range research program aimed at an accuracy of one part in 10 million in gage-block length calibrations is under way at the National Bureau of Standards. Significant advances have been made recently with the development of highly stable blocks and ultraprecise measurement techniques. This paper describes the highlights and presents the data obtained in the initial phases of the program.

The power spectrum and its importance in precise frequency measurements, J. A. Barnes and R. C. Mockler, *IRE Trans. Instrumentation* **I-9,** *No. 2, 149–155 (September 1960).*

The power spectral density functions of a frequency multiplier chain, driven by several different crystal oscillators, were obtained by comparing the output with a second chain which was stabilized with an ammonia maser. The frequency of the maser stabilized chain was demonstrated to be relatively fixed; the power spectrum of the other chain was determined by two different methods. The results are compared. Possible errors and uncertainties introduced by the methods are discussed. An analysis is made that relates the instantaneous frequency fluctuations of a signal with the power spectral density function.

Analysis predicts that when frequency modulation occurs in the first stages of frequency multiplication or in the primary frequency oscillator, the output power spectrum is, in general, not symmetrical. Furthermore, the sidebands are increased in intensity by the multiplication process. This is, in fact, observed to be the case. It is shown that a frequency counter will measure the frequency of the center of gravity of the power spectrum.

If signals having a complex power spectrum are used in precise frequency measurements, errors may result.

The nation's electronic standards program: where do we now stand? H. W. Lance, *IRE Trans. Instrumentation* **I-9,** *No. 2, 94–100 (September 1960).*

Recently increased standards activities throughout the nation have resulted in a large increase in the calibration services requested from NBS and in a number of related problems. Several of these are discussed, including desirable criteria for the staffing and instrumentation of electronic standards laboratories, the choice of interlaboratory standards to be submitted to NBS, and the use of these standards before and after calibration. An attempt is made to clarify the concept of "traceability of calibrations to NBS," and conditions under which a calibration may be called traceable are discussed. Suggestions are made regarding the use of available calibration services and the action to be taken when needed calibration services are not available. The need for an association of standards laboratories is pointed out, and many areas are noted in which such an association could make valuable contributions.

Trends in the technology of automatic data processing. S. N. Alexander, *AMA Report* **43,** *38–42 (1960).*

This is a summary of a talk presented to the Annual Office Management Conference of the American Management Association, Inc., in which the four elementary functions of automatic data processing systems are discussed as they relate to management. The progressive development of input and output devices and data storage and memory systems as well as improved logical organization of the central processor are described. In conclusion, the point is made that an evolution of appropriate automatic program procedures now in process is of comparable importance.

Reproducibilities of carbon and germanium thermometers at 4.2 °K, M. H. Edlow and H. H. Plumb, *Proc. Cyrogenic Eng. Conf., Boulder, Colo., Aug. 1960,* **6,** *542–547 (1961).*

Some new results are presented on the characteristics of secondary thermometers at temperatures in the liquid helium region. These results are for the reproducibility of the resistances of carbon and germanium resistors at 4.2 °K when they were cycled from 300 °K to 4.2 °K. The resistances of these thermometers were determined as functions of the vapor pressures of liquid helium in a liquid helium bath at nearly constant temperature. The resistance of Allen-Bradley resistors (10^2, ¼ watt), which have been continuously in liquid helium for many weeks at constant temperature have been found to drift. Similar drifts have not been detected for germanium resistors.

Other NBS Publications

Journal of Research 65A (Phys. and Chem.) No. 4 (July–August 1961). 75 cents.

Electrical properties and kinetics of electrode reactions, R. J. Brodd.

Effect of hydrostatic pressure upon the relaxation of birefrigence in amorphous solids, R. M. Waxler and L. H. Adams.

Vapor pressures of platinum, iridium, and rhodium, R. F. Hampson, Jr., and R. F. Walker.

Crystallization of bulk polymers with chain folding: theory of growth of lamellar spherulites, J. D. Hoffman and J. I. Lauitzen, Jr.

Phase equilibrium relations in the binary system barium oxide-niobium pentoxide, R. S. Roth and J. L. Waring.

Solid state reactions involving oxides of trivalent cations, S. J. Schneider, R. S. Roth, and J. L. Waring.

Gamma irradiation of fluorocarbon polymers, R. E. Florin and L. A. Wall.

Inhibition of diffusion flames of methyl bromide and trifluoromethyl bromide applied to the fuel and oxygen sides of the reaction zone, E. C. Creitz.

Journal of Research 65A (Phys. and Chem.) No. 5 (September–October 1961). 75 cents.

Calibration of a monitor for use in bremsstrahlung beams, E. G. Fuller and E. Hayward.

Mass spectrometric study of NF_2, NF_3, N_2F_2, and N_2F_4, J. T. Herron and V. H. Dibeler.

Rate of the reaction NO+N, and some heterogeneous reactions observed in the ion source of a mass spectrometer, J. T. Herron.

Synthesis of the humites nMg2SiO$_4$·Mg(F, OH)$_2$, A. Van Valkenburg.

Phase equilibria in systems involving the rare earth oxides. Part III. The Eu_2O_3–In_2O_3 system, S. J. Schneider.

Heats of hydrolysis and formation of dimethoxychloroborane, M. V. Kilday, W. H. Johnson, and E. J. Prosen.

Tritium-labeled compounds VII. Isotope effects in the oxidation of D-mannitols-C^{14} and D-mannitols-t to D-fructoses, L. T. Sniegoski, H. L. Frush, and H. S. Isbell.

Franck-Condon factors to high vibrational quantum numbers I: N_2 and N_2^+, R. W. Nicholls.

Journal of Research 65B (Math. and Math. Phys.) No. 3 (July–September 1961). 70 cents.

Theory of an accurate intermediary orbit for satellite astronomy, J. P. Vinti.

Note on the "baffled piston" problem, F. Oberhettinger.
Some results on non-negative matrices, M. Marcus, H. Minc, and B. N. Moyls.
Probability inequalities of the Tchebycheff type, I. R. Savage.

Journal of Research 65D (Radio Prop.) No. 5 (September–October 1961). 75 cents.

Frequency dependence of *D*-region scattering at VHF, J. C. Blair, R. N. Davis, Jr., and R. C. Kirby.
Theoretical scattering coefficient for near vertical incidence from contour maps, H. S. Hayre and R. K. Moore.
Mutual interference between surface and satellite communication systems, W. J. Hartman and M. T. Decker.
VHF and UHF signal characteristics observed on a long knife-edge diffraction path, A. P. Barsis and R. S. Kirby.
Experimental study of inverted L-, T-, and related transmission-line antennas, S. Prasad and R. W. P. King.
Reflection from a sharply bounded ionosphere for VLF propagation perpendicular to the magnetic meridian, D. D. Crombie.
Resonance of the space between earth and ionosphere, H. Poeverlein.
Observed attenuation rate of ELF (region below 1 kc/s) radio waves, A. G. Jean, A. C. Murphy, J. R. Wait, and D. F. Wasmundt.
A note concerning the excitation of ELF electromagnetic waves, J. R. Wait.
Computation of whistler ray paths, I. Yabroff.
On the analysis of LF ionospheric radio propagation phenomena, J. R. Johler.

Journal of Research 65D (Radio Prop.) No. 6 (November–December 1961). 75 cents.

The solar wind, E. N. Parker.
Attentuation coefficients for propagation at very low frequencies (VLF) during a sudden ionospheric disturbance (SID), E. T. Pierce.
Dipole radiation in a conducting half space, R. K. Moore and W. E. Blair.
Reliability of atmospheric radio noise predictions, J. R. Herman.
Effects of the ionosphere on VLF navigational aids, W. T. Blackband.
On the spectrum of terrestrial radio noise at extremely low frequencies, H. R. Raemer. (See above abstract)
The nonsingular embedding of transition processes within a more general framework of coupled variables, J. Heading.
Worldwide VLF standard frequency and time signal broadcasting, A. D. Watt, R. W. Plush, W. W. Brown, and A. H. Morgan.
Design of panoramic ionospheric resources, L. H. Heisler and L. D. Wilson.
A quick method for estimating the stage of the sunspot cycle, W. B. Chadwick.
Measurements of low-angle radiation from a monopole, A. C. Wilson.

Ideal gas thermodynamic functions and isotope exchange functions for the diatomic hydrides, deuterides, and tritides, L. Haar, A. S. Friedman, and C. W. Beckett, NBS Mono. 20 (1961) $2.75.
Causes of variation in chemical analysis and physical tests of portland cement, B. L. Bean and J. R. Dise, NBS Mono. 28 (1961) 25 cents.
Thermal expansion of technical solids at low temperatures. A compilation from the literature, R. J. Corruccini and J. J. Gniewek, NBS Mono. 29 (1961) 20 cents.
Mean electron density variations of the quiet ionosphere—May 3, 1959, J. W. Wright, L. R. Wescott, and D. J. Brown, NBS TN40–3 (PB151399–3) (1961) $1.50.
Bibliography on ionospheric propagation of radio waves (1923–1960), W. Nupen, NBS TN84 (PB161585) (1961) $7.00.
The absorption spectra of magnesium and manganese atoms in solid rare gas matrices, O. Schnepp. J. Phys. Chem. Solids **17,** Nos. 3/4, 188–195 (1961).
The Franck-Condon factor ($q_{v'v''}$) array to high vibrational quantum numbers for the $O_2(B^3\Sigma_u^- - X^3\Sigma_g^+)$ Schumann-Runge band system, R. W. Nicholls, Can. J. Phys. **38,** 1705–1711 (1960).
Ionospheric mapping by numerical methods, W. B. Jones and R. M. Gallet, Telecommun. J. **12,** 260–264 (December 1960).
The activation energy for hydrogen atom addition to propylene, M. D. Scheer and R. Klein, J. Phys. Chem. **65,** No. 375, 375–377 (1961).
Intramolecular rearrangements. I. *sec*-butyl acetate and *sec*-butyl formate, R. Borkowski and P. Ausloos, J. Am. Chem. Soc. **83,** No. 5, 1053–1056 (March 1961).
Titanium (III) chloride and titanium (III) bromide (titanium trichloride and titanium tribromide), J. M. Sherfey, Chapter IVB, Sec. 17, p. 57–61, Book, Inorganic Syntheses, by E. G. Rochow (McGraw-Hill Book Co., New York, N.Y., 1960).
Science news writing, D. M. Gates and J. M. Parker, Science **133,** No. 3447, 211–214 (January 1961).
Integrated starlight over the sky, F. E. Roach and L. R. Megill, Astrophys, J. **133,** No. 1, 228–242 (January 1961).
Elastomers for static seals at cryogenic temperatures, D. H. Weitzel, R. F. Robbins, G. R. Bopp, and W. R. Bjorklund, Rev. Sci. Insts. **31,** No. 12, 1350–1351 (December 1960).
The electromagnetic fields of a dipole in the presence of a thin plasma sheet, J. R. Wait, Appl. Sci. Research **8,** Sec. B, 397–417 (1960).
New standards for the space age, A. T. McPherson, Astronautics **6,** No. 1, 24-25; 50–54 (January 1961).
Near infrared atmospheric transmission to solar radiation, D. M. Gates, J. Opt. Soc. Am. **50,** No. 12, 1299–1304 (December 1960).
Determination of crystallite size distributions from X-ray line broadening, A. Bienenstock, J. Appl. Phys. **32,** No. 2, 187–189 (February 1961).
Correlation of visual and subvisual auroras with changes in the outer Van Allen radiation zone, B. J. O'Brien, J. A. Van Allen, F. E. Roach, and C. W. Gartlein, IGY Bull. No. 45, 1–16 (March 1961).
Arc source for high temperature gas studies, J. B. Shumaker, Jr., Rev. Sci. Instr. **32,** No. 1, 65–67 (January 1961).
The dependence of the melting temperature of bulk homopolymers on the crystallization temperature, L. Mandelkern, J. Polymer Sci. **XLVII,** issue 149, 494–496 (July 1960).
Spiral patterns in geophysics, V. Agy, J. Atmospheric and Terrest. Phys. **19,** 136–140 (1960).
Iron (99.9+), G. A. Moore and T. R. Shives, Metals Handb. **1,** 1206–1212 (1961).
The interfacial properties of polyesters at glass and water surfaces, R. R. Stromberg, Soc. Plastic Engr. **15,** 882–886 (October 1959).
Ionospheric absorption at times of auroral and magnetic pulsations, W. H. Campbell and H. Leinback, J. Geophys. Research **66,** No. 1, 25–34 (January 1961).
Some properties of new or modified excitation sources, M. Margoshes, Am. Soc. Testing Materials, Spec. Tech. Publ. No. 259, 46–58 (1959).
Seasonal and day-to-day changes of the central position of the S_q overhead current system, S. Matsushita, J. Geophys. Research **65,** No. 11, 3835–3839 (November 1960).
Hydrogen sulfide precipitation of the elements from 0.2–0,5 normal hydrochloric acid, J. I. Hoffman, Chemist-Analyst **50,** No. 1, 30 and 32 (March 1961).
The mechanism of electrolytic deposition of titanium from fused salt media, W. E. Reid, J. Electrochem. Soc. **108,** No. 4, 393–394 (April 1961).
Studies of elevated temperature corrosion of type 310 stainless steel by vanadium compounds, H. L. Logan, Corrosion **17,** 109–111 (April 1961).
Deep penetration of radiation, U. Fano and M. J. Berger, Proc. Symp. Appl. Math. **XI,** 43–59 (1961).
A simple low-temperature specimen holder for an X-ray diffractometer, D. K. Smith, Norelco Reporter **VII,** No. 1, 11–12 (January–February 1961).
Microbalance techniques for high temperature application, R. F. Walker, Book, Vacuum Microbalance Techniques, edited by M. J. Katz. I, 87–110 (Plenum Press Inc., New York, N.Y., 1961).
Investigation of bond in beam and pull-out specimens with high-yield-strength deformed bars, R. G. Mathey and D.

Watstein, J. Am. Concrete Inst. **32,** No. 9, 1071–1090 (March 1961).

Vacuum ultraviolet photolysis of ethane: Molecular detachment of hydrogen, H. Okabe and J. R. McNesby, J. Chem. Phys. **34,** No. 2, 668–669 (February 1961).

Shielding calculations for civil defense, C. Eisenhauer, Health Phys. **4,** No. 2, 129–132 (1960).

Hydrogen atom reactions with propene at 77 °K. Disproportionation and recombination, R. Klein and M. D. Scheer, J. Phys. Chem. **65,** 324–325 (1961).

The effect of solvents on the γ-ray radiolysis of methyl acetate and acetone, P. Ausloos, J. Am. Chem. Soc. **83,** No. 5, 1056–1060 (March 1961).

On the nature of the crystal field approximation, C. M. Herzfeld and H. Goldberg, J. Chem. Phys. **34,** No. 2, 643–651 (February 1961).

A study of auroral coruscations, W. H. Campbell and M. H. Rees, J. Geophys. Research **66,** No. 1, 41–55 (January 1961).

The nature, cause and effect of the porosity in electrodeposits. VII. A microscopic examination of nickel-chromium coatings after atmospheric corrosion, D. W. Ernst and F. Ogburn, Plating **48,** No. 4, 491–497 (May 1961).

Fracture characteristics of notched tensile specimens of titanium and a titanium alloy, G. W. Geil and N. L. Carwile, Materials Research and Standards (Am. Soc. Testing Materials, Philadelphia, Pa.) **1,** No. 1, 16–21 (Jan. 1961).

Absence of an isotope effect in the fractional recrystallization of alpha-D-glucose-1-*d*, H. S. Isbell, H. L. Frush, and N. B. Holt, Anal. Chem. **33,** 225–226 (Feb. 1961).

Applications of graphs and Boolean matrices to computer programming, R. B. Marimont, SIAM Rev. **2,** No. 4, 259–268 (Oct. 1960).

Comparison of national standards for roentgen measurement, H. O. Wyckoff, IXth Intern. Congress of Radiology, July 23–30, 1959 (München, Germany), 1315–1318 (1960).

Environmental factors in a family-size underground shelter, R. P. Achenbach, Proc. Meeting on Environmental Engineering in Protective Shelters, Feb. 8–10, 1960, Natl. Acad. Sci.-Natl. Research Council, Wash., D.C., 69–118 (1961).

Absorption and scattering of photons by holmium and erbium, E. G. Fuller and E. Hayward, Proc. Intern. Conf. Nuclear Structure, 760–763 (Kingston, Canada, 1960).

Introductory remarks, U. Fano, Conf. Coherence Properties of Electromagnetic Radiation, AFOSR–583, Report on Conf., 31–38 (University of Rochester, The Institute of Optics, Rochester, N.Y., April 1961).

Available heat sinks for protected underground installations, B. A. Peavy, Proc. Meeting on Environmental Engineering in Protective Shelters, Feb. 8–10, 1960, Natl. Acad. Sci.-Natl. Research Council, Wash., D.C., 69–118 (1961).

Interpretation of the appearance potentials of secondary ions, M. B. Wallenstein and M. Krauss, J. Chem. Phys. **34,** No. 3, 929–936 (Mar. 1961).

Observations on the chemiluminescent reaction of nitric oxide with atomic oxygen, H. P. Broida, H. I. Schiff, and T. M. Sugden, Trans. Faraday Soc **57,** No. 458, 259–265 (Feb. 1961).

Studies of the low-temperature distillation of hydrogen isotopes, T. M. Flynn, Cryogenics **1,** No. 2, 1–5 (Dec. 1960); Advances Cryogenic Engr. **6,** 236–244 (1961).

Inert enclosed pump for shaped flow of ultraclean solutions, M. W. Barnes and R. H. Noyce, Rev. Sci. Instr. **32,** No. 3, 353 (Mar. 1961).

On some partial differential equations of Brownian motion of a free particle, A. Ghaffari, (Abstract) Proc. Intern. Conf. on Partial Differential Equations and Continuum Mechanics (Univ. of Wisconsin, Madison, Wis., June 7–15, 1960), 348–350 (1961).

Radiation protection standards, L. S. Taylor, Radiology **74,** 824–831 (May 1960).

Atomic beam frequency standards, R. C. Mockler, R. E. Beehler, and C. S. Snider, IRE Trans. Instrumentation **I–9,** No. 2, 120–132 (Sept. 1960).

VLF phase perturbation associated with meteor shower ionization, C. J. Chilton, J. Geophys. Research **66,** No. 2, 379–383 (Feb. 1961).

Departures from the Saha equation for ionized helium. I. Condition of detailed balance in the resonance lines, R. N. Thomas and J. B. Zirker, Astrophys. J. **133,** No. 2, 588–595 (Mar. 1961).

Tests for regression coefficients when errors are correlated, M. M. Siddiqui, Annals Math. Stat. **31,** No. 4, 929–938 (Dec. 1960).

Electron diffraction studies on solid α-nitrogen, E. M. Horl and L. Marton, Acta Cryst. **14,** Pt. I, 11–19 (Jan. 10, 1961).

A comment on the NRL solar Lyman-Alpha results, J. T. Jefferies and R. N. Thomas, Astrophys. J. **133,** No. 2, 606–607 (Mar. 1961).

Hard gallium alloys for use as low contact resistance electrodes and for bonding thermocouples into samples, G. C. Harman, Rev. Sci. Instr. **31,** No. 7, 717–720 (July 1960).

Scattering of photons by deformed nuclei, E. G. Fuller and E. Hayward, Proc. Intern. Conf. Nuclear Structure, 763–766 (Kingston, Canada, 1960).

The glass electrode, R. G. Bates, Book, Reference Electrodes, edited by D. J. G. Ives and G. J. Janz (Academic Press Inc., New York, N. Y.), Chapter 5, 231–269 (1961).

A recalibration of the NBS standard thermal neutron flux, E. R. Mosburg, Jr., and W. M. Murphey, J. Nuclear Eng. (Reactor Science and Technology Pt.) **14,** 25–30 (1961).

The relationship of low-height ionosonde echoes to Auroral-zone absorption and VHF *D*-scatter, J. K. Olesen and J. W. Wright, J. Geophys. Research, **66,** No. 4, 1127–1134 (Apr. 1961).

Use of the bulge test for determining mechanical properties of stainless steel foil, D. B. Ballard, Materials Research and Standards **1,** No. 6, 471–473 (June 1961).

Some comments on the use and preparation of hard gallium alloys, G. G. Harman, Rev. Sci. Instr. **32,** No. 4, 465–466 (April 1961).

On the nature of equatorial spread *F*, R. Cohen and K. L. Bowles, J. Geophys. Research **66,** No. 4, 1081–1106 (April 1961).

A study of the chemical reactions in kilning bone char, F. G. Carpenter and V. R. Deitz, Proc, 6th Tech. Session on Bone Char 1959, p. 321 (Bone Char Research Project Inc., Charlestown, Massachusetts, 1961).

Rate of vaporization of refractory substances, R. F. Walker, J. Efimenkof, and N. L. Lofgren, Book Physical Chemistry in Aerodynamics and Space Flight (Pergamon Press, Inc., London, England), p. 24–30 (1961).

Analysis of pyrolyzates of polystyrene and ploy(methyl methacrylate) by gas chromatography, F. A. Lehmann and G. M. Brauer, Anal. Chem. **33,** No. 6, 673–676 (May 1961).

A note on phase velocity of VLF radio waves, J. R. Wait and K. P. Spies, J. Geophys. Research **66,** No. 3, 992–993 (Mar. 1961).

Microwave spectrum of isobutylene. Dipole moment, internal barrier, equilibrium conformation, and structure, V. W. Laurie, J. Chem. Phys. **34,** No. 5, 1516–1519 (May 1961).

Nonequilibrium processes in isotopically disordered crystals. Dependence on degree of order, R. Zwanzig, J. Math. Phys., **2,** No. 3, 370–372 (May–June 1961).

Intermolecular forces from optical spectra of impurities in molecular crystals, R. W. Zwanzig, Molecular Phys. **3,** No. 4, 305–311 (July 1960).

On the excitation of electromagnetic surface waves on a curved surface, J. R. Wait, IRE Trans. Ant. Prop. **AP–8,** No. 4, 445–448 (July 1960).

Solubility product phenomena in hydroxyapatite-water systems, H. M. Rootare, V. R. Deitz, and F. G. Carpenter, Proc. 6th Tech. Session on Bone Char 1959, p. 287 (Bone Char Research Project Inc., Charlestown, Massachusetts, 1961).

The automatic chloride titrator in the analysis of some ionic constituents, M. D. Peiperl, F. G. Carpenter, and V. R. Deitz, Proc. 6th Tech. Session on Bone Char 1959, p. 53 (Bone Char Research Project Inc., Charlestown, Massachusetts, 1961).

Spin-lattice relaxation in cerous magnesium nitrate, R. P. Hudson and R. S. Kaeser, Il Nuovo Cimento **19,** Serie X, 1275–1277 (March 16, 1961).

The photolysis of ethyl vinyl ether, E. Murad, J. Am. Chem. Soc. **83,** 1327–1330 (1961).

UNIVERSITY MICROFILMS INC
EDITORIAL DEPARTMENT
313 NORTH FIRST ST
ANN ARBOR MICH
SJR-C JUNE

UNITED STATES
GOVERNMENT PRINTING OFFICE
DIVISION OF PUBLIC DOCUMENTS
WASHINGTON 25, D.C.

OFFICIAL BUSINESS

PENALTY FOR PRIVATE USE TO AVOID PAYMENT OF POSTAGE, $300 (GPO)

JOURNAL OF RESEARCH of the National Bureau of Standards Vol. 65C, No. 4 October–December 1961
C. Engineering and Instrumentation

Contents

Page

A new airglow photometer. C. M. Purdy, L. R. Megill, and F. E. Roach. 213

A guide to the use of the modified reflectometer technique of VSWR measurement. Wilbur J. Anson. 217

An X-ray diffractometer cryostat providing temperature control in the range 4 to 300 °K. Floyd A. Mauer and Leonard H. Bolz. 225

Apparatus for determination of pressure-density-temperature relations and specific heats of hydrogen to 350 atmospheres at temperatures above 14 °K. Robert D. Goodwin. 231

The use of a thermistor for detecting eluent fronts in liquid-solid chromatography. Gaylon S. Ross. 245

Radiation field from a circular disk source. J. H. Hubbell, R. L. Bach, and R. J. Herbold. 249

The Bauschinger effect and residual microstresses in alpha brass. Clarence J. Newton. 265

A study by polarization techniques of the corrosion rates of aluminum and steel underground for sixteen months. W. J. Schwerdtfeger. 271

Publications of the National Bureau of Standards. 277
Index to volume 65C, January to December 1961. 281

For sale by the Superintendent of Documents, U.S. Government Printing Office, Washington 25, D.C. Price 75 cents (single copy)
Subscription price: $2.25 a year; 50 cents additional for foreign mailing.

UNITED STATES GOVERNMENT PRINTING OFFICE, WASHINGTON : 1961